



UNIVERSITAT<sup>DE</sup>  
BARCELONA

# Fabricating ultrasensitive metal nano-structures with Langmuir-Blodgett technique to improve plasmonic response of SERS

Mohammad Tahghighi Haji Alizadeh



Aquesta tesi doctoral està subjecta a la llicència **Reconeixement 4.0. Espanya de Creative Commons.**

Esta tesis doctoral está sujeta a la licencia **Reconocimiento 4.0. España de Creative Commons.**

This doctoral thesis is licensed under the **Creative Commons Attribution 4.0. Spain License.**

Programa de doctorat en Nanociències



UNIVERSITAT DE  
BARCELONA

Fabricating ultrasensitive metal nano-structures  
with Langmuir-Blodgett technique to improve  
plasmonic response of SERS

Mohammad Tahghighi Haji Alizadeh<sup>1, 2</sup>

Director/a: Jordi Ignés<sup>1, 2</sup>

Tutor/a: Jordi Ignés

*1 Departament de Ciència dels Materials i Química Física, Universitat de Barcelona*

*2 Institut de Nanociència i Nanotecnologia de la Universitat de Barcelona (IN2UB)*



*Dedicated to a kind wife who endured years of distance between us and with her patience and endurance during this period paved my way to achieve scientific aspirations. Also dedicated to my mother and her positive energies and support which are always helpful and facilitate my problems and, at the end I want dedicate my research to my father who is not among us now and I hope he will be blessed by God.*

## **Acknowledgments**

*Firstly I want to exalt my director of PhD thesis, Prof. Jordi Ignés from the physical chemistry section at University of Barcelona. His insight and knowledge into the subject steered me through this research from the first day. He was supervising and safeguarding my ideas and research and all the time he was ready to give advice on experimental ideas and without whom I would not have been able to complete this research. I appreciate his effort and communication with other departments and groups to solve my practical and theoretical problems. Jordi all the time tried his best to facilitate my research and eliminate obstacles. I appreciate his availability by any means of communication before and after COVID-19 epidemic, for fast troubleshooting. He helped me a lot in revising and composing my papers. I have to admit that Jordi was by my side not only as a director of PhD but also as a compassionate friend all the time.*

*I have to exalt Francesc Sagués as head of SOC&SAM group and member of monitoring committee of my doctorate degree. Davide Janner, a former post doc in ICFO and currently a professor of DISAT politecnico di Torino helped me a lot and I used his advice during my PhD research.*

*Laboratory No 4017 in physical chemistry section at UB where I did most of my research. It was a lovely and nostalgic place and I owe most of my progress to this calm and friendly atmosphere. I appreciate all the colleagues in SOC&SAM group and I thank them for their help and cooperation. Working with them has been a daily source of joy and*

*motivation, and it opened a whole set of new perspectives in my projects. Finally, my biggest thanks to my family for all the support they have shown me through this research, the culmination of five years of distance learning was very hard for both sides and I appreciate their patience.*

## Abstract

Nanoparticle self-assembly is a versatile and coherent strategy for the development of functional nanostructured materials, offering low-cost and scalable methods that can be fine-tuned for many different specific application. Functionalized nanoparticles could be spread at the interface of liquid/gas by means of self-assembly. In this work, we demonstrate a pathway for the fabrication of tailorable quasi two-dimensional lattices of gold nanoparticles with several core sizes and shapes (5, 10, 20, 30, 40 nm and nano-urchin) to be used in surface enhanced Raman scattering (SERS) detection of biomolecules.

Upon spreading gold nanoparticles at the water/air interface in this research, we used the Langmuir-Blodgett technique as a way of making supra-molecular and nano-structure assembly in ultrathin films with a controlled layered and spatial structure, which have many envisioned technological applications for several branches of science as well as to develop SERS substrates. Monolayers of gold particles were transferred at a target lateral density using the Langmuir–Blodgett technique. Once gold nanoparticles were firmly adhered to the substrate, we used electroless plating to let the nanoparticle grow, thus tuning the plasmonic response and leading to SERS enhancement. Compared to direct deposition, chemical deposition or lithographic methods, our protocol enables to obtain consistent results and much higher coverages of Au nanoparticles thanks to the active control of the surface pressure of the spread monolayers.

Prepared substrates were analyzed with different techniques such as UV/VIS spectroscopy, SEM and TEM microscopy. We have demonstrated that, for a given particle size, the enhancement for SERS detection of a referent analyte, 4-MBA, can be tuned by controlling the packing density of the nanoparticles at the water/air interface by adjusting the surface pressure using the Langmuir film balance setup. The other factor which affects the SERS signals is the thickness of a subsequent gold layer, deposited and tuned by using electroless plating.

After finding the optimum conditions of surface pressure and electroplating time for 10 nm gold nanoparticles, we entered the second phase of the experiments to unveil the effect of gold nanoparticle size on our study. SERS data of different-sized nanoparticles did not prove that bigger particles result in better SERS signals. However, urchin-shaped gold nanoparticles have shown more intense

signals in comparison with spherical nanoparticles. For the same conditions of preparation, we achieved better result by using urchin-shaped nanoparticles.

In order to test our substrate efficiency to detect more substances, in the final step of this research, we investigated and performed tests on Thiram and Carbaryl as water-polluting molecules that are widely using as pesticide compounds. We performed several SERS measurements with different substrates and studied the effect of gold nanoparticles shape, contact time between substrate and pollutant solution, substrate functionalization with thiol groups, and effect of pollutant solution concentration on SERS signals. Finally, we report the limit of pollutant detection with our prepared substrates.

## **Resum**

El procés d'autoassemblatge de nanopartícules és una estratègia versàtil i coherent per al desenvolupament de materials nanoestructurats funcionals, que ofereix mètodes de baix cost i escalables que es poden ajustar per a diferents aplicacions específiques. Les nanopartícules funcionalitzades es podrien estendre a la interfície de líquid / gas mitjançant un fenomen d'autoassemblatge. En aquest treball, demostrem una via per a la fabricació de xarxes quasi bidimensionals adaptables de nanopartícules d'or amb diverses mides i formes de nucli (5, 10, 20, 30, 40 nm i nano-eriçó) que s'utilitzaran per a la detecció de biomolècules en dispersió Raman de superfície millorada (SERS).

En estendre nanopartícules d'or a la interfície aigua / aire en aquesta investigació, hem utilitzat la tècnica Langmuir-Blodgett com una manera de fer un assemblatge de nanoestructures en pel·lícules ultrafines amb una estructura espacial i de capes controlades, que tenen moltes aplicacions tecnològiques potencials en diverses branques de la ciència, com ara substrats SERS. Les monocapes de partícules d'or es transfereixen, a una densitat lateral determinada, sobre substrats de vidre o sílice mitjançant la tècnica LB. Una vegada que les nanopartícules d'or s'han adherit fermament al substrat, vam utilitzar un mètode d'electrodeposició d'or sense electròlisi per fer créixer les nanopartícules, ajustant així la resposta plasmònica i la millora del SERS. En comparació amb la deposició directa, la deposició química o els mètodes litogràfics, el nostre protocol permet obtenir resultats consistents i una cobertura molt més gran de nanopartícules d'or gràcies al control actiu de la pressió superficial de la monocapa estesa sobre la interfície aigua/aire.

Els substrats preparats es van analitzar amb diferents tècniques com l'espectroscòpia *UV / VIS*, microscòpia *SEM* i *TEM*. Hem demostrat que, per a una mida de partícula determinada, la millora per a la detecció SERS d'un analit referent, 4-MBA, es pot ajustar controlant la densitat d'empaquetament de les nanopartícules a la interfície aigua / aire ajustant la pressió superficial mitjançant la balança de pel·lícules de Langmuir. L'altre factor que afecta els senyals SERS és el gruix de la capa d'or dipositada posteriorment mitjançant una tècnica no-electrolítica.

Després de trobar els paràmetres òptims de pressió superficial i temps d'electrodeposició per a nanopartícules d'or de 10 nm, vam entrar a la segona fase de l'estudi per descobrir l'efecte de la mida de les nanopartícules d'or en el nostre

sistema. Tot i que les dades SERS de nanopartícules de diferent mida no van indicar que les partícules més grans donessin millors senyals SERS, les nanopartícules d'or en forma d'eriçó han mostrat senyals més intensos en comparació amb les nanopartícules esfèriques. En les mateixes condicions de preparació, vam obtenir un millor resultat mitjançant l'ús de nanopartícules de forma d'eriçó.

Per tal de provar l'eficiència del nostre substrat per detectar més substàncies, en el darrer pas d'aquesta investigació vam investigar i realitzar proves emprant Thiram i Carbaryl com a molècules contaminants de l'aigua que s'utilitzen àmpliament com a compostos pesticides. Hem realitzat diverses mesures de SERS amb substrats diferents i hem estudiat l'efecte de a) la forma de les nanopartícules d'or, b) el temps de contacte entre el substrat i la solució contaminant, c) la funcionalització del substrat amb grups tiol i d) l'efecte de la concentració de solució contaminant en els senyals SERS. Finalment, informem del límit de detecció d'aquests contaminants amb els nostres substrats nanoestructurats.

# Contents

<i>List of Figures</i>	3
<i>List of Tables</i>	5
<i>List of abbreviations</i>	5
<b>1. Introduction</b>	19
1.1 Nanotechnology	20
1.1.1 Preface	20
1.1.2 World of Nano and Nanotechnology	20
1.1.2.1 Definition and history of nanotechnology	20
1.1.2.2 Nanotechnology in the modern era	21
1.1.2.3 Nanoparticles	22
1.2 Gold in nanotechnology	23
1.2.1 Gold nanoparticles	24
1.2.2 Gold utilization in ancient civilization	25
1.2.3 Gold in the spotlight of researchers	26
1.3 Surface Plasmon Resonance (SPR)	27
1.3.1 Mathematical models of surface Plasmon	29

1.3.1.1	<i>Drude Model</i>	29
1.3.1.2	<i>Mie Model</i>	30
1.3.2	<i>LSPR VS SPR</i>	31
1.4	<i>Gold nanoparticles monolayers using the Langmuir Blodgett technique</i>	35
1.4.1	<i>Preface</i>	35
1.4.2	<i>Particle preparation</i>	35
1.4.3	<i>Langmuir monolayers</i>	36
1.4.4	<i>Langmuir-Blodgett Technique</i>	37
1.4.5	<i>Langmuir-Blodgett vs Langmuir-Schaffer technique</i>	38
1.4.6	<i>Langmuir film balance</i>	39
1.4.7	<i>Surface tension</i>	40
1.4.8	<i>Surface pressure</i>	41
1.4.9	<i>The surface pressure area isotherm</i>	41
1.4.10	<i>Brewster Angle Microscope</i>	43
1.5	<i>RAMAN spectroscopy</i>	46
1.5.1	<i>Preface</i>	46
1.5.2	<i>Raman Technique background and history</i>	46
1.5.3	<i>Scattering of light in RAMAN</i>	47
1.5.4	<i>Infrared spectroscopy (IR)</i>	48
1.5.5	<i>Difference between RAMAN and Infrared spectroscopy</i>	50
1.5.6	<i>Theoretical principals of EM and molecular polarization</i>	50
1.5.7	<i>Raman Device Components</i>	52
1.6	<i>Surface Enhanced Raman Spectroscopy (SERS) Technique</i>	54
1.6.1	<i>Preface</i>	54
1.6.2	<i>SERS Scattering phenomena</i>	55
1.6.3	<i>SERS substrates</i>	57
1.6.4	<i>SERS in different media</i>	58
1.6.5	<i>SERS frequencies</i>	59
1.6.6	<i>SERS substrate preparation</i>	61
1.6.6.1	<i>Chemical Vapor Deposition (CVD) method</i>	62
1.6.6.2	<i>Nano Imprint Lithography (NIL) method</i>	63
1.6.6.2.1	<i>Direct writing method of NIL</i>	64
1.6.6.2.2	<i>Optical Lithography</i>	65
1.6.6.3	<i>SERS substrate preparation by self-assembly method</i>	66
1.7	<i>Objectives of research</i>	68
<b>2.</b>	<b><i>Materials and methods</i></b>	69
2.1	<i>Preface</i>	70
2.2	<i>Materials</i>	70

2.3 Instruments	71
2.4 Software	73
2.5 Methods	73
2.5.1 Gold nano-star preparation	73
2.5.2 Nanoparticle functionalization and phase transfer	73
2.5.3 Gold NP Langmuir monolayer preparation	76
2.5.4 Substrate preparation	76
2.5.5 Monolayer transfer onto a solid substrate	77
2.5.6 Vis–NIR spectroscopy	78
2.5.7 Scanning electron microscopy	78
2.5.8 Electroless deposition of gold	78
2.5.9 Solid substrate functionalization with 1-DDT	79
2.5.10 Surface Enhanced Raman Scattering	80
2.5.10.1 4-MBA incubation	80
2.5.10.2 Thiram incubation	80
2.5.10.3 Carbaryl incubation	80
<b>3. SERS substrate preparation by LB technique and SERS measurement of 4-MBA</b>	<b>82</b>
3.1 Preface	83
3.2 Introduction	83
3.3 Methods	84
3.4 Results	85
3.4.1 Langmuir monolayers of nanoparticles	85
3.4.2 Langmuir–Blodgett films as templates for nanostructure formation	87
3.4.3 SERS performance of the gold monolayers	90
3.5 Conclusions	94
<b>4. Effect of gold nanoparticle size and shape on the SERS performance</b>	<b>95</b>
4.1 Preface	96
4.2 Introduction	96
4.3 Experimental	97
4.4 Results	98
4.4.1 Monolayers of Spherical Gold Nanoparticles	98
4.4.2 SERS Performance of Spherical Gold Nanoparticle Monolayers	99
4.4.3 SERS Performance of Urchin-Shaped Gold Nanoparticle Monolayers	102
4.4.4 Homogeneity of the SERS Substrates and Detection of Thiram	104
4.5 Conclusions	107
<b>5. SERS detection of water pollutant substances</b>	<b>109</b>

5.1 Preface	110
5.2 Introduction	110
5.2.1 Thiram	110
5.2.2 Carbaryl	111
5.2.3 Methods for the detection of Thiram and Carbaryl	112
5.3 Methods	113
5.4 Results	114
5.4.1 Thiram detection	114
5.4.1.1 Effect of surface pressure	114
5.4.1.2 Effect of contact time on Thiram adsorption on substrate	122
5.4.1.3 Effect of Thiram solution concentration on SERS measurements	123
5.4.1.4 Effect of 1-DDT functionalization on the performance of SERS substrates	125
5.4.2 Carbaryl detection	126
5.4.2.1 Effect of surface pressure	127
5.4.2.2 Effect of contact time on Carbaryl adsorption on substrates	133
5.4.2.3 Effect of Carbaryl solution concentration on SERS measurements	134
5.4.2.4 Effect of 1-DDT functionalization on the performance of SERS substrates	136
5.5 Conclusions	137
<b>6. Final conclusions and future ideas</b>	139
<b>List of references</b>	142
<b>List of publications</b>	

## **List of the Figures:**

- 1.1 *Scale of nano in scientific world. (P: 21)*
- 1.2 *TEM images of gold nanoparticles (P: 25)*
- 1.3 *Lycurgus cup (P: 25)*
- 1.4 *Schematic view of Surface Plasmon (P: 28)*
- 1.5 *Effect of electric field on electron orientation and formation of dipole (P: 31)*
- 1.6 *Difference between evanescent plasmon field of SPR and LSPR (P: 32)*
- 1.7 *Langmuir Film of MPG (P: 37)*
- 1.8 *Schematic view of monolayer preparation at the air/water interface (P: 38)*
- 1.9 *Schematic of the Langmuir-Blodgett and Langmuir-Schaefer methods (P: 39)*
- 1.10 *Commercial Langmuir trough (P: 39)*
- 1.11 *Schematic diagram of the Wilhelmy plate mechanism (P: 40)*
- 1.12 *Surface pressure—area isotherms of a Langmuir film (P: 42)*
- 1.13 *Brewster Angle Microscope (BAM) (P: 43)*
- 1.14 *Schematic of a Brewster Angle Microscopy (P: 44)*
- 1.15 *Effect of surface pressure on forming 1-monopalmitoyl-rac-glycerol monolayers (P: 45)*
- 1.16 *Scattered radiation from particles (P: 47)*
- 1.17 *Raman spectrum of CCl<sub>4</sub> (P: 48)*
- 1.18 *Range of wavelength that used in IR spectroscopy (P: 49)*
- 1.19 *Formation of electromagnetic wave (P: 51)*
- 1.20 *Schematic view of Raman devices (P: 53)*
- 1.21 *Electromagnetic enhancement models (P: 57)*
- 1.22 *Wavelength ranges of Ag, Au, and Cu as SERS substrate (P: 58)*
- 1.23 *Schematic comparison between SERS techniques (P: 59)*
- 1.24 *Schematic view of CVD process (P: 62)*
- 1.25 *Schematic comparison of a typical Thermal NIL and UV-NIL processes (P: 64)*
- 1.26 *Schematic of UV exposure in lithography method (P: 66)*
  
- 2.1 *Devices which are used in entire research (P: 72)*
- 2.2 *Surface structure of functionalized gold nano particles (P: 75)*
- 2.3 *Surface of functionalized glass and silica with APTES (P: 77)*
- 2.4 *Schematic of the LB monolayer transfer (P: 78)*
- 2.5 *Schematic OF gold electroless plating (P: 79)*
  
- 3.1 *Surface pressure vs. particle surface number density isotherm (P: 86)*
- 3.2 *Vis–NIR absorption spectra for LB films of 10 nm gold nanoparticles (P: 87)*

- 3.3 *Vis–NIR spectra for LB films of 10 nm gold nanoparticles as a function of electroless plating time (P: 88)*
- 3.4 *SEM micrographs of nanoparticle LB films (P: 89)*
- 3.5 *SERS spectra of 4-MBA adsorbed on gold nanoparticle monolayers transferred at different lateral pressures (P: 91)*
- 3.6 *SERS spectra of 4-MBA adsorbed on gold nanoparticle monolayers followed by different electroplating times (P: 92)*
- 3.7 *SERS map of the 1077 cm<sup>-1</sup> peak in a sample of 4-MBA (P: 93)*
  
- 4.1 *Maximum wavelength of UV–vis absorption spectra of gold monolayers (P: 98)*
- 4.2 *SEM micrographs of spherical gold NP Langmuir–Blodgett (P: 99)*
- 4.3 *Surface Enhanced Raman Spectroscopy (SERS) spectra of 4-MBA adsorbed on 10 nm gold NP monolayers prepared at different lateral pressures (P: 101)*
- 4.4 *SERS spectra of 4-MBA adsorbed on gold nanostars prepared at different lateral pressures (P: 103)*
- 4.5 *SERS map of the 1588 cm<sup>-1</sup> peak in a sample of 4-MBA with substrate with consist of different size of gold NP (P: 106)*
- 4.6 *SERS signal and detection of 1 μM of Thiram in water (P: 107)*
  
- 5.1 *SERS spectra of 5 μM Thiram solution on fused silica substrate with a 10 nm gold nanoparticle (P: 116)*
- 5.2 *SERS spectra of Thiram adsorbed on 10 nm gold nanoparticle monolayers from 1 μM solution (P: 118)*
- 5.3 *SERS spectra of Thiram adsorbed on 10 nm gold nanoparticle monolayers from 5 μM solution (P: 119)*
- 5.4 *SERS spectra of Thiram adsorbed on nanostar gold nanoparticle monolayers from a 1 μM solution (P: 120)*
- 5.5 *SERS spectra of Thiram adsorbed on nanostar gold nanoparticle monolayers from 5 μM solution (P: 121)*
- 5.6 *SERS spectra of Thiram adsorbed on gold nanostar monolayers from 5 μM solution with different contact times (P: 123)*
- 5.7 *SERS spectra of Thiram adsorbed on 10 nm gold nanoparticle monolayers effect of solution concentration (P: 124)*
- 5.8 *SERS spectra of Thiram adsorbed on nanostar gold monolayers effect of 1-DDT functionalization (P: 126)*
- 5.9 *SERS spectra of 5 μM Carbaryl solution on fused silica substrates with 10 nm gold NP (P: 127)*
- 5.10 *SERS spectra of Carbaryl adsorbed on 10 nm gold nanoparticle monolayers from 1 μM solution (P: 129)*

- 5.11 *SERS spectra of Carbaryl adsorbed on 10 nm gold nanoparticle monolayers from a 5  $\mu$ M solution (P: 130)*
- 5.12 *SERS spectra of Carbaryl adsorbed on nanostar gold nanoparticle monolayers from a 1  $\mu$ M solution (P: 131)*
- 5.13 *SERS spectra of Carbaryl adsorbed on nanostar gold nanoparticle monolayers from a 5  $\mu$ M solution (P: 132)*
- 5.14 *SERS spectra of Thiram adsorbed on gold nanostar monolayers from 5  $\mu$ M solution with different contact times (P: 134)*
- 5.15 *SERS spectra of Thiram adsorbed on 10 nm gold nanoparticle monolayers effect of solution concentration (P: 135)*
- 5.16 *SERS spectra of Carbaryl adsorbed on nanostar gold monolayers effect of 1-DDT functionalization (P: 137)*

**List of the Tables:**

- 1.1 *Physicochemical properties of gold (p: 21)*
- 1.2 *Raman frequencies of common chemical functional groups (p: 61)*
  
- 2.1 *Brief description of used chemicals (p: 71)*
- 2.2 *Gold nanoparticle phase transfer conditions (p: 75)*
  
- 5.1 *Physicochemical properties of Thiram (p: 111)*
- 5.2 *Physicochemical properties of Carbaryl (p: 112)*
- 5.3 *Number of 10 nm gold particles per area on the solid substrate calculated from SEM images (p: 115)*
- 5.4 *Theoretical Band assignments of major peaks in Raman spectra of Thiram (p: 116)*

**List of the abbreviation:**

Below, find a list of abbreviations for important terms and concepts used in this thesis:

**APTES:** (3-Aminopropyl) Triethoxysilane ( $C_9H_{23}NO_3Si$ )

**AUNPs:** Gold nanoparticles

**BAM:** Brewster Angle Microscope

**BP:** Black Phosphorous

**CCD:** Charge-Coupled Device

**CT:** Charge Transfer Affect

**CTAB:** Cetrimonium Bromide ( $C_{19}H_{42}BrN$ )

**CVD:** Chemical Vapor Deposition

**EM:** Electromagnetic Field

**EME:** Electromagnetic Field Effect

**EW:** Evanescent Wave

**FTIR:** Fourier-Transform Infrared Spectroscopy

**IR:** Infrared Spectroscopy

**LB:** Langmuir-Blodgett

**LS:** Langmuir-Schaefer

**LSPR:** Localized Surface Plasmon

**MRLs:** Maximum Residue Limits

**NIL:** Nano Imprint Lithography

**NPs:** Nanoparticles

**PAHs:** Polycyclic Aromatic Hydrocarbons

**PEG:** Polyethylene Glycol ( $C_{2n}H_{4n+2}O_{n+1}$ )

**RI:** Refractive Index

**SAM:** Self Assembled Monolayer

**SEM:** Scanning Electron Microscope

**SERS:** Surface Enhanced Raman Spectroscopy

**SPR:** Surface Plasmon Resonance

**STM:** Scanning Tunneling Microscope

**TEM:** Transmission Electron Microscopy

**TERS:** Tip Enhanced Raman Spectroscopy

**TMDs:** Transition Metal Dichalcogenides

**1-DDT:** 1-Dodecanthiol

# ***1. INTRODUCTION***

## **1.1 Nanotechnology**

### **1.1.1 Preface**

Nano science is one of the new branches of science that has been studied by many scientists in the 20 and 21<sup>ST</sup> century. With the improvement of chemistry and physics in the early twentieth century, researchers already needed to identify and recognize the world of molecules and atoms. Therefore, many researchers have studied and tried to open a way to this world. These efforts led to the invention of the electron microscope in the mid-twentieth century. In recent days the electron microscope become an integral part in research laboratories and institutes. The invention of the electron microscope was a turning point in the history of nanoscience. Today high-tech models of electron microscopes are available for researchers in order to study and analyze a new world of small particles called nano world.

### **1.1.2 World of nano and nanotechnology**

#### **1.1.2.1 Definition and History of nanotechnology**

Nanotechnology and nanoscience are branches of science and engineering related to the nano scale world with dimensions of 100 nm or less. In recent days, nanotechnology has been adopted by research and industrial sectors due to its applications in different fields of science. Nano comes from a Greek word 'dwarf' that means very small size [1, 2]. In the names of units of measure, it has the specific sense "one billionth" ( $10^{-9}$ ) of a meter. *Fig 1.1.*

Nanoscience as a 21<sup>st</sup> century frontier is science, engineering, and technology handled at the nanoscale, typically in the range of 1 to 100 nanometers, where unique phenomena happen, and nanotechnology enable researchers to use the features of nanotechnology in novel applications [3]. Richard Zsigmondy for the first time adopted the concept of a "nanometer". He was an Austrian chemist who won the Nobel Prize in chemistry in 1925. Zsigmondy used nanometer as a term in his study on colloidal gold particles, and he measured and characterized gold particles with an electron microscope for the first time. 34 years later, in 1959, Richard P. Feynman, a physicist at CalTech, predicted the advent of nanomaterials. One of his famous ideas was born when he said, "There is plenty of room at the bottom," and suggested that minimizing the scale to nano level and starting from the

bottom will be the key to future technology and scientific progress [1, 4]. Feynman tried to describe a process in which scientists would be able to employ and manipulate individual atoms and molecules. He was one of the first researcher who published a scientific paper about nanotechnology in 1960 [5].

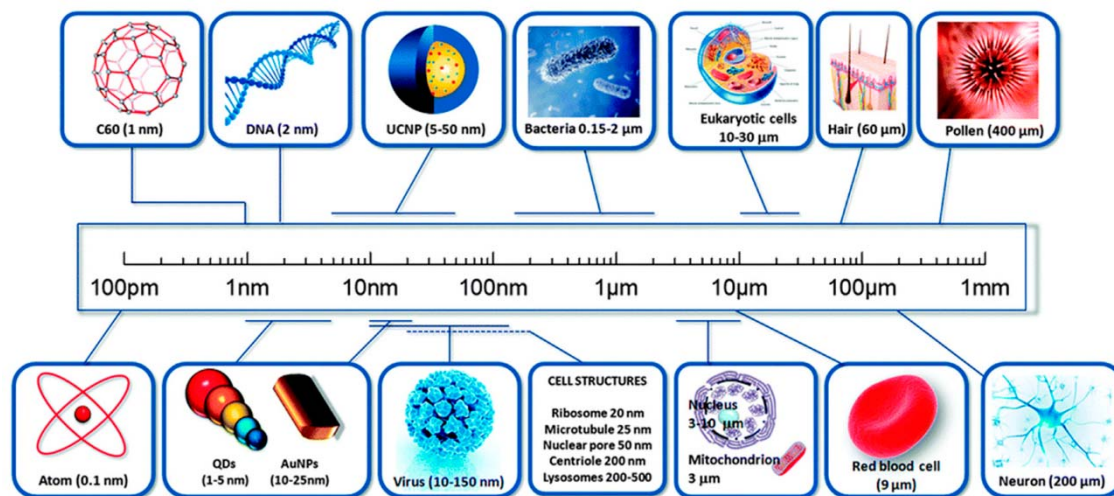


**Fig.1.1** scale of nano in scientific world adapted from[1]

Almost 15 years after Feynman's prediction, Norio Taniguchi, a Japanese scientist, was the first person to use "nanotechnology" to demonstrate semiconductor processes that occurred at the nanometer scale [6].

Another pioneer in nanotechnology and related techniques was Drexler. He was the first who proposed the idea of a nanoscale "assembler" that was able to reproduce a copy of itself and other items, in the other word he mentioned in the theory that molecules could robotically assemble structures and devices by manipulating individual atoms or molecules. The term "molecular nanotechnology" is related to molecular simulations at the nanoscale, and it comes from Drexler's vision and his theory [7].

### **1.1.2.2 Nanotechnology in the modern era**

One of the famous definitions of nanotechnology is the study of phenomena and specification of materials at atomic, molecular and macromolecular scales, where properties of nanoparticles (NPs) as constituents of some nano systems, differ significantly from those at a larger scale. Nanotechnology and all its related phenomena are nowadays very familiar to us and it is expected that the market value

of nanotech related products will increase rapidly by hundreds of billions of euro in the 21<sup>st</sup> century [1, 6].

There is a brief and general definition of nanotechnology stated by the US National Science and Technology Council “The essence of nanotechnology is the ability to work at the molecular level, atom by atom, to create large structures with fundamentally new molecular organization. The aim is to exploit these properties by gaining control of structures and devices at atomic, molecular, and supramolecular levels and to learn to efficiently manufacture and use these devices.” [8].

The improvement of nanotechnology in the 1980s coincided with experimental advances such as the invention of the scanning tunneling microscope (STM) in 1981. “Engines of Creation” is a book about modern nanotechnology published in 1986 which began with the clarification and generalization of a conceptual framework for nanotechnology purposes. Significant debates about the potential applications of molecular nanotechnology, as well as the possibility of its application by its proponents and the move by governments to establish and develop nanotechnology research, were issues that made nanotechnology popular in the early 2000s. The early 2010s saw the beginning of industrial applications of nanotechnology, although these applications were more limited to the mass applications in nanomaterials than the modifiable applications that nanotechnology envisioned[9].

Since the beginning of this century there is an increased interest in all fields of nanoscience and nanotechnology. Some part of the scientific phenomena in chemistry and physics are not explained without fully recognizing the nano structure of materials.

### **1.1.2.3 Nanoparticles**

The most significant parameter which make NPs unique is their high ratio of surface area to volume. As a result of this fact they are being used in the various fields of science such as diagnostic medicine, optoelectronics, display instruments, catalysis, fabricating biological and electrical sensors, monitoring diseases like cancer cells, drug delivery, and detection of environmental toxic metals or molecules[10].

NPs are used widely in different branches of science as mentioned. Among the different and various uses of NPs in recent days, studying nano-sensors has become increasingly popular. One of the final goals in this field is the fabrication and

manipulating of particles which would be the building blocks for sensors and electronic devices.

Metallic NPs are used as a main substrate in many sensors due to their plasmonic effect. This plasmonic effect is the main feature that separates these particles from non-metal particles, which causes interesting scattering, absorbance and coupling properties based on their geometries and relative positions. These unique properties have made them a focus of research in many applications including solar cells, spectroscopy, signal enhancement for imaging, and cancer treatment.

Metallic NPs have attracted the attention of many scientists for over a century and are widely utilized in several branches of science. They are in the spotlight because of their significant potential in nanotechnology. Today these NPs can be easily synthesized and modified with different functional groups, which enable them to be conjugated with antibodies, ligands, and drugs and thus their high plasmonic potential could be utilized in biotechnology, magnetic separation, targeted drug delivery, and vehicles for gene and chemical sensors [11].

NPs can be suspended in a liquid in a kinetically stable manner forming colloidal suspensions. This is the usual result of NPs synthesis and a useful way to prevent NPs aggregation. In other words a colloid is a mixture in which one substance of microscopically dispersed insoluble particles are suspended throughout another substance. A sol is an example of colloidal suspension and described as a homogeneous, non-crystalline media in which insoluble particles are dispersed in liquid substrate.

## ***1.2 Gold in nanotechnology***

Gold (Au) is a metal element located in group XI of the periodic table alongside with Cu, Ag and Rg. Au is derived from the Latin term aurum meaning “dawn glow”. Au has a shiny yellow appearance. Bulk gold is very stable and could be found in a pure form in nature. Normally, the tendency of this element to chemical reaction is very low and it does not rust in the presence of oxygen. In addition to the use as financial support and its use in jewelry, gold has various other applications, including: dentistry, the production of stained glass and the electronics industry, diagnosis and medical treatment and, due to its high electrical conductivity, it is used in electrical wiring [12].

Specification	Amount
Atomic number	79
Atomic weight	196.9655 g.mol <sup>-1</sup>
Melting point	1062 °C
Boiling point	2000 °C
Density	19.3 g.cm <sup>-3</sup> at 20°C
Isotopes	7
Oxidation States	+1, +3
Electron Configuration	[Xe]4f <sup>14</sup> 5d <sup>10</sup> 6s <sup>1</sup>

**Table. 1.1** physicochemical properties of gold

Gold does not have a specific crystal shape (so-called amorphous). In nature, it is found among volcanic rocks and sometimes among river and lake sediments. Gold is exploited directly from the mine and as a by-product of the mining and treatment of nickel, copper, zinc, lead, and silver ores [13].

Au in compounds appears in its (I) and (III) valences. Gold has a great tendency to form complexes in which it is always in the valence (III). Gold (I) compounds are not very stable and are generally oxidized to valence (III) or reduced to free metal. Of course, it is a general rule that inactive (noble) metal compounds can be easily reduced to the corresponding metal, whereas in the case of active metal compounds this is not easily done.

### **1.2.1 Gold nanoparticles**

After the invention of electron microscopy and the discovery of the world of nano materials, Gold NPs became noticed by many scientists because of their unique attributes. Gold NPs (AuNPs) have peculiar physical and chemical attributes that make them excellent tools and substrates for biological and medical applications. First, AuNPs can be synthesized in a straightforward manner and can be made highly stable. Second, they feature unique and remarkable optical and electrical properties. Third, they provide high surface-to-volume ratio with excellent biocompatibility to bind other molecules and ligands. Finally, AuNPs offer a suitable substrate for multi-functionalization with a wide range of organic and biological ligands to prepare proper sensors for the selective binding and detection of small molecules and biological targets.

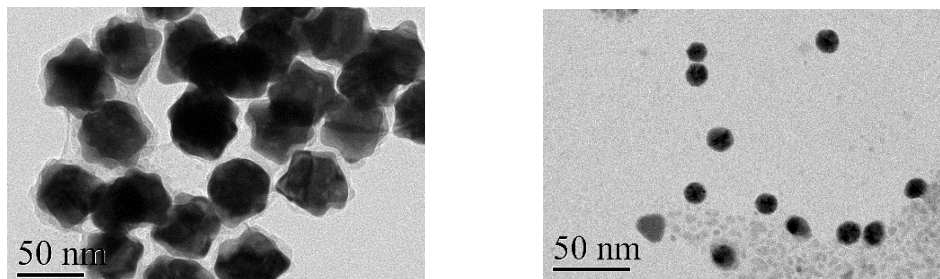


**Fig.1.2** TEM images of gold NPs synthesized by the author

Not only are gold nanoparticles now being synthesized on a large commercial scale, but they could also be synthesized on a laboratory scale. There is an image of gold nanostars which fabricated by the author in *Fig. 1.2*.

### ***1.2.2 Gold utilization in ancient civilization***

Utilizing of gold in ancient medicine has been common and it has been used topically or orally. Chinese philosophers believed that gold could rejuvenate man and called it the “elixir of life”. In the past, many alchemists did a lot of research on gold. They tried to extract gold from natural minerals. Many researchers in ancient times believed that with the help of chemistry, precious metals such as copper could be converted into gold. There is a lot of evidence that many chemical instruments for recovering gold was used by them. It is obvious that many laboratory techniques like heating, refluxing, extraction, sublimation and distillation was used by them to treat metals [14, 15].



**Fig. 1.3** Lycurgus cup kept in the British Museum

Using gold and silver in the manufacturing of ancient vessels and sculptures had been very common. The Lycurgus cup is a very old cup from the 4<sup>th</sup> century AD that is kept in the British Museum. The cup was purchased by British Museum from Lord Rothschild in the year 1958. This old cup represents the image of King Lycurgus. The most important issue about this cup is the color. Normally, it is green in the day light, but it turns red when light is radiated on the cup from inside. Research has shown that this effect is due to the presence of very fine particles of gold and silver in the structure of the cup. It is possible that gold and silver particles have deposited in the glass by heat reactions[16].

Gold particles was used widely in ancient vessels and glass in the Egyptian civilization. Using gold particles in sculptures and old glassy objects was favored due to the red color that is created by the passage of light through them.

### ***1.2.3 Gold in the spotlight of researchers***

The first official research of scientists on the color appearance of glass dates was back to 1612, when Florentine Priest Antonio Neri achieved interesting results during a visit to Venice and Antwerp. He notes that in ancient times, gold powder particles were added to glass during its manufacture. Johann Rudolph Glauber in 1659 during his pharmaceutical experiments concluded that colloidal solutions containing gold can produce a red color. However, he could not give a reason for this effect at that time. In the late 17<sup>th</sup> century, the production of purple and red colored glass by using gold powder became popular[17].

Professor Andreas Cassius, in his book published in 1685, described a gold precipitation method. His innovative method is called the “purple of Cassius”. He dissolved some tin and gold separately in Aqua regia and then mixed them together in a container and added some water to it. The color of the solution turned reddish-purple due to the deposition of gold NPs. The “Purple of Cassius” method became popular immediately and in the 18<sup>th</sup> century it was used as a decoration in most of Europe.

Michael Faraday (1797-1897) was the first researcher who worked on a suspension containing gold NPs and its electrochemical properties. Although most of his fame is in the field of electrochemistry, his research and effort to study the distribution of light in gold solutions is one of his most important achievements. In 1857 he published an article entitled: “experimental relations of gold and other metals to light” [18]. In this article, he expressed all his findings regarding the optical properties and

color appearance of gold colloidal solutions. He published articles on the colors of gold thin films as well as its colloidal solutions. Faraday was able to produce solutions with specific color by reducing the gold element into fine particles with the help of solid phosphorus in a solution of gold chloride. One of the most important things he mentioned in his achievements was that gold particles do not dissolve and are suspended in very fine suspensions (colloids)[19].

Faraday's theory was later confirmed by Tyndall. The Tyndall effect is a phenomenon in which colloidal particles scatter light passing through them. This effect can be seen in almost all colloidal suspensions. As a result, the Tyndall effect is used to check the colloidal nature of a solution. The intensity of the scattered light depends on the density of the colloidal particles and the frequency of light. Tyndall confirmed the presence of colloidal gold particles in solution using Faraday research and additional tests. Although much information about colloids was not available at the time of the above experiments, nowadays colloidal chemistry has become one of the large branches of chemical science [20, 21].

Gustav Mie (1869-1957), after Faraday and Tyndall, carefully studied the behavior of small metal particles when they encountered light emitted from different sources. Mie found that metal NPs such as gold NPs can both scatter and absorb visible light. He first studied the absorption of visible light by gold colloidal particles using electromagnetic theory [22].

Zsigmondy, who is known as one of the founders of nanoscience, succeeded at synthesizing gold particles as small as several hundred nanometers by using a method of gold chloride reduction with formaldehyde in 1903. He pointed out that gold particles have a negative charge on the surface, which makes them stable in solution.

### **1.3 Surface Plasmon Resonance (SPR)**

Gold colloids have a different color in comparison with bulk gold. These solutions are typically red. Where does this red color come from? In order to have a precise understanding of the colloidal gold solutions color, the surface plasmon resonance (SPR) phenomenon must be reviewed. The first studies and definitions related to SPR phenomenon have been done in the late 1970s. SPR occurs when the metallic particle size is smaller than the wavelength of the encountered visible light, or in other words, when the wavelength of the visible light is close to the vibration frequency of conduction electrons. [11, 23].

plasmons are defined as the collective and free oscillations of electrons in a metal conduction layer from one particle to another. The oscillations of the electrons are similar to the oscillations of the particles in the plasma environment, which is why this effect is called plasmon. Metals like Al, Cu, Au, Ag, In and Na are capable of generating the SPR when light is incident on the metal surface. The free electrons in the metal nanoparticles can form partial dipoles because of charge distribution. The formation of electron dipoles on the surface of particles is described by polarizability. The normal spatial configuration of electrons in the conduction band are changed as they are exposed to an electrical field, and form an electron cloud on a part of the atom surface. The presence of an electron cloud causes charge accumulation and create dipoles[24].

There are several noble metals whose NPs demonstrate SPR. Emitted light with a wavelength smaller or equal to the diameter of the particles creates an electric field, and consequently electrons converge along the direction of the electric field in a part of the particle surface and form a dipole. The movement of electrons on the surface of particles, cause an electron dipole and generate some resonances. These collective resonances from the conductive electrons are named Mie resonances or surface Plasmon resonances. SPR occurs at the metal–dielectric interface of plasmonic metals upon radiation of incident monochromatic light (using a prism is a solution to obtain monochromatic light) and a surface Plasmon wave (SPW) is emitted from surface. A configuration of SPR was proposed by Otto et al. where Incident monochromatic light will divide into three parts: (i) reflected light (ii) SPW (ii) Evanescent Wave (EW). *Fig. 1.4.* [25].

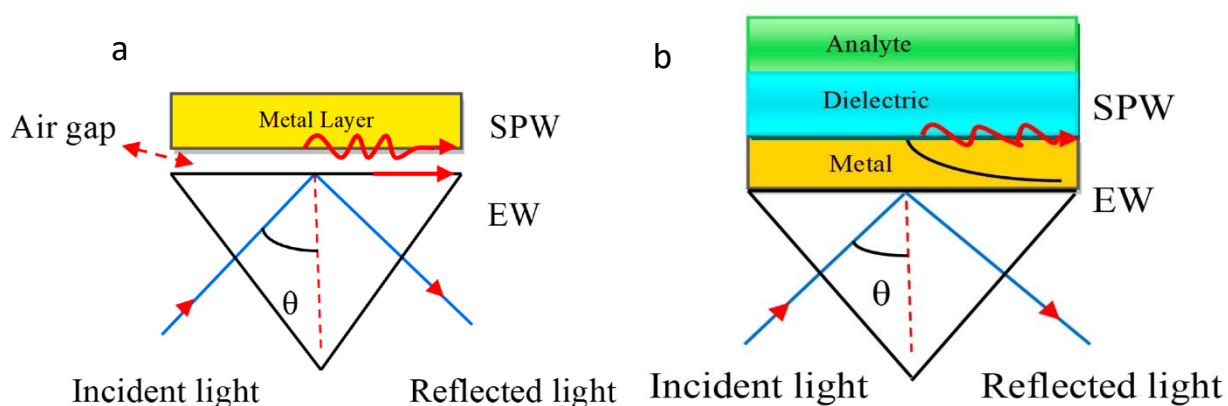


**Fig 1.4** Schematic view of Surface Plasmon wave emitted from surface of metals  
a) proposed by Otto et al. b) proposed by Kretschmann [25]

In Otto's configuration of the SPR setup there is an air gap between the prism surface and the metal layer. The SPW is generated on the surface of the air-metal interface. It is difficult to provide the proper air gap with defined dimension between prism and metal layer. Another configuration was proposed by Kretschmann where a 10-100 nm metal layer deposited on the prism. The SPW was generated on the interface between the metal layer and the dielectric media[25]. Fig 1. 4.

### **1.3.1 Mathematical models of surface Plasmon**

Several researchers from all over the world tried to elaborate a model related to this physical process at the nanoscale. There are many models that could describe atomic and electron behavior when exposed to electromagnetic radiation.

#### **1.3.1.1 Drude Model**

Lorentz, Drude and Sommerfeld discussed the relationship between electron vibrations and electric fields caused by radiation. The most important theories in the field of radiation and absorption of light to colloidal particles are related to the famous ideas and theory of Mie.

Sommerfeld introduced a model in 1900 to study the behavior, orientation, and motion of electrons. In the proposed model, the electrons are compared to pinballs, which are constantly vibrating and jumping. The following two equations represent the proposed Sommerfeld model [26]:

The first equation is for calculating an electronic equation of motion:

$$1) \quad \frac{d}{dt} \langle p(t) \rangle = q \left( E + \frac{\langle p(t) \rangle \times B}{m} \right) - \frac{\langle p(t) \rangle}{\tau}$$

The second equation includes the linear relationship between current density  $J$  and electric field  $E$ :

$$2) \quad J = \left( \frac{nq^2\tau}{m} \right) E$$

Where  $t$  is the time,  $\langle p \rangle$  is the average momentum per electron and  $q$ ,  $n$ ,  $m$ , and  $\tau$  are respectively the electron charge, number density, mass, and mean free time between ionic collisions.

### 1.3.1.2 Mie Model

Extinction, scattering and absorption of incident beams could be efficiently described by the Mie theory, which is one of the significant descriptions of scattering of light by a spherical particle. In fact, this theory is an analytical solution of Maxwell's equations. Mie theory is the best tool for calculating the scattering of light by spheres in a wide range of diameters and any wavelength of incoming light.

The Mie solution of Maxwell's equations (also known as the Lorenz–Mie solution, the Lorenz–Mie–Debye solution or Mie scattering) describes the scattering of an electromagnetic plane wave by a homogeneous sphere:

$$a) Q_e = Q_s + Q_a$$

Values commonly calculated using Mie theory include attenuation efficiencies coefficient  $Q_e$ , coefficients of scattering  $Q_s$  and absorption (electromagnetic radiation)  $Q_a$ .

The scattering and extinction coefficients can be represented as the series of spherical harmonics:

$$b) Q_s = \frac{2}{x^2} \sum_{L=1}^{\infty} (2L + 1) (|a_L|^2 + |b_L|^2)$$

$$c) Q_e = \frac{2}{x^2} \sum_{L=1}^{\infty} (2L + 1) R_e(a_L + b_L)$$

Here,  $x = 2\pi r/\lambda$  is the dimensionless diffraction parameter,  $R_e$  is the real part of the sum of complex numbers, and  $a_L$  and  $b_L$  are expansion coefficients [27].

Gold NPs, similar to other noble metal NPs, feature surface plasmon resonance bands. The origin reason of SPR is related to the collective oscillation of the conduction electrons across the particle due to the resonant excitation by the incoming photons. The resonance condition for Au NPs occurs at visible wavelengths of light and it depends on their size, and their color appearance is attributed to this phenomenon.

There are different factors that could affect the band intensity of SPR, like particle size, shape, structure, composition, and the dielectric constant of the surrounding medium. These factors affect the electron charge density on the particle surface. The mathematical model presented by Mie was briefly described above[28].

### 1.3.2 LSPR VS SPR

Surface Plasmon Resonance is a phenomenon that occurs at the interface of media one of which has to be a metal, and they must have different refractive indices. This phenomenon happens when polarized light is irradiated onto a metal film. In most instances, SPR occurs in metals like Ag and Au.

Unlike Traditional SPR, which is created at the interface of bulk metal, the localized surface plasmon resonance (LSPR) is created on metal NPs, typically silver and gold. A powerful resonance absorbance peak is produced in the visible range of light by LSPR.

When two or more plasmonic nanoparticles are placed close to each other (with edge-to-edge separations of one particle diameter or less) their surface plasmons couple as the conduction electrons on each particle surface oscillate collectively. This effect is similar to molecular orbital theory in that plasmon coupling results in the oscillating electrons assuming the lowest energy state, causing the plasmon resonance wavelength of the coupled particles to red-shift to longer wavelengths (lower energies). This coupling effect is responsible for the dramatic changes in the color appearance of the plasmonic nanoparticle solution.

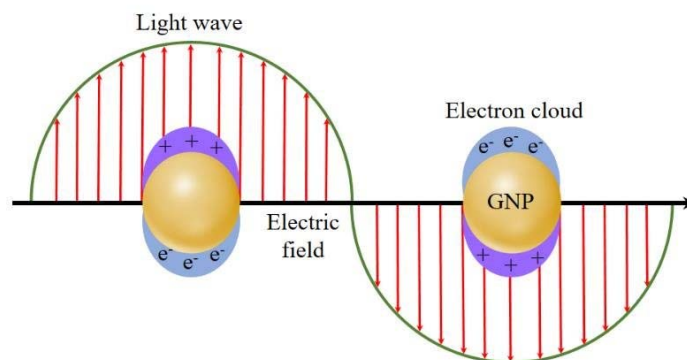


**Fig 1.5** Effect of electric field on electron orientation and formation of dipole

An alternative method to SPR is LSPR, which has been studied over the years and in these days is become the center of scientist attention. Local electromagnetic (EM) field enhancement results from excitation of the localized surface Plasmon resonance of metallic NP surfaces. LSPRs are non-propagating excitations of the conduction electrons of metallic NPs coupled to the electromagnetic field *Fig. 1.5*

Field enhancement is one of the factors that could have a dramatic effect on molecular adsorption on the surface of plasmonic structures. 35 years ago, it was first recognized that the Raman scattering intensity of pyridine on roughened Ag particles was enhanced by  $\sim 10^6$  with respect to operating at the resonance frequency of the sample molecule [29].

LSPR phenomena is a variation of SPR, and it has been noticed since the invention of nanofabrication techniques. LSPR occurs when surface plasmons are confined to a nanostructure much smaller than the wavelength of light, and they are localized around the nanostructure with a specific frequency. There are several 2-D nanomaterials used as substrates to enhance the sensitivity of LSPR sensors. Graphene, black phosphorous (BP), and transition metal dichalcogenides (TMDCS) such as  $\text{MoS}_2$ ,  $\text{MoSe}_2$ ,  $\text{WS}_2$  are some examples of compounds which are used by researchers.

LSPR is the main phenomenon responsible for the brilliant colors exhibited by Ag and Au nanoparticles under illumination. Michael Faraday was one of the first scientists who studied the effect of gold nanoparticles on the appearance color of colloidal solutions. He discovered the effect of gold nanoparticles on glass color for the first time in the 19<sup>th</sup> century when he examined the size and color of Au particles.

SPR measurements are more sensitive to bulk changes in refractive index due to the significantly shorter EM field decay length of LSPR. However, LSPR surpasses SPR on the absolute number of molecules detected on metal surface areas. This is the main advantage of LSPR in comparison with SPR. The range of Plasmon wave in SPR is subject to the bulk effect but the effect of bulk on localized plasmonic field could be neglected. *Fig. 1.6.*

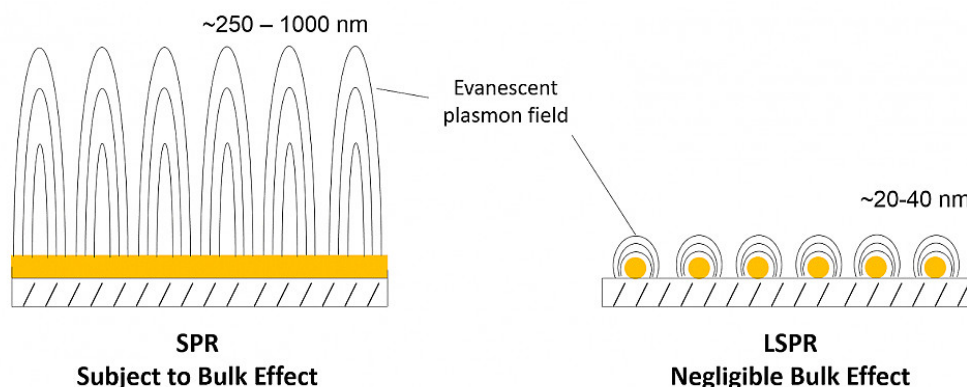


**Fig 1.6** Difference between evanescent plasmon field of SPR and LSPR

In order to understand LSPR it is better to review the physical meaning of the dielectric constant. The dielectric constant ( $\epsilon$ ) or relative permittivity is described as

a physical material property which affects the Coulomb force between two point charges in the material. It is a dimensionless constant factor by which the electric field between the charges is decreased relative to vacuum ( $\epsilon_0$ ). In particular, the dielectric constant is related to the polarity of the material and describes the behavior of the material in the presence of an electric field[30].

The relative permittivity of the medium is related to its electric susceptibility,  $\chi_e$  as:

$$a) \frac{\epsilon}{\epsilon_0} = 1 + \chi_e$$

Since the electric permittivity is a complex quantity, we can break it down into a real and an imaginary part:

$$b) \frac{\epsilon}{\epsilon_0} = \epsilon' - j\epsilon''$$

The complex dielectric function indicates that the material optical properties are dependent on the incident wavelength of light and can be described by  $\epsilon_{in} = \epsilon' + j\epsilon''$ , where  $\epsilon'$  and  $\epsilon''$  are respectively the real and imaginary dielectric permittivity. The real and imaginary components of the dielectric function of a harmonic oscillator can be described by the Lorentz model as:

$$c) \epsilon' = 1 + \frac{\omega_p^2 (\omega_0^2 - \omega^2)}{(\omega_0^2 - \omega^2)^2 + \gamma^2 \omega^2}$$

$$d) \epsilon'' = \frac{\omega_p^2 \omega \gamma}{(\omega_0^2 - \omega^2)^2 + \gamma^2 \omega^2}$$

Here,  $\omega_p$  is the plasma frequency,  $\omega$  is the frequency of the incident electric field,  $\omega_0$  is the natural frequency of the oscillator, and  $\gamma$  is a damping factor.

Note that since the polarization vector and the electric field are related by the electric susceptibility, we should analyze the magnitude and phase as:

$$e) \chi_e = \left( \frac{\epsilon}{\epsilon_0} - 1 \right) = (\epsilon_r - 1) - j\epsilon_i$$

From the above equations it can be deduced that permittivity depends on the frequency of the electric field as well as on the properties of the media, including the plasma frequency.

Media that exhibit the above behavior (dependency of permittivity on ongoing wave frequency) can act like a prism, turning white light into rainbow colors. The dielectric function clarifies the physical reason for the resonance condition and, ultimately, these equations display why the LSPR occurs when an electric field is incident on metals possessing negative real and positive imaginary dielectric constants. As the frequency of the incident electric field changes, so does the complex dielectric function, exhibiting the frequency dependence of the LSPR [31, 32].

Using the fundamentals of SPR, the technique of Raman spectroscopy can be easily explained. A surface plasmon is formed on metal surfaces such as gold under the influence of infrared radiation, and the reflective plasmon wave from the surface leads to the formation of Raman spectra. Beside traditional Raman spectroscopy, a modern technique called Surface Enhanced Raman Spectroscopy (SERS) has arisen, and it is explained on the basis of the LSPR principle. Metal particles intensify the surface Plasmon properties when placed less than 100 nanometers apart. Using the technique that we will discuss, it is possible to characterize particles, thin films, and monolayers deposited on the solid surface.

Nowadays, robust frameworks for the fabrication of two-dimensional substrates of nanomaterials are developed. These materials can be utilized in different devices such as batteries, transistors, detectors, ultrafast lasers, components of biological and physical sensors, photovoltaic cells, etc. There are thousands of scientific articles published on the specification and quality of 2D nanomaterials (graphene, Au and Ag films, BP and TMDCs) in several fields of science in the last decades. Alongside with Au and Ag, graphene is one of the most commonly used substrates in 2-D sensors. High stability and high affinity to adsorb biomolecules, high surface to volume ratio, high range of optical transparency (97.7%), and a potential for encapsulating molecules between graphene layers or attached on them, are important features of graphene. The highest sensitivity of graphene-based SPR sensor was reported by Wu and Chu et al. , who achieved up to 25% enhancement in SPR sensitivity [33].

## ***1.4 Gold nanoparticle monolayers using the Langmuir Blodgett technique***

### ***1.4.1 Preface***

A gold nanoparticle monolayer is a thin film with a 2-D lattice that is usually formed at the interface of liquid/gas with a single particle thickness. This structure is a key element and the building block of many sensors and devices in nanotechnology. There are several methods to prepare nanoparticle monolayers. One such method is the self-assembly of a gold monolayer that results from the binding of gold particles on a functionalized solid surface.

There are several complex methods to prepare monolayers of particles on a solid surface, such as self-assembly method, chemical vapor deposition techniques and electroless deposition methods. Another method is called Langmuir-Blodgett extraction and it is based on the transfer of a monolayer from the liquid/air interface to the solid substrate. The latter technique will be discussed further below.

### ***1.4.2 Particle preparation***

To prepare a Langmuir film at the interface of water/gas, we need molecules or particles that are hydrophobic or amphiphilic. Amphiphilic particles or molecules include dual properties in their chemical structure, both hydrophobic and hydrophilic parts are present in their structure. The hydrophobic head of particles and molecules usually orients towards the air due to the tendency to separate from the water environment and this causes the formation of a film at the interface. An example of amphiphilic molecules are surfactant molecules that are able to form thin films by self-assembling on the surface of water and other polar liquids. Janus particles could be considered amphiphilic particles if they combine hydrophilic and hydrophobic surfaces in their structure. Surface functionalization of particles can be tuned to provide the selective or specific structure required to synthesize sensors. Surface functionalization is a method for preparing a proper surface for chemical reactions, but sometimes synthesizing non-interactive molecules with neutral surface is advantageous for scientists [34]. Functionalization of molecules with other chemical ligands or groups could change their surface properties and cause molecules to act as non-interactive.[35, 36].

Researchers use different methods to make particles hydrophobic, hydrophilic or amphiphilic. Particles could be functionalized with organic groups and turn into molecules with different surface properties in comparison to their origin. In this study we used thiols as the type of functional group which are typical to functionalized gold surface.

### **1.4.3 Langmuir monolayers**

Insoluble molecules and particles could spontaneously form a very thin two-dimensional structure at the interface of liquids-gas which is called Langmuir film. This thin film is formed by means of a self-assembly phenomenon. In most cases, particles that make up the film do not interact chemically with the sub-phase. Therefore, they are able to be considered as free particles and form a thin film at the interface between the sub phase and air. Most particles that form a monolayer have hydrophilic and hydrophobic parts in their structure. A Langmuir film is an insoluble monolayer of atoms, molecules, or even nanoparticles spreading and floating at the liquid-gas interface (or liquid-liquid). Insoluble molecules and particles form a monolayer as a result of self-assembly at the surface of a liquid. The first person who talked about monolayers was Benjamin Franklin who, in 1770, described a simple monolayer formed by oil drops when spreading on the surface of lake. Franklin made some simple quantitative calculations. He found out that a teaspoonful (2 ml) of oil spreads over an area of half an acre. He calculated the thickness of film and realized that it would be around 2 nm. The formation of a film containing gold particles at the interface of water-air is an example of the self-assembly phenomenon. Gold nanoparticles form a 2-D lattice and a cohesive structure at the interface of water-air after injection on the surface of the liquid due to the gold particle surface chemistry [37].

The term Langmuir film dates back to 1917 when Irving Langmuir proved the feasibility of the method and showed that single layer films could be spread at the water/air interface by means of self-assembly phenomena. Langmuir films have been used in many fields for 100 years. In recent years Langmuir monolayers have been used by researchers to prepare nanostructures at the water/air interface and transfer them onto solid surfaces. Using organic ligands and molecules are reported more often than inorganic materials.

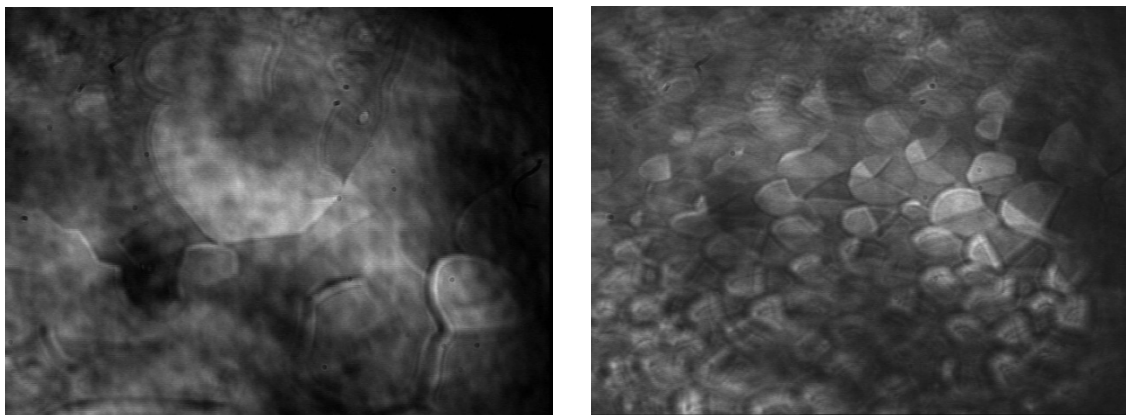


**Fig 1. 7** Langmuir Film of 1-monopalmitoyl-rac-glycerol formed at the interface of water/air. Captured with BAM (the field of view is 1mm wide) from author

Some of these studies include:

- 1- Use in the field of fabricating sensors with nanoparticles on glass and silicon wafers [38].
- 2- Use for preparing nanofilms to fabricate MIS (Metal-Insulator-Semiconductor)[39]
- 3- Use in biological sciences to produce monolayers consisting of lipids and fatty acids with long hydrocarbon chains to form monolayers on water surface[40].
- 4- Preparation of a glucose biosensor which is produced by using Poly (3-hexyl thiophene)[41].
- 5- Preparation of anti-reflection glass by depositing organic layers on it [42].

#### **1.4.4 Langmuir Blodgett technique**

18 years later than Irving Langmuir, Katharine Blodgett in 1953 showed the possibility of making multilayer films by attaching several single monolayer films on top of one another [43]. After the pioneering work done by Langmuir and Blodgett, it took almost half a century before scientists all around the world started to realize the opportunities of this unique technique. From that time, LB films and LB troughs have become popular for preparing monolayers and thin films of molecules and particles at the water/air surface [44].

The Langmuir-Blodgett (LB) methodology is based on the transfer process of a monolayer adsorbed at the water interface, Langmuir film, from the air-water interface onto a solid support by vertical dipping of the substrate immersed on the subphase. The free movement of particles at the water/air interface enable great

flexibility to prepare a 2-D solid layer. With the help of the trough barriers, particles can be arranged to a desired compression (*Fig 1.7*)

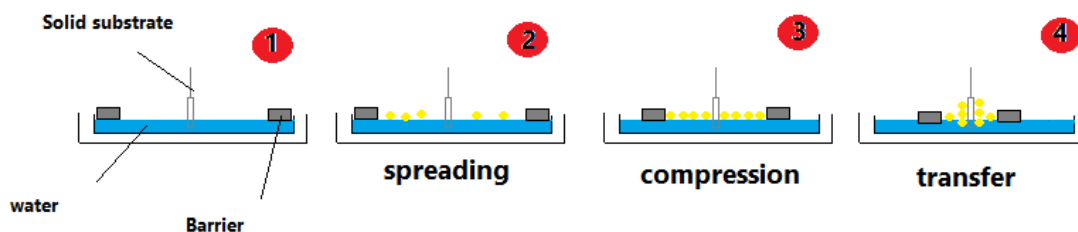


**Fig 1. 8** Schematic view of monolayer preparation at the air/water interface and transferring with the LB technique

The Langmuir-Blodgett (LB) methodology is based on the transfer process of a monolayer adsorbed at the water interface, Langmuir film, from the air-water interface onto a solid support by vertical dipping of the substrate immersed on the sub phase. The free movement of particles at the water/air interface enable great flexibility to prepare a 2-D solid layer. With the help of the trough barriers, particles can be arranged to a desired compression (*Fig 1.8*).

### **1.4.5 Langmuir Blodgett vs Langmuir Schaffer technique**

Langmuir-Blodgett and Langmuir-Schaefer are techniques used to transfer films or monolayers from the interface between liquids and gases to solid surfaces. For this purpose, the solid surface is contacted vertically or horizontally with the liquid surface and the particles at the interface are transferred to the solid surface. The same 2D patterns previously assembled at the interface are transferred to the solid substrate.

The most remarkable difference between these two methods concerns the extraction and transferring mechanism of the monolayer or particle film from the interface to the substrate. In the Langmuir-Blodgett method, the solid substrate is immersed vertically in the liquid and, upon extracting out from the liquid, the spread monolayer attaches and is transferred to the solid surface. In the Langmuir Schaffer method, the solid surface touches horizontally and parallel to the liquid surface and, upon contact, the film originally formed on the liquid surface is transferred to the solid surface. In the Langmuir-Blodgett method, all sides of the solid substrate are coated with the monolayer. In the Langmuir-Shaffer method, however, the film is placed on only one side of the substrate[45].

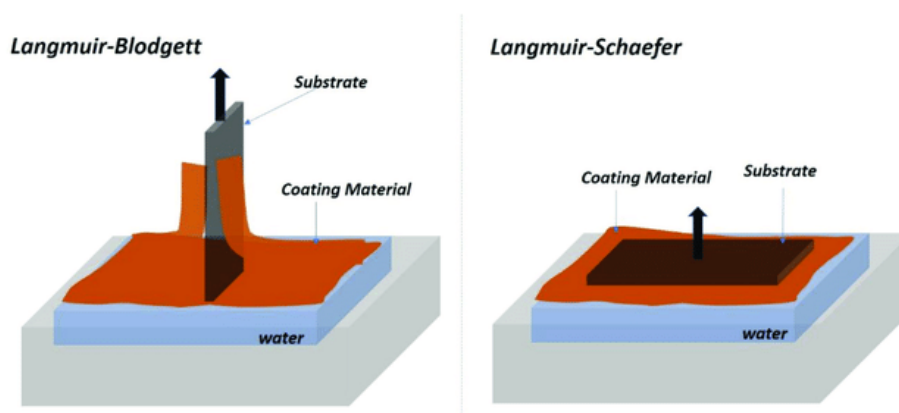


**Fig 1.9** Schematic of the Langmuir-Blodgett (Left) and Langmuir-Schaefer (Right) methods for transferring a thin film from the air/water interface. Adapted from [45].

For some substrates, for instance if they are functionalized with organic molecules and ligands for which direct contact with water is to be avoided, using the Langmuir-Schaefer technique is required to minimize substrate damage.

### **1.4.6 Langmuir Film Balance**

A Langmuir Film Balance is an apparatus used to assemble and process molecules and particles at the liquid/gas interface. This device has the ability to control and modify the surface pressure of liquids allowing to form cohesive and dense lattice structures of particles. Not only can LB troughs form a monolayer at the interface, but these monolayers can also be transferred, using a dipping system in the LB Trough, to the solid surface.

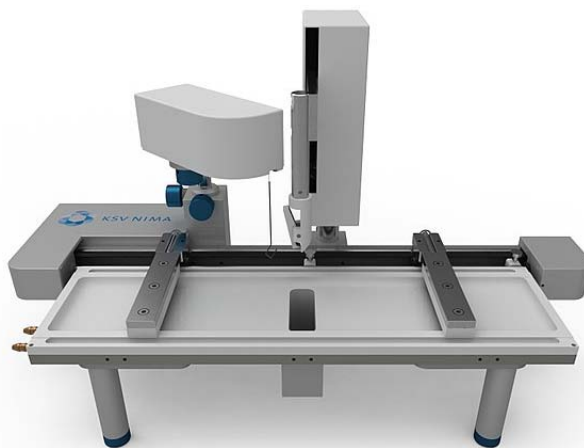


**Fig 1.10** Commercial Langmuir trough, adapted from KSV NIMA.

Early version of Langmuir troughs were made of metal but, because of contamination problems and difficulty of cleaning, they changed to glass with wax coating in order to prevent contamination. In recent days, Langmuir troughs are made of Teflon, a hydrophobic and chemically inert material. All in all, some troughs are still made from metals or glass with Teflon coatings. Surface tension and surface pressure are crucial in the preparation of monolayers with the Langmuir technique. In the following we will describe the above parameters and techniques involved in Langmuir monolayer preparation and characterization.

### 1.4.7 Surface tension

Cohesive forces between liquid molecules in the surface result in a phenomenon called surface tension. The top layer molecules of the liquid are in contact with liquid molecules from the layer below and neighboring molecules at the interface. Since there are no liquid molecules on top, molecules from below and surroundings cause and extra cohesion [46]. As a result, it is more difficult to move an object through the interface than to move the object when submerged. The surface tension is measured with the Wilhelmy plate method in Langmuir troughs. The plate could be made from various material, such as filter paper, glass or platinum [47].

In the Wilhelmy plate method, in order to measure the liquid surface tension, a clean plate of the filter paper, glass or platinum is submerged vertically down to half its height. When the liquid completely wets the surface of the sheet (contact angle = 0), near the three-phase region, the surface tensile force is vertical (*Fig 1.11*).

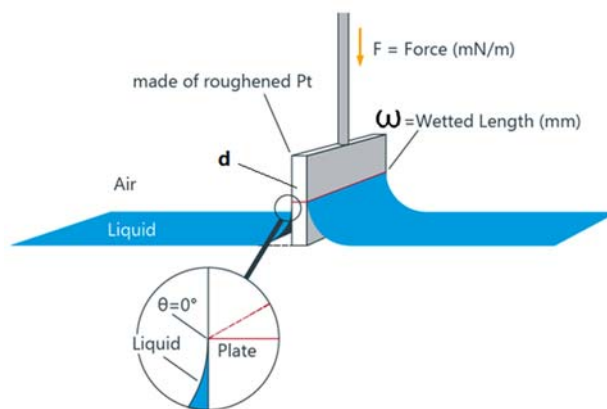


**Fig 1.11** Schematic diagram of the Wilhelmy plate mechanism

Surface tension  $\gamma$  of a liquid is the force per unit length actuating on the plate, and is calculated as follows:

$$\gamma = \frac{1}{\cos \theta} \frac{F}{L}$$

Where F is force, L is the wetted perimeter ( $2\omega+2d$ ),  $\omega$  is the plate width, d is the plate thickness, and  $\theta$  is the contact angle between the liquid and the plate surface. The units of the surface tension in the SI are Newton per meter (N/m). In practice, plates with perfect wetting are used and the wetting angle is not measured and complete wetting of the plate is assumed ( $\theta=0$ ). (Fig 1.11).

### **1.4.8 Surface pressure**

Surface pressure is the force which is applied per unit length on a floating material at an interface. In other words, the surface pressure is the decrease in surface tension of a given interface state (for instance, in the presence of a spread monolayer) with respect to a reference state (for instance, the clean interface).

In the Langmuir film balance, the surface pressure ( $\pi$ ) is calculated by subtracting the surface tension of the interface without any monolayer ( $\gamma_0$ ) from the surface tension in the presence of a monolayer( $\gamma$ ).

$$\pi = \gamma_0 - \gamma$$

The surface pressure is, thus, directly related to the change in surface tension due to the addition of the monolayer.

### **1.4.9 The surface pressure-area isotherm**

The surface pressure-area isotherm is the most basic indicator of the monolayer state and it is calculated from the surface pressure as a function of the surface area occupied, at a given temperature, by the molecules or the particles that form the monolayer. In a typical surfactant isotherm there are three phases found upon increasing the surface pressure by compressing the monolayer: Gas phase (G), liquid phase (L), and solid phase (S). By decreasing the area, the surface pressure increases and particles or molecules at the interface compact into denser states until reaching the point where the monolayer collapses and multiple layers overlap. The collapse point can be observed through real time monitoring of BAM images

during preparation of monolayer as the appearance of very bright regions (see below).

The phase behavior of the monolayer is mainly determined by:

- physical and chemical properties of the molecules or particles
- liquid temperature and pH
- chemical composition and specification of sub phase liquid
- Compression speed, which should be slow as we are assuming close to equilibrium state.

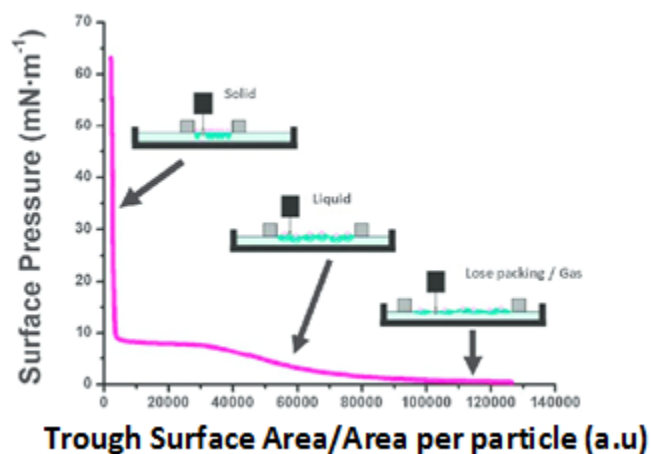


**Fig 1. 12** Surface pressure—area isotherms of a Langmuir film with molecules in different phases.[48]

Upon decreasing the area, there is an increase in the surface pressure *Fig. 1.12*, and we can observe three regions in this graph, corresponding to different compression trends and different monolayer phases. The trend of the graph in the gaseous phase is steady and stable until particles move closer to each other and reach the liquid phase. In this phase, a dominant feature is the interaction between particles and the onset of intraparticle forces. In this phase, by decreasing the area, there is remarkable change in the trend of the surface pressure, which is due to said interactions. Below a certain area per molecule, there is a drastic change in the slope of the surface pressure when particles are packed densely in a 2-D lattice. Eventually, the monolayer collapses into three-dimensional aggregates and, after that, there is no remarkable change in the graph, which is seen as flat regions or bumps in the isotherm.

### 1.4.10 Brewster Angle Microscope

A Brewster angle microscope (BAM) is an apparatus to study and visualize thin layers like Langmuir films on the surface of liquids. Brewster-angle microscope is based on the principles of the refractive index for a given medium. Laser beam irradiates from a source to the surface of water after passing through a polarizer aligned with the plane of incidence and hits the interface at the Brewster angle. An image of the reflected light is focused to a CCD camera with a microscope objective. An analyzer may be used to modulate the reflection in the case of monolayers with anisotropic optical properties [49, 50]. The Brewster angle ( $\theta$ ) for the water/air interface is around  $53^\circ$  and there is no reflected light under these conditions [51]. However, adding a film at the air-water interface causes light reflection as a result of changing the refractive index ( $RI$ ). The reflected light is displayed as bright areas corresponding to assembled particles or molecules on the surface. A light source of BAM is usually consist of Class 50 mW laser and classified as class (*IIIb*) broadband laser[52].

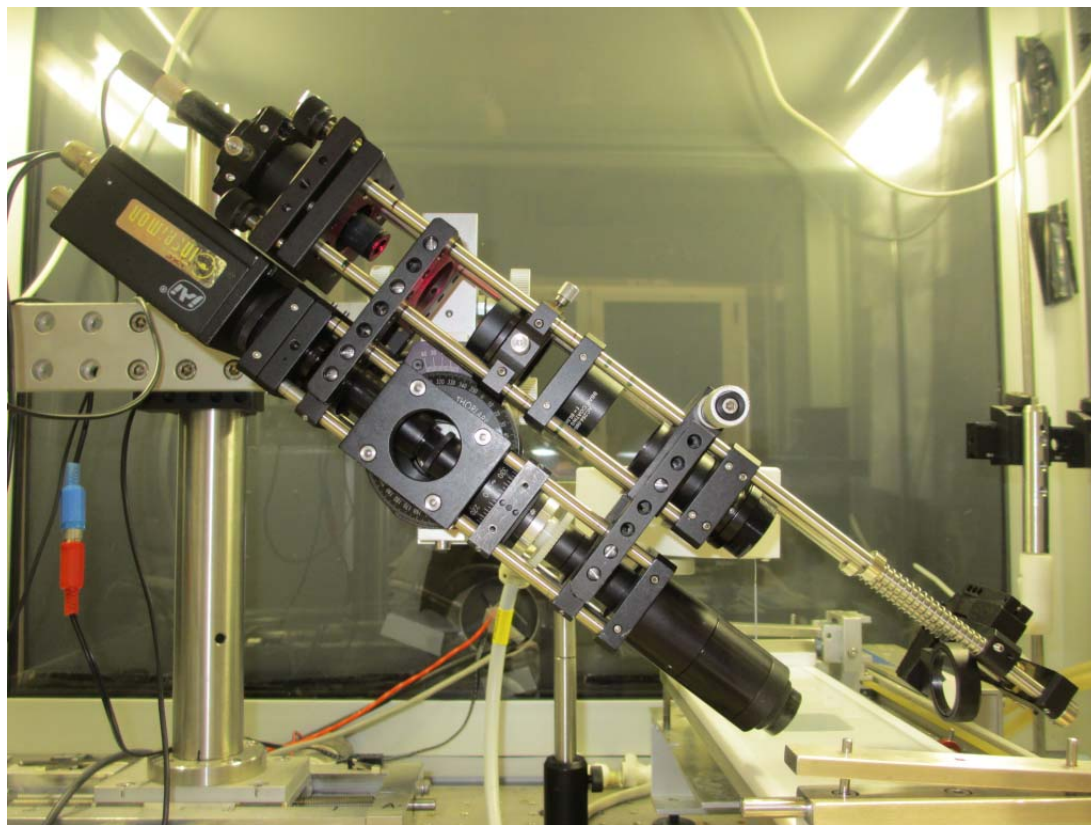


**Fig 1. 13** Brewster Angle Microscope (BAM) which has been used by the author in this research

Different phases of monolayers and film preparations at the air/water interface can be monitored precisely in real time with BAM. BAM provides information on homogeneity, phase behavior, and film morphology.

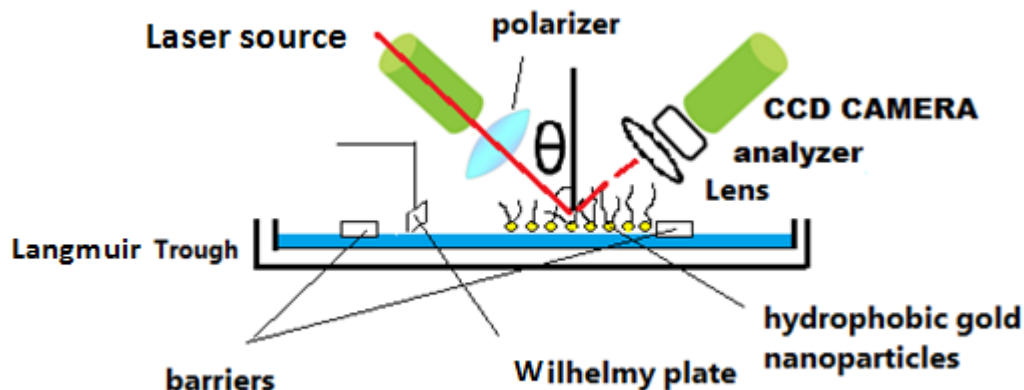


**Fig 1. 14** Schematic of a Brewster Angle Microscopy

Under the condition of decreasing the surface area increasing the surface pressure ( $\pi$ ) the phase of a monolayer changes (Sec.1.4.3). The unsuspected morphological variety of the domain structure depends largely not only on the chemical structure of the amphiphilic molecules, but also on the system parameters, such as surface pressure and pH of the sub phase. *Fig 1.15* shows a phase transition region during the compression isotherm of a 1-monopalmitoyl-rac-glycerol monolayer. There is a morphological change in the monolayer upon decreasing the area. Each round domain in the *Fig.1.15* is related to the orientation of alkyl chains. 1-monoglyceride domains are subdivided into seven segments with different brightness level. The shape of the cardioid domains is caused by the anisotropy of the line tension. A remarkable feature of the circular domains is a sevenfold substructure. The different brightness of subdomains are due to regions of different molecular orientation. Gelhert 1997. The angle between segments and their rotational configuration indicates that the lattice structure influences the inner structure of a condensed phase domain [52, 53].

There are several parameters which affect the packing density of molecules and particles at the water/air interface. Temperature and pH of the sub phase are the most significant factors and may cause major changes and transform the domain shape. By using BAM, we can study and monitor amphiphilic monolayers at equilibrium or non-equilibrium conditions [52].

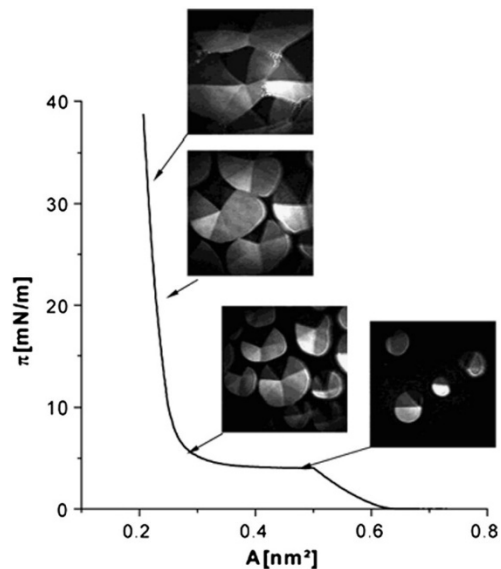


**Fig. 1.15** Effect of surface pressure on forming 1-monopalmitoyl-rac-glycerol monolayers, adapted from[52]

Nanofilm-Ultra BAM was introduced in recent years as a modern generation of Brewster Angle Microscope. This device is equipped with advanced imaging optics that provide fully focused images at 30 frames per second. Advantages of modern BAMs are the high resolution and low noise of the images, and molecular orientation in the monolayer can be easily captured by the device.

## ***1.5 Raman Spectroscopy***

### ***1.5.1 Preface***

Raman spectroscopy is a molecular spectroscopy technique (that deals with the identification of molecules, not atoms) that has found several applications in various fields of research. Raman technique, unlike the early years of its invention, has become very common today and has been widely used in basic and applied sciences. In fact, the Raman technique owes its widespread use to the many device advances that have been made in the field to date, making it even simpler, more accessible, and more cost-effective. Of course, despite advances, in some cases it is still difficult to interpret Raman spectra and requires special skills to avoid misinterpretations.

### ***1.5.2 Raman Technique background and history***

In 1928, an Indian scientist called C.V. Raman, discovered that the wavelength corresponding to a small fraction of the radiation scattered by certain molecules was different from the wavelength of the original radiation (i.e., inelastic scattering occurs). Such wavelengths vary depending on the molecular structure of the compounds. Raman spectroscopy is based on the analysis of these differences to determine the molecular structure of different compounds. In the other word Raman spectroscopy is the study of interaction between light and matter in which light is scattered inelastically. In Raman spectroscopy experiments, single-wavelength photons (called monolithic light in the visible region) are focused on the sample, and a laser is commonly used as a high-intensity monolithic source. Photons interact with molecules and are reflected, absorbed or scattered. The basis of Raman spectroscopy is the study of scattered photons from materials[54]. The Austrian physicist Adolf Smekal also theoretically described the technique in 1923. Concurrent with Raman, two Russian researchers, Leonid Mandelstam and Grigory Landsberg, were working on the technique but did not publish any results. Raman won the Nobel Prize in 1930 [55].

### 1.5.3 Scattering of light in RAMAN

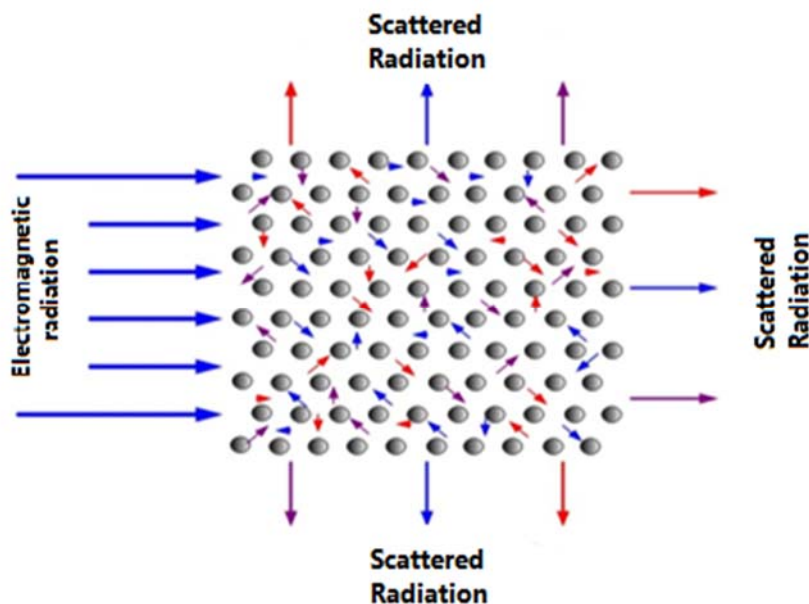


**Fig. 1. 16** Scattered radiation from particles upon Electromagnetic radiation

When electromagnetic radiation passes through a transparent medium, existing species scatter part of the beam in all directions (*Fig. 1.16*). Due to the collisions of light with matter, we will have two types of scattering according to the wavelength of the scattered radiation:

1. Rayleigh scattering, which is caused by particles that are much smaller than the wavelength of the radiation. Due to this type of scattering, the radiation wavelength does not change and is also classified as elastic scattering. The most obvious example of this type of scattering is the blue color of the sky, which occurs due to the scattering of shorter wavelengths in the visible spectrum.
2. Raman scattering, in which the initial wavelength changes due to the transfer of energy between photons and matter, and the wavelength increases due to energy loss, or the wavelength decreases due to energy capture. The magnitude of these energy changes (whether decreasing or increasing) is proportional to the frequency of the molecular vibrations of the light scattering species. Raman scattering will be divided into two general categories. The first group, in which scattered radiation has a longer wavelength (less energy) than the original radiation, is called Stokes, and the second group, in which it has a shorter wavelength (more energy) than the original radiation, is known as anti-Stokes [55, 56].

Stokes lines in Raman diagrams are more intense, which can be explained by the higher probability of their occurrence, because usually, due to exposure to the material environment, energy loss by photons is more likely than energy reception. Another point to consider is that the amount of Raman shift is independent of the laser wavelength used to excite the sample. It should also be noted that Rayleigh scattering is located exactly at the wavelength equal to the source wavelength, its displacement is zero and its intensity is much higher than the Stokes and anti-Stokes lines.

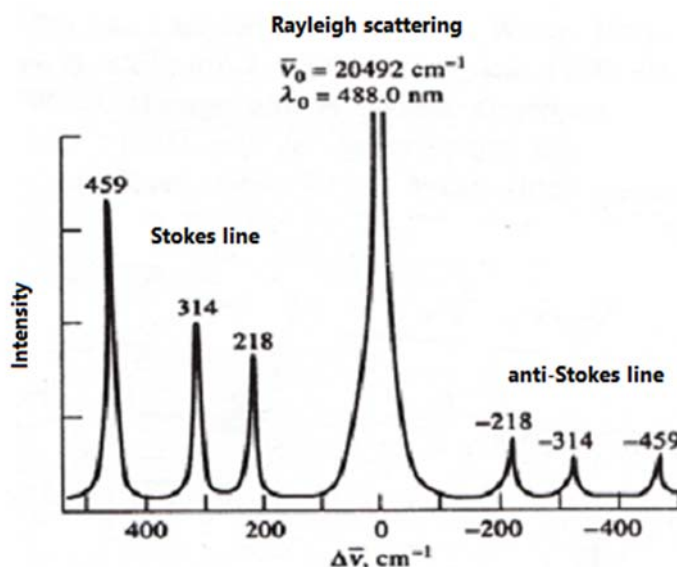


**Fig.1. 17** Example of Raman spectrum of CCl<sub>4</sub> using a laser with a wavelength of 488 nm. The numbers above each peak are the amount of Raman displacement

### 1.5.4 Infrared Spectroscopy (IR)

Infrared spectroscopy (IR) is a method similar to Raman spectroscopy and both these techniques are based on the interaction of electromagnetic waves with the lattice waves or phonons. In the following, considering the main similarities between these two methods, we will review the method briefly.

Infrared spectroscopy is based on the absorption of radiation and the study of vibrational changes of molecules and polyatomic ions. This method is a powerful technique for determining the structure and measurement for the detection of chemical species. This method is also mainly used to identify organic compounds, because the spectra of these compounds are usually complex and have a large number of peaks that can be used for comparative purposes[57].

There are two types of vibrations in molecules, which are called tensile and flexural vibrations. Tensile vibration is divided into symmetric and asymmetric. Whenever an asymmetric tensile half-cycle occurs, the dipole moment changes in one direction, and in the other half-cycle, the bipolar moment shifts in the opposite direction. Thus, the dipole moment fluctuates with the vibrational frequency of the molecule (this oscillation causes the molecule to rise to the infrared absorption band and is therefore called an infrared activator).

The interaction of infrared radiation with a sample changes the vibrational energy of the bond in its molecules and it's a good way to identify the functional groups and the molecular structure. The condition for the molecule to absorb infrared energy is that the bipolar torque changes during vibration. In the electromagnetic spectrum, the range between  $0.8\text{-}1000\ \mu\text{m}$  is related to the infrared range, but the range used for chemical analysis is  $0.8\text{-}50\ \mu\text{m}$ . The region above  $50\ \mu\text{m}$  is called the far infrared area, the region between  $0.5\text{-}0.2\ \mu\text{m}$  called near infrared area, and the region between  $8\text{-}25\ \mu\text{m}$  is called the fingerprint region *Fig 1.18*.

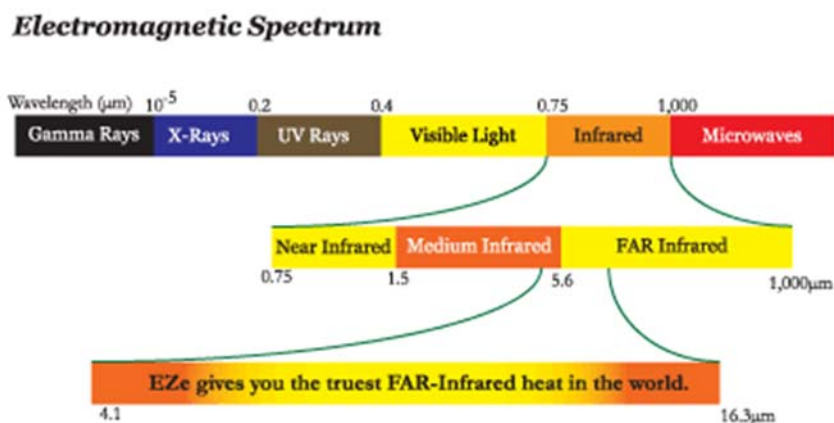


**Fig. 1.18** Range of wavelength that is in IR spectroscopy

In conventional IR instruments, the electromagnetic spectrum extends from visible to infrared. In the mentioned method, a small portion of the radiation reaches the detector and is recorded. In this case, the resulting spectrum will be recorded in the specific frequency or wavelength range. In the case of Fourier transform IR (FTIR) all the wavelengths of the spectral region are analyzed at the same time. In conventional methods, however, only a small fraction of the wavelengths reaches the sample at a time. Therefore, the speed, resolution and signal-to-noise ratio in the FTIR method are significantly superior to the conventional IR method [58, 59].

### ***1.5.5 Differences between Raman and infrared spectroscopy***

There are many similarities between the two methods as The Raman scattering spectrum and the infrared spectrum are often very similar for a particular species. But it should be noted that, despite these similarities, the two techniques are different in basic principles, so that they are usually used as a complement to each other.

IR spectroscopy is based on the changes of dipole moment of molecules during their interaction with the IR radiation, while Raman is based on the change of electric polarizability of the molecules. In the infrared spectroscopy method, one of the necessary conditions for a particular bond to be active is that, due to the absorption of radiation, a net change in the dipole moment occurs. Unlike infrared spectroscopy, electric polarizability of molecules is active and dominant in the Raman technique, molecular polarizability is changed due to radiation absorption. Accordingly, a link can be active in the Raman technique, infrared spectroscopy, or both, and this will cause similarities or differences in the spectra of the two methods. All in all, the infrared technique has a slight advantage over Raman. Raman peaks are usually weak and defect lines are dominant. The Raman device setup is usually more expensive. In Raman measurement, a fluorescence light may be emitted from the sample in a specific laser wavelength, and it may affect the spectra. A Raman advantage over infrared is the elimination or simplification of sample preparation methods in the case of using complex biological cells. The other advantage is the ability to detect oscillating modes of molecules which are not detected by infrared. Finally, we note that Raman spectroscopy is a non-destructive method and does not even require direct contact with the specimen [60, 61]

### ***1.5.6 Theoretical principles of EM and molecular polarization***

Suppose that a monochromatic light wave (electromagnetic wave) is propagating in the direction of the z axis, while its electrical component oscillates in the direction of the x-axis (*Fig 1.19*). The intensity of its electric field ( $E_x$ ) at time t will be expressed as:

$$a) E_x = E_x^0 \cos(2\pi V_0 t)$$

Where  $E_x^0$  is the amplitude of the wave or the maximum value of the electric field and  $V_0$  is the frequency of the electromagnetic wave. Also assume that a molecule with a natural frequency  $V_v$  is vibrating. The normal vibration vector or normal mode, ( $q_v$ ), has an amplitude that changes with time as:

$$b) q_v = q_v^0 \cos(2\pi V_v t)$$

As mentioned above, when an electromagnetic wave interacts with a molecule, it polarizes the electrons of the molecule, and this polarization induces a dipole moment ( $\mu$ ) in the molecule. This dipolar moment is defined as follows:

$$c) \mu = \alpha E$$

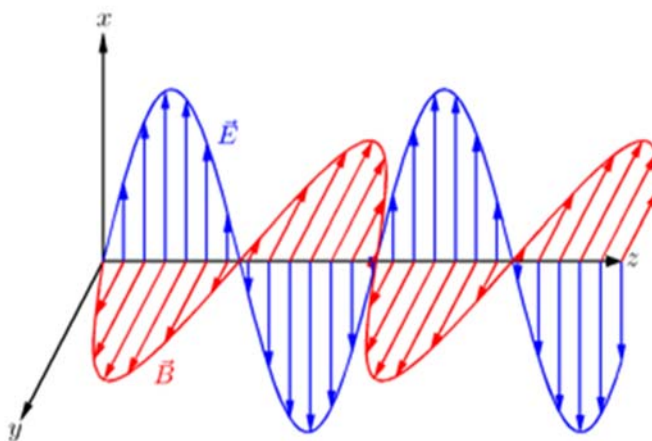


**Fig. 1.19** The electric and magnetic fields that form an electromagnetic wave propagating in the direction of the z axis

Here,  $\alpha$  is a proportionality constant called the polarizability of the bond and it is a measure of the amount of bond deformation in the electric field. For a bond to be active in Raman, its polarization needs to change as a function of the distance between the cores (bond length). The polarizability can be expressed as a Taylor series:

$$d) \alpha = \alpha^0 + \left( \frac{da}{dq_v} \right) + \dots$$

The induced magnetic moment has an oscillating motion and it emits light with three different frequencies (scattered light). These three different frequencies will be obtained by using Equation d) and placing Equations a) and c) in it:

$$e) \quad \mu = E_X^0 \alpha^0 \cos(2\pi V_0 t) + E_X^0 \left( \frac{dx}{dq_v} \right) q_v^0 \{ \cos[2\pi(V_0 - V_v)t] + \cos[2\pi(V_0 + V_v)t] \}$$

As shown in Equation e), the scattered light will include three frequencies, namely,  $V_0$ ,  $(V_0 - V_v)$ , and  $(V_0 + V_v)$ . In other words, the scattered light will have three components with different frequencies: one equal to the frequency of the origin light (Rayleigh), one with a higher frequency of incident light which is equal to the natural frequency of molecular vibrations (anti-Stokes) and the last with a smaller frequency than that of the original light (Stokes). Therefore, in the case of Stokes and anti-Stokes peaks, we can expect their intensity to increase with increasing temperature, because with increasing temperature, the amount of molecular vibrations also increases, and more fractions of molecules will be in the first vibration-excited state.

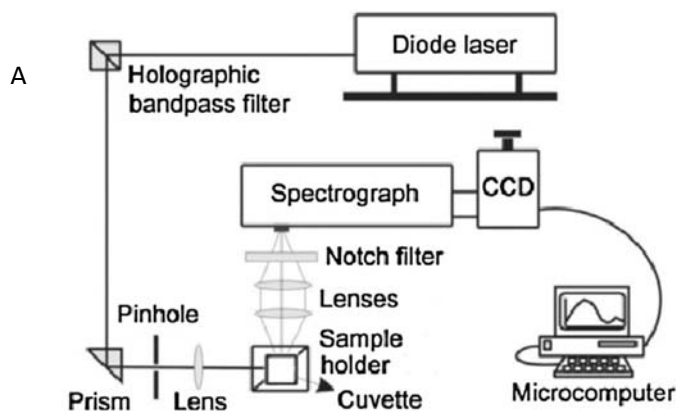
### **1.5.7 Raman Device Components**

The Raman device includes the Raman spectrometers and an optical microscope which is coupled to them. The most important components of a Raman device are its radiation source and the spectrometer system. The sources used in the Raman method are mostly lasers, because their intensity is high enough to create an acceptable Raman scatter. The most common laser sources used are: Argon-ion laser with wavelengths of 488 and 514.5 nm, Krypton-ion with wavelengths close to 531 and 647 nm, Helium / Neon with wavelength of 863 nm, diode laser with wavelength 782 and 830 nm and Nd/YAG (Neodymium-doped Yttrium Aluminum garnet; Nd:Y<sub>3</sub>Al<sub>5</sub>O<sub>12</sub>) laser with a wavelength of 1064 nm. Since the source frequency has a significant effect on the intensity of Raman peaks of a species, the source used is selected according to the sample conditions. For example, fluorescent species generally require sources with wavelengths in the infrared range, such as Nd/YAG, which do not have enough energy to excite the species and create fluorescence in them. In this way, fluorescence disturbance is minimized [62]. Of course, it should be noted that UV sources can also be used in

the Raman method, but due to a series of limitations, including their high energy content that sometimes causes the destruction of the sample, as well as the dangers of using UV light, the latter is not widely used.

Recent Raman devices are mainly based on two general types of spectrometers; one is Dispersive Spectrometers and the other is Fourier Transform Spectrometers. The use of a spectrometer in a Raman device is done for two main reasons:

1. In order to separate the radiation caused by Rayleigh scattering from Raman radiation, we should filter Elastic scattered radiation at the wavelength corresponding to the laser line (Rayleigh scattering) with spectrometer device.
2. Analysis of collected optical signals.



## FT-Raman

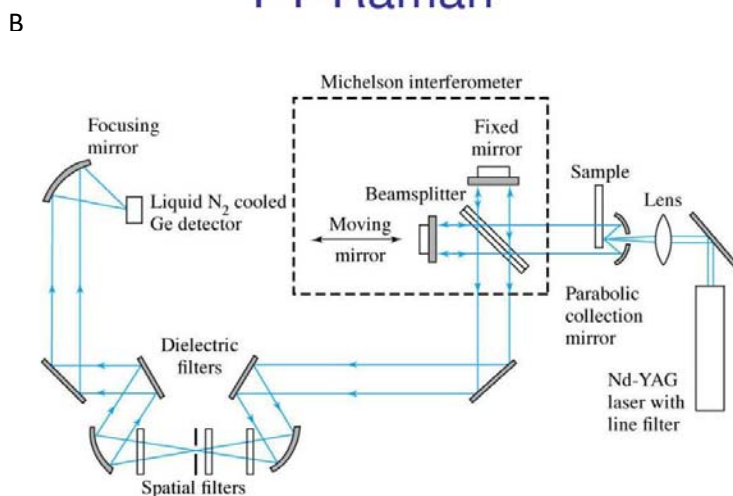


**Fig. 1. 20** Schematic view of A) Dispersive and B) Fourier-Transform Raman [63]

We need to focus on the wavelengths that have a frequency change, which are identified as Raman signals. The Raman scattering cross section is very small and the most difficult step in this method is to separate the elastic beams from the modified Raman frequency beams. In the past, holographic grids and multiple steps were used to achieve a high degree of laser beam rejection. In the past, photo multipliers were the detectors of choice for dispersive Raman devices, resulting in longer data collection times. Nevertheless, modern devices use notch or edge filters almost universally to repel laser beams, and spectrographs, whether Axial-Transmissive (AT), Czerny-Turner (CT) or Fourier transform spectroscopy, and CCD detectors.

The Raman spectroscopy method has found wide applications in the field of nanoparticle identification and determination, among which the following can be mentioned:

- a. Identification of organic and inorganic compounds that are attached to particles of RAMAN [64].
- b. Determining the boundary conditions for the electric field near the surface[65].
- c. Using Raman spectrometer to analyze nanoparticles and carbon nanotubes[66].
- d. Determination of carbon nanotube diameter and determination of diameter of some mineral nanoparticles[67].
- e. Determination of carbon chirality (chiral carbon is carbon that has four different groups of atoms attached to it).
- f. Determining the structure of different carbon nanomaterials and allotropes.

## ***1.6 Surface Enhanced Raman Spectroscopy (SERS) Technique***

### ***1.6.1 Preface***

First observation of Enhanced Raman spectra dates back to the year 1974 when Martin Fleischmann, Patrick J. Hendra and A. James Mc Quillan studied pyridine on roughened silver at the Department of Chemistry at the University of Southampton, UK. They encountered a high enhancement in a part of the

spectrum. However, there is not any scientific reason for it in their publication. At that time, the authors did not recognize that these spectra were due to any unusual, enhanced, or new phenomena. The first discovery of SERS dates back to 1977. David L. Jeanmaire described the resonance of Raman peak in his publication [68].

SERS is an abbreviation, which derived from:

Surface (S): SERS is a surface spectroscopy technique, unlike Raman which focuses on the bulk material; the target molecules of SERS must be on (or close to) the surface. This is a significant difference between SERS and classic RAMAN.

Enhanced (E): Plasmon resonances in the metal substrate is the reason for signal enhancement. The plasmon effect of some metal surfaces like gold and silver is the basis of signal enhancement in the SERS technique.

Raman (R): This technique consists of measuring the Raman signals of molecules (the SERS probes or analytes). The basis of Raman spectroscopy concerns inelastic light scattering and, when applied to molecules, it provides an insight into their chemical structure that could be gathered by detectors and analyzed by comparing with reference Raman libraries.

The final S in SERS can stand for Scattering or Spectroscopy, depending on whether one prefers to emphasize the optical effect (scattering) or the technique and its applications (spectroscopy).

Surface Enhanced Raman Spectroscopy (SERS) is a technique in which the Raman spectrum is used to identify molecules that are adsorbed on the surface of metals. The main advantage of this method is the increased intensity of Raman peaks, which can be amplified from  $10^4$  to  $10^{14}$ , and therefore it may be even used to identify single molecules.

### ***1.6.2 SERS Scattering Phenomena***

Raman scattering is dramatically increased by adsorption of the target analyte or molecule on the metal substrate. This effect is very strong in Silver, and it is also found in Gold and Copper, but it is insignificant in other metals. Two main mechanisms have been introduced to justify this effect: charge transfer effect (CT) and electromagnetic field effect (EME). The effect of charge transfer is also called chemical effect [69].

In both mechanisms, the presence of a rough surface is necessary to increase and enhance the signal. In the electromagnetic field effect, the intensification of the superficial plasmon is considered as the cause of signal enhancement. Surface plasmon forms when high-energy radiation or electrons hit the metal surface (see sec. 1.3).

As we mentioned above the presence of sharp and rough surfaces is essential for the EME effect because the electric field near the sharp edges of the surfaces increases greatly. Due to the transfer of charge, the increase of the Raman signal is not related to the increase of the magnetic field. Under special conditions, the adsorbed molecules can interact with the metal surface and increase the polarizability of the molecule. In fact, according to this mechanism, the orbitals of the adsorbed molecule are expanded due to the binding to the electrons of the metal conduction band and make a chemical bond with them. All in all, the affinity of target molecules and metal conduction band electrons depends on the chemical nature of them. Chemisorption and physisorption happen as a result of the mentioned affinity between molecules and SERS substrate.

We can compare the physics of electromagnetic wave enhancement in normal Raman and in SERS. A laser radiation, oscillating with frequency  $\omega_L$  is radiated to the molecule with an electric field  $E(\omega_L)$ . The input laser contacts the metal surface and causes a dipole oscillating at the Raman frequency (vertical red arrow),  $P(\omega_r)$ .  $P(\omega_r)$  is equal to the Raman polarizability tensor ( $\hat{\alpha}_r(\omega_r, \omega_l)$ ) times  $E(\omega_L)$ . The Raman power ( $P_{\text{Raman}}$ ) in this case is equal to the square of the dipole (Fig 1. 21). Surface Enhanced Raman Scattering (SERS) occurs when a molecule is placed in the domain of a plasmonic substrate. The electric field that affects the molecule is  $E_{LOC}(\omega_L)$ , and it is much higher than the input laser  $E(\omega_L)$  as a result of plasmonic resonance. The local field enhancement is introduced as  $M_{LOC}^Z(\omega_L)$  and the enhancement of dipoles that cause Raman radiation is introduced as  $M_{LOC}^Z(\omega_R)$ . The total electromagnetic enhancement factor is identified as  $G_{EM}^{SERS}$  and it is calculated by multiplying  $M_{LOC}^Z(\omega_L)$  and  $M_{LOC}^Z(\omega_R)$ . There is a principal effect of localized surface plasmon in SERS technique as described, and according to that, the increase in SERS sensitivity in comparison to traditional Raman is remarkable. A mathematical model is described in Fig 1.21.

SERS technique is a very sensitive method that also has the ability to detect individual molecules. The SERS method is not destructive and has a very high spatial resolution. The enhanced signal is highly dependent on the metal material

and the substrate fabrication, so sample preparation is a very crucial step and requires special skills and tools to prepare the SERS sample.

Tip-Enhanced Raman Spectroscopy (TERS) is an advanced SERS technique in which an atomic-scale pin is coated with SERS-like active metal such as gold. This technique, combines the sensitivity of Raman spectroscopy, the lateral resolution of SPM, and the sensitivity of SERS. TERS occurs near the tip of the pin, resulting in a signal with a lateral resolution of about 20-30 nm.

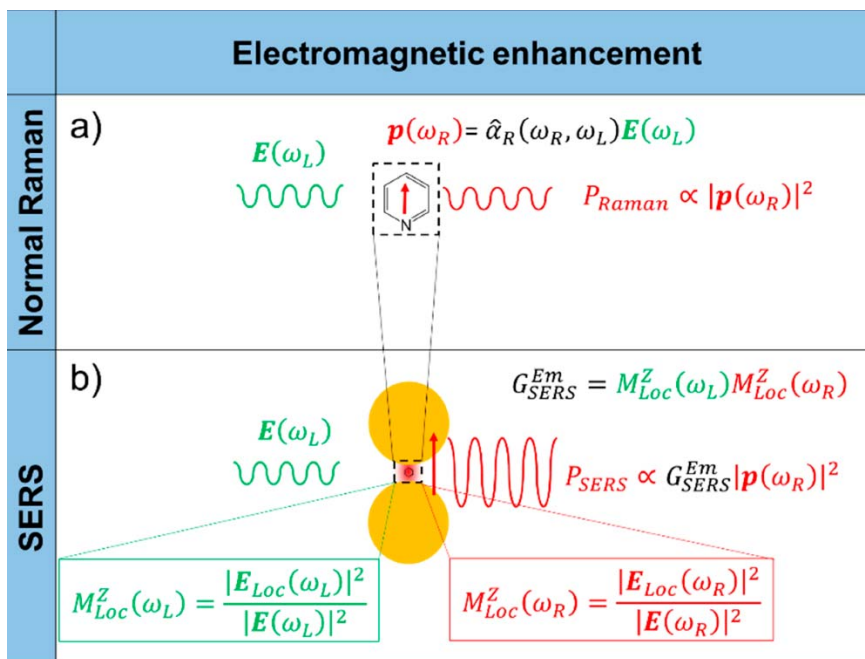


Fig. 1. 21 Electromagnetic enhancement models (a) normal RAMAN (b) SERS.

Adapted from [70]

### 1.6.3 SERS substrates

SERS was first performed on adsorbed analytes on the surfaces of coinage metals (Au-Ag-Cu) as well as alkali metals (Li, Na, K) with excitation wavelengths in the visible and near infrared range. There are other metals capable of performing SERS, but the metals mentioned above provide a stronger signal with a more satisfactory length of wavelength or wavenumbers. Metals such as Pd and Pt show a slight increase of wavelength in the near ultraviolet region. The nature and structure of the metal surface determines the resonant frequency of surface plasmon. Usually the visible and near infrared radiation region is used to excite the Plasmon Raman modes. Of course, silver was used before other metals due to its high surface plasmon effect.

SERS has been shown in metals such as platinum, ruthenium, palladium, iron-cobalt and nickel. These metals have shown an increase in Raman spectra by a factor of 1-3. The amount of enhancement compared to the enhancement obtained with Au and Ag is very low and this is due to problems in excitation of surface Plasmon resonance in the visible region, but nevertheless a large increase in order of magnitude can be achieved by transition metals using excitation wavelengths in the near ultraviolet region. Two examples of SERS active substrates that are rough and widely used are:

- 1- Metal colloids, especially agglomerated colloids, which are produced by chemical methods.
2. Electrode surfaces roughened by the electrochemical reduction-reduction cycle.

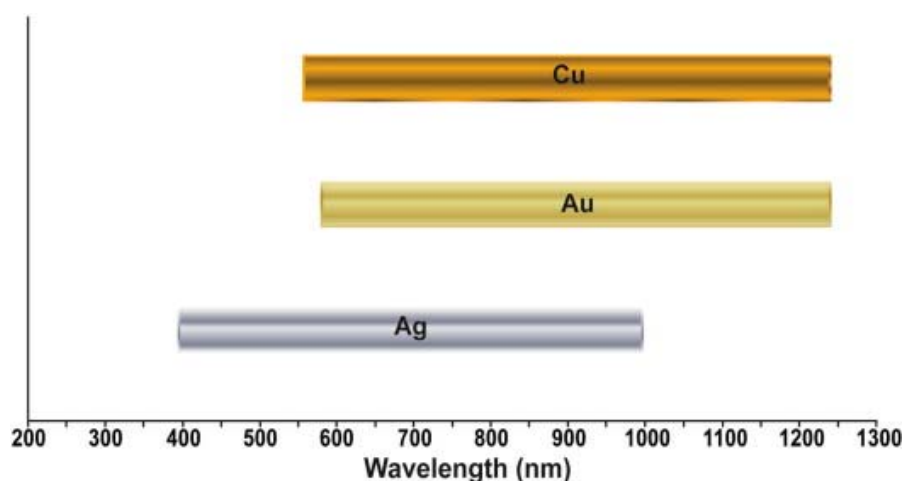


**Fig.1. 22** Wavelength ranges where Ag, Au, and Cu have been well-characterized and are established to support SERS [71].

Sharma et al. published statistics about Raman measurement of different molecules with Ag, Au and Cu used as substrate. They indicated strong and precise peaks of molecules in several range of wavelengths. These metals are used mostly as SERS substrate and their other advantage is their air-stability which makes them resistant against oxidation in the air. *Fig. 1. 22* [71].

#### **1.6.4 SERS in different media**

Several methods of working with the sample are used for surface enhanced Raman. In the most common technique, the Raman spectrum is usually obtained on the solid substrate which is made of a rough deposited metal surface. Samples

are exposed to the surfaces and, after deposition, they are irradiated with the laser source. In another method, metallic colloidal particles of silver or gold are suspended inside a dilute liquid sample (usually an aqueous solution) and then the solution is irradiated with the laser beam. Samples should be held or made to flow inside a thin glass tube to reduce laser refraction [72].

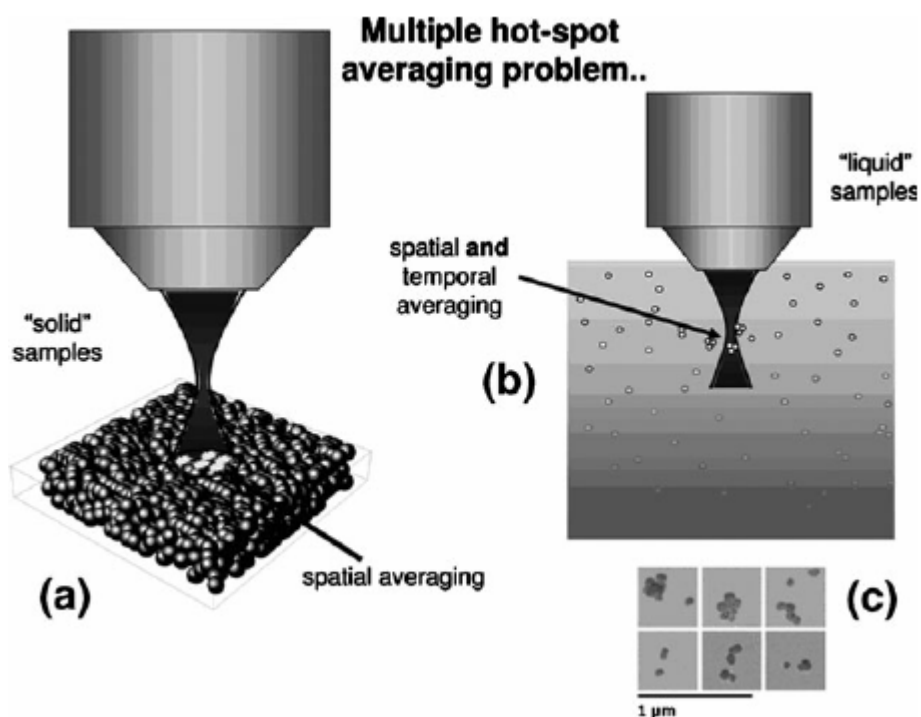


**Fig. 1. 23** Schematic comparison between SERS techniques a) solid substrate SERS b) Liquid substrate SERS c) particle dispersion in liquid adapted from [72]

The main problem with SERS spectroscopy in liquid is the homogeneity of spectra. Suspended particles in the solution are moving under the effect of Brownian motion and forming a non-homogeneous structure in the liquid. In reality, we have a disorganized dispersion of substrate particles *Fig. 1. 23 c)*. Due to the dispersion of particles in solution we obtain inhomogeneous SERS spectra. There is no evidence to know about the density of metal particles and how many molecules contributed to a given SERS signal *Fig 1.23 sec b) and c)*.

### **1.6.5 SERS Frequencies**

Interatomic bonds of chemical molecules and groups have different properties due to their type of bonding and electron orientation. SERS substrate indicated

plasmonic incitation upon encountering an electromagnetic field (sec 1.3), and cause a molecule to vibrate in many ways, and each way is called a vibrational mode.

Vibrational spectroscopy is based on periodic changes of dipole moments (IR) or polarizabilities (Raman) caused by molecular vibrations of molecules or groups of atoms and the combined discrete energy transitions and changes of frequencies during absorption (IR) or scattering (Raman) of electromagnetic radiation of wavelengths. Different organic bonds have specific vibrational spectra in unique wavelength of Raman and IR. This molecular spectroscopy yields bond-specific chemical specification of a specimen. This method is a reliable and precise method used in a variety of scientific fields such as organic/inorganic chemistry, geology, biomedical science, materials science, food science, and environmental science [73].

Several bonds and chemical functional groups can be identified from vibrational spectroscopy data. Some groups are listed in *Table. 1. 2*. Some bonds like C-C, C-O, and C-N are geometrically close to each other in molecules. These functional bonds are difficult to be identified as they have similar energy. Most of the time, these bonds seem to overlap. Measuring molecular vibration caused by SERS enablest researchers to analyze and discover the chemical formula of samples with relatively high accuracy [73, 74].

Functional group	Position (cm <sup>-1</sup> )	Remarks
>S-S<	500-550	
C-C	~1060-1127	Polyethylene
C-C	700-1260	Highly mixed in complex molecule
Aromatic ring	~1000	Monosubstituted
Aromatic ring	~1000	1,3 Disubstituted
Aromatic ring	~1000	1,3,5 Trisubstituted
Aromatic ring	~860	1,4 Disubstituted
CH <sub>3</sub> umbrella mode	~1375	
CH <sub>3</sub> and CH <sub>2</sub> deformation	1410-1465	

$>C=C<$	~1650	
$>C=C<$	~1623	Ethylene
$>C=O$ mixed with NH deformation	1620-1690	Amide I
$>C=O$	1710-1745	Changes for ketone, aldehyde and ester
$C\equiv O$	2100-2300	
SH	2540-2600	
$>CH_2$	2896 and 2954	Ethane
$>CH_2$	2845 and 2880	Polyethylene
$CH_3$	2870 and 2905	Polypropylene
$R_1R_2R_3CH$	2880-2890	Methine CH
CH	~2900	Cellulose
CH	~3015	Olefinic CH
CH	~3065	Aromatic CH
CH	3280-3340	Acetylenic CH
NH	3150-3340	Broadened and shifted by H-bonding
OH	3000-3600	Broadened and shifted by H-bonding

**Table 1.2** Raman frequencies of common chemical functional groups[73]

### **1.6.6 SERS substrate preparation**

One of the significant and basic needs to obtain appropriate and accurate results in the SERS technique is the use of a suitable substrate. Due to the effect of the distance between the substrate particles on the resonance of SERS peaks, the importance of this issue becomes clear. Several methods for substrate synthesis have been reported: 1- Chemical Vapor Deposition (CVD), 2- Nano Imprint Lithography (NIL), 3- Self Assembling methods.

LB is a type of self-assembling method which was explained above and we will discuss it with more detail in other chapters.

### 1.6.6.1 Chemical Vapor Deposition (CVD) method

Chemical Vapor Deposition (CVD) is a chemical process used to create a layer or deposit molecules or particles on a solid surface. The CVD method is one of the relatively advanced techniques. Soot formation due to incomplete oxidation of burning firewood is probably the oldest example of CVD deposition in prehistoric times. The industrial use of CVD dates back to de Lodyguine's 1893 paper where he deposited tungsten (W) on carbon lamp filaments by reducing  $WCl_6$  using  $H_2$ . During this period, the CVD process was developed as an industrially viable process in the field of extraction and pyro-metallurgy for the production of high purity refractory metals such as Ti, Ni, Zr and Ta.

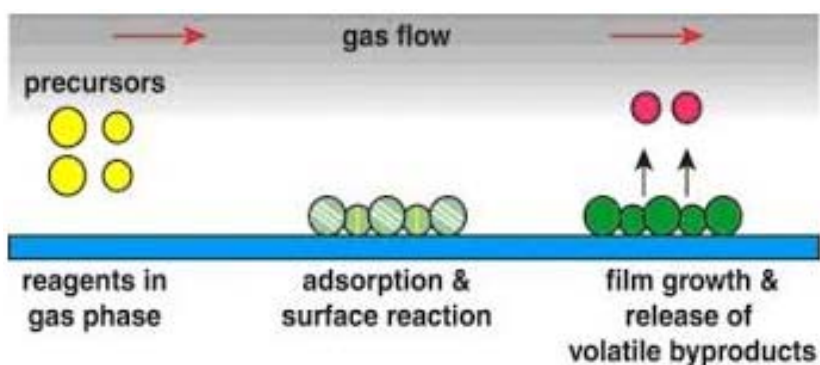


Fig 1.24 Schematic view of CVD process

CVD (Fig 1.24) is mainly used by the semiconductor component industry to form a thin film. In this method, the precursors evaporate and enter the reactor, where, the precursor molecules are adsorbed on the substrate. Usually, the temperature of the substrate is set in a certain range. The adsorbed molecules either decompose by heat or react with other gases and vapors to form a solid film on the substrate.

In CVD, the substrate is placed into a vacuum chamber, and two chemical precursors are heated, which causes them to vaporize. When they meet on the substrate surface, a chemical reaction occurs to form a high-performance thin film coating. The energy consumption in this method is very high as we need around 1000 degrees Celsius. Because of the presence of temperature gradients, it is difficult to control the shape and structure of the prepared particles or film. Also, the films created in this way may not have the desired homogeneity, unless different measures are implemented, such as: using the laser as a heat source, adjust the appropriate temperature gradient, prevent unwanted gas phase reactions, etc. A. Mohammadi et al and Litao Hu et al, in different studies used to

spray graphene based coatings to silver nanodendritic SERS substrates by means of CVD, to improve their surface enhance scattering [75, 76].

#### ***1.6.6.2 Nano Imprint Lithography (NIL) method***

Lithography is one of the most common methods for making electronic circuits. This method has been developed and has become more popular in recent years. With the pervasiveness of nanotechnology and the implementation of methods at nanometer scales by researchers, today it is possible to use this technique for producing structures with dimensions of 10 nanometers with high accuracy and quality. Lithography is a Greek word that consists of two parts, Lithos meaning stone and Graphia meaning writing and engraving. Therefore, the word-for-word translation of this word is engraved on stone. This method involves drawing a design of a pattern on materials and then transferring that design to other materials to produce an electronic or optical instrument. Preparation of sensors which consist of 2-D thin layers of metals and SERS substrate by lithography method been considered in recent years. [77, 78]. Liu et al fabricated a three-dimensional (3D) hot-spot network of nanopillars on plastic film by means of NIL [79].

Lithographic methods are divided into two general categories based on the required tools, image transfer method, and modelling strategy: (a) direct writing or engraving and (b) transfer of the design with an optical mask using conventional radiation methods. The first method is known as Serial Writing and the second method is known as Parallel Replication. Parallel replication methods include optical lithography, contact printing, and nano-seal lithography. These methods are used for high-efficiency, large-scale production, but cannot be used to customize designs [80-82]. Series engraving techniques such as scanning probe lithography are used to create custom patterns with high resolution and accurate recording. But the efficiency and speed of this method is low. Scanning Probe Lithography (SPL) is a method based on Scanning Probe Microscopy (SPM) and creates the desired design with various sub-methods such as mechanical scanning probe lithography (m-SPL), thermal scanning probe lithography (t-SPL) and thermochemical scanning probe lithography (tc-SPL). The dimensions of the final design created by this method are 10 to 100 nanometers. The SPL methods uses three probes: AFM [Atomic Force Microscopy], STM [Scanning Tunneling Microscopy] and SNOM [Scanning Nearfield Optical Microscopy] [83, 84].

### 1.6.6.2.1 Direct writing method of NIL

Direct writing is used to prepare a thin layer of metal on a solid surface by means of temperature and pressure. The procedure is performed in 3 basic steps (Fig 1. 25).

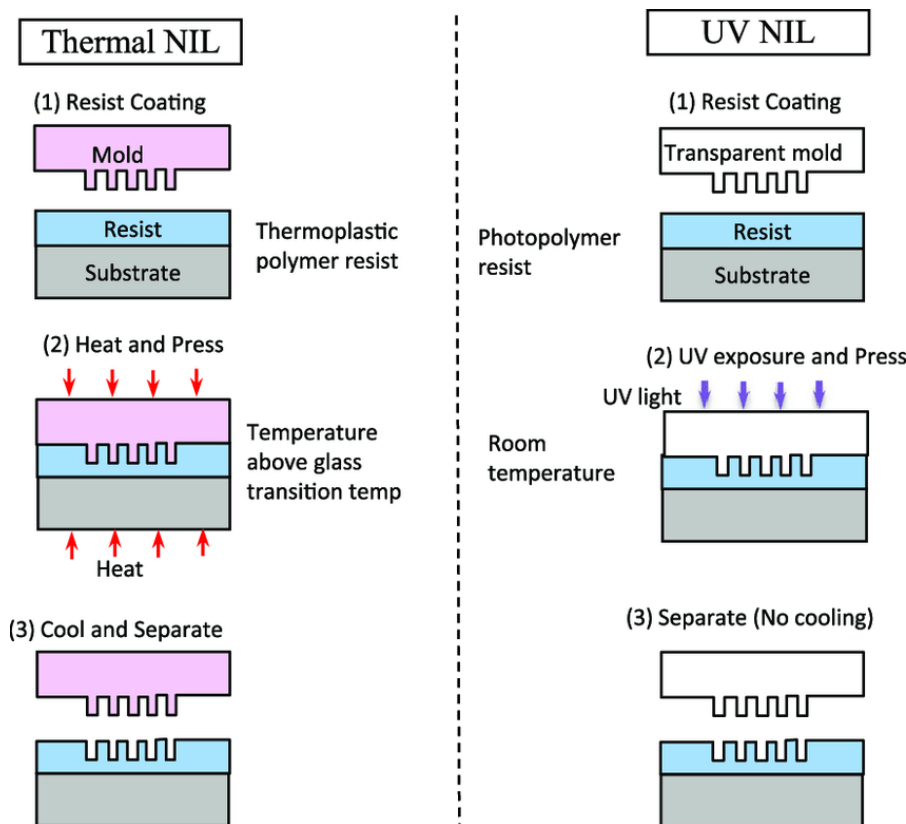


**Fig. 1. 25** Schematic comparison of a typical Thermal NIL (left) and UV-NIL (right) processes [85]

In step (1) the pattern and design are made with the desired nano-pattern, and this design is used to place on a substrate impregnated with a layer of polymer or coating, a step called resist coating. In step (2) heat and pressure is applied on the mold as the heated mold comes in contact with the resist, the resist will be heated up and softened into its molten stage, whereby it will fill in the mold cavities under sufficient imprinting pressure. In step (3), temperature and pressure is cut off and the setup cools down, and then the mold is separated from the polymer (*Fig 1.25*). The direct NIL method can be used to produce SERS substrates, many of which

consist of neat arrays of metal dots. This method could be used to prepare different metal patterns, such as gold, silver and platinum-copper, which are widely used for SERS measurements [86].

After the preparation of pillars made on polymer by the NIL method, we could deposit metal particles on them to prepare a SERS substrate. Barcelo et al, fabricated SERS substrates by evaporating gold on top of Si pillars. In the first step, a high-aspect-ratio pillar arrangement is defined in Si and subsequently transferred into a flexible polymer material by nanoimprint lithography. Then an array of gold nanoparticles is prepared on their tips [87].

#### **1.6.6.2.2 Optical Lithography**

Optical lithography is the oldest method for creating a design on solid surfaces. Ultraviolet and extreme ultraviolet lithography are widely used in the semiconductor industries to print electronic chips. The difference between ultraviolet and extreme ultraviolet lithography is related to the range of ultraviolet wavelengths. As of 2020, Samsung and TSMC are the only companies who have used ultraviolet lithography to fabricate chips and micro-electronic devices. In this process, the semiconductor surface (silicon wafer) is first coated with a thin layer of a light-sensitive polymer or resist called photo-resist. The coated layer is subjected to heat curing to remove the remaining solvent completely and it is prepared for the design. To create the design, an ultraviolet beam with a wavelength of 193-436 nm passes through an optical mask. The optical mask is usually made of quartz or glass and consist of two parts 1. Transparent part 2. Opaque part. Opaque materials were used to avoid UV radiation from desired parts of the mask. Parts of the substrate that have been exposed to ultraviolet radiation undergo reactions and the desired material will deposited onto it. There are two main protocols after exposure the substrate to UV light. In one protocol the photoresist is washed with suitable chemicals and in the other protocol the exposed photoresist is preserved. (Fig. 1.26) [88].

The protocol of high-energy ultraviolet and X-ray lithography techniques are the same as optical lithography, but in these methods, due to the high energy of the used beams, it is necessary to use resistant photoresist and substrate with special capabilities and special optics. It is worth noting that using these latter methods, one can create patterns with an accuracy below 100 nm.

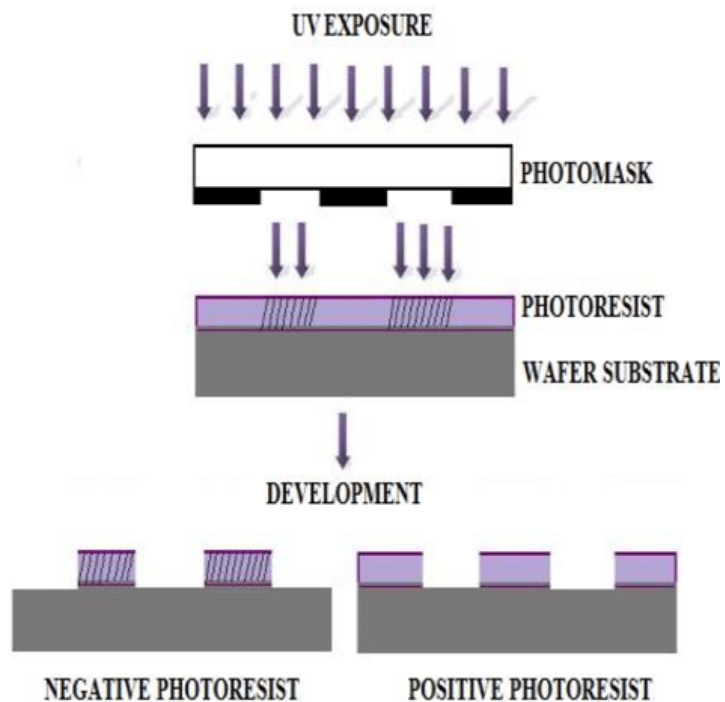


**Fig. 1.26** Schematic of UV exposure in lithography method and difference between positive and negative photoresist adapted from [88]

The protocol of high-energy ultraviolet and X-ray lithography techniques are the same as optical lithography, but in these methods, due to the high energy of the used beams, it is necessary to use resistant photoresist and substrate with special capabilities and special optics. It is worth noting that using these latter methods, one can create patterns with an accuracy below 100 nm.

### ***1.6.6.3 SERS substrate preparation by self-assembly method***

In comparison to the complex chemical and physical methods which are described above, self-assembly is a relatively simple and cost-effective method that could be used to prepare a SERS substrate. Self-assembly of nanostructures is a process where atoms, molecules, polymers, colloids, nanoscale building blocks or even macroscopic particles spontaneously organize into ordered structures or patterns with nanometer features without any external intervention. For nanoparticles, this spontaneous assembly is a result of the interaction between the particles aimed at reaching thermodynamic equilibrium and reducing the system's free energy.

Self-assembling is recognized in two forms, namely, static and dynamic. Static self-assembly utilizes interactions amongst the nanoparticles to achieve a free-energy minimum. A dynamic system is forced not to reach equilibrium by supplying the system with a continuous, external source of energy to balance attractive and repulsive forces. Static self-assembly is significantly slower compared to dynamic self-assembly as it depends on the random chemical interactions between particles [89].

C. Fang et al demonstrated a method to prepare silver (Ag) nanoparticle assembly as a SERS substrate by immersing a flat silicon wafer into an aqueous solution of hydrogen fluoride (HF) with silver nitrate, and finally a monolayer of Ag particles was uniformly deposited on the silicon substrate [90].

Jiandong Hu et al deposited gold films onto (3-aminopropyl)-trimethoxysilane (APTMS)-coated glass surfaces by means of self-assembly. APTMS was used as an adhesive reagent to attach the gold nanoparticles (AuNPs) onto the glass substrate. They immersed APTMS-coated glass into a colloidal gold solution for 6h to form the self-assembled monolayer (SAM) of the AuNPs [91].

## ***1.7 Objectives of research***

In this work we follow two main objectives. Firstly, we want to utilize the LB technique to fabricate SERS substrates with gold nanoparticles. We can identify substances present in a sample from their unique Raman spectral fingerprints, typically using databases of known spectra.

At first, we focus on performing SERS measurements of 4-MBA, as a reference organic molecule. We want to tune multiple parameters that are involved in the quality of SERS substrates, such as surface pressure during the preparation of monolayers by means of the LB technique, electroless plating time of gold nanoparticles, and nanoparticle core size and shape.

The second objective of this work is to improve our fabricated substrates to measure and determine water and wastewater pollutant molecules. Thiram and Carbaryl are selected as organic pollutants in the next phase of our study and we will test our substrates to detect them with the SERS technique. We plan to fabricate SERS substrates which can be used as sensors to detect several compounds. Our main goal is to prepare solid SERS substrate to introduce it as a base of a low-cost, high efficiency sensor.. Our LB proposed method for preparing SERS substrates could be used to fabricate sensors that could be used directly in aquatic environments and adsorb several pollutants and other organic molecules. We plan to perform a SERS technique as a time saving, reliable and precise method to use for initial identification of contaminant in aqueous environment

## ***2. Materials and methods***

## 2.1 Preface

In this chapter, I will describe the methods and materials which we used in this research. First, I will talk about preparing a Langmuir film of gold nanoparticles at the interface of water/air. Then, I will describe solid substrate modification and the transferring of a gold monolayer onto it. The next step will be analyzing and characterizing the substrates by *UV/VIS* spectroscopy. Afterwards, the analyzed molecule was deposited on the surface and we completed SERS measurements. Next, I used gold nanoparticles with different size and shape to compare their effect on *SERS* spectra of the target molecule. At the final part of this study, synthesized substrates were used to measure the SERS spectra of water pollutants (Carbaryl and Thiram) and their isotherm of adsorption on the substrate.

## 2.2 Materials

Spherical gold nanoparticles of different diameters (5, 10, 20, 30 and 40 nm) and gold nanostars of approximate diameter 40 nm, were used in this study. Spherical gold nanoparticles were purchased from Sigma–Aldrich as aqueous suspensions stabilized with citrate as a capping agent. Poly (ethylene glycol) methyl ether thiol (PEG) (6000 g/mol), 1-dodecanethiol (1-DDT, 98%), 4-mercaptobenzoic acid (4-MBA, 99%), Hydrogen peroxide (30%), Hexane (98.5%), Methanol, (3-aminopropyl) triethoxysilane (APTES, 99%), Gold (III) chloride trihydrate ( $\text{HAuCl}_4 \cdot 3\text{H}_2\text{O}$ , 99.99%), Silver nitrate ( $\text{AgNO}_3$ ,  $\geq 99\%$ ), Sodium citrate tribasic dihydrate ( $\geq 98\%$ ), Hexadecyltrimethylammonium bromide (CTAB,  $\geq 99\%$ ), L-ascorbic acid (AA,  $\geq 99\%$ ), Tetramethylthiuram disulfide (Thiram 97%) and 1-Naphthyl-N-methylcarbamate (Carbaryl) were purchased from Sigma–Aldrich. Ethanol 96%, sulfuric acid (95%), and hydrochloric acid (37% v/v) were purchased from Panreac (Barcelona, Spain). Reagent grade toluene was purchased from Scharlau (Barcelona, Spain). All chemicals were used as received. We used float glass slides from *DURAN* Co. for *UV/VIS* and *SEM* imaging. As SERS substrates, we used polished 7980 fused-silica slides from 2SPI (*West Chester, PA, USA*), and cut them with a size of 15×10 mm. Milli-Q water was used in all processes in this research.

Chemical compound	Abbreviation	Formula	Structure
Poly (ethylene glycol) methyl ether thiol	PEG	$\text{CH}_3\text{O}(\text{CH}_2\text{CH}_2\text{O})_n\text{CH}_2\text{CH}_2\text{SH}$	
1-Dodecanthiol	1- DDT	$\text{CH}_3(\text{CH}_2)_{11}\text{SH}$	
4-Mercaptobenzoic acid	4-MBA	$\text{HSC}_6\text{H}_4\text{CO}_2\text{H}$	
Hydrogen peroxide	–	$\text{H}_2\text{O}_2$	
Hexane	–	$\text{C}_6\text{H}_{14}$	
(3-aminopropyl) triethoxysilane	APTES	$\text{C}_9\text{H}_{23}\text{NO}_3\text{Si}$	
Hexadecyltrimethyl ammonium bromide	CTAB	$\text{C}_{19}\text{H}_{42}\text{BrN}$	
Silver nitrate	–	$\text{AgNO}_3$	
L-Ascorbic acid	AA	$\text{C}_6\text{H}_8\text{O}_6$ or $\text{HC}_6\text{H}_7\text{O}_6$	
Tetramethylthiuram disulfide	Thiram	$\text{C}_6\text{H}_{12}\text{N}_2\text{S}_4$	
1-Naphthyl-N-methylcarbamate	Carbaryl	$\text{C}_{12}\text{H}_{11}\text{NO}_2$	

**Table 2. 1** Brief description of used chemicals

## 2.3 Instruments

All monolayers in this study were prepared at the interface of air/water in a KSV NIMA mini-trough system. Monolayers at the air/water interface could be easily transferred to the solid substrate by the dipping system in the Langmuir film balance. It is also possible to prepare films using the Langmuir-Schafer technique for transferring monolayers. Using the included Wilhelmy plate method we monitored the surface pressure at the interface during monolayer preparation (see

sec 1.4.6 to 1.4.8). We used a custom-made Brewster angle microscope (BAM) system, in order to monitor the state of the monolayer during experiments.

A Shimadzu *UV-1700* spectrophotometer was used to characterize gold NP-coated glass. The spectrophotometer was equipped with a custom 3D-printed holder to hold and support LB-coated plates. Localized Surface Plasmon Resonance (LSPR) of the gold monolayers on glass were characterized with UV-vis spectroscopy (*Fig. 2.1*).

We use Scanning electron microscopy (SEM) with a Jeol J-7100F Field Emission Scanning Electron Microscope to visualize the morphology of gold NP monolayers. Transition electron microscope (TEM) JEOL JEM 2010F 200 kV, Japan was used in our research.



**Fig. 2.1** a) KSV NIMA LB mini-trough b) Shimadzu UV-1700 uv-vis spectrometer c) Jeol J-7100F Scanning Electron Microscope d) Jobin-Yvon Labram HR 800 Raman spectrometer. Images adapted from manufacturers

All of SERS Spectra were obtained using a dispersive spectrometer Jobin-Yvon Labram HR 800 (Kyoto, Japan) which was coupled to an Olympus BXFM optical microscope (Barcelona, Spain). We used a 16-bit dynamic range Peltier cooled CCD for image acquisition. In all measurement of 4-MBA we

irradiated with a 532 nm laser and, for analyzing pollutants, we used a 785 nm laser. The laser power irradiated on the samples was in the range 0.5-4 mW, using a diffraction grating of 600 lines  $\text{mm}^{-1}$  with 50 $\times$  and 100 $\times$  microscope objectives. Diffraction gratings are optical devices that are used in instruments such as spectrometers to separate polychromatic light into the underlying constituent wavelengths of which it is comprised.

## **2.4 Software**

For processing the SERS spectra we used the software Labspec (version 5, Horiba Ltd., Kyoto, Japan) and IgorPro (version 7 and 8, Wavemetrics, Inc., Tigard, OR, USA). All spectra have been normalized by the laser power. We applied a band-pass filter at the 2 main peaks of 4-MBA in order to enhance the signals. For Thiram, we applied a band-pass filter at the 1386 and 1515  $\text{cm}^{-1}$  peaks and for Carbaryl we did it for peaks at the 1374 and 1576  $\text{cm}^{-1}$ .

## **2.5 Methods**

### **2.5.1 Gold nano-star preparation**

Unlike gold nanospheres (5-40 nm), which we used as received in aqueous suspensions, gold nano-stars (or urchin-shaped) NPs were synthesized in our laboratory adapting the protocols described by Serrano et al. [36]. In brief, we mixed 500  $\mu\text{L}$  of 10 nm gold NP suspension, 10 mL of 0.25 mM  $\text{HAuCl}_4$  and 10 mL of 1.0 M HCl in a 20 mL glass vial, under moderate stirring and quickly we added 100  $\mu\text{L}$  of  $\text{AgNO}_3$  (3 mM) and 50  $\mu\text{L}$  of ascorbic acid (100 mM) to the solution, and immediately the color changed (from yellow to dark red or purple) indicating a change in the particles size and shape. The final size of nanostars was verified by TEM. The average diameter was 50 nm. The processes above were performed at room temperature, and the final aqueous nanostar suspension was kept in the refrigerator at 4 $^\circ\text{C}$  up to several months.

### **2.5.2 Nanoparticle functionalization and phase transfer**

Spherical gold nanoparticles were purchased in the form of aqueous suspensions. In order to prepare a monolayer at the interface of water/air it is necessary to disperse the gold nanoparticles in chloroform as a volatile organic solvent. These nanoparticle dispersions appeared to be indefinitely stable at room temperature.

Chloroform, toluene and hexane are used as solvents to prepare gold nanoparticle colloidal suspensions. There are different methods for phase transferring aqueous gold particles into an organic solvent. Most of the reported phase transfer methods have restrictions on the size of the particles, and cannot be used for particles smaller than 100 nm [92]. To perform a complete phase transfer and to avoid aggregation of particles in the chloroform suspension, we adapted a method used by *Serrano-Montes et al.* which is simple, rapid and trustable, based on particle functionalization with a combination of 1-DDT and PEG-SH [36]. In brief, we add different amounts of water-soluble PEG-SH and chloroform-soluble DDT respectively to the aqueous particle suspension and to chloroform (see Table (2.2)). The concentration of particles in suspension is considered to be the one reported by the manufacturer, and we have used it to calculate the nominal particle surface in our samples. Different amounts of PEG-SH was added to the aqueous particle dispersion, as detailed in Table 2. 2, to achieve a desired concentration of PEG-SH molecules per nm<sup>2</sup> of particle surface. The aqueous solution was put into contact, inside of a test tube, with a DDT chloroform solution. Vortex shaking at 1500 rpm leads to the particle exchange across the water/chloroform interface. We add 30 µL of concentrated HCl to 10 mL of nanoparticle suspension to accelerate the process during phase transfer. After using centrifugation with the conditions described in Table. 2. 2, the supernatant aqueous solution was removed and exchanged with fresh Milli-Q water and shaking was performed again for 30 min. This process was performed 3 times to ensure that all non-adsorbed PEG-SH was eliminated from the suspension. The rinsing step could be done up to 5 times as mentioned by *serrano* [36]. After rinsing the suspension with Milli-Q water for several times, we obtain a chloroform suspension of nanoparticles functionalized with a combination of PEG-SH and 1-DDT. The resulting suspension obtained following this protocol has the same concentration of NP in chloroform as in the original aqueous suspension.

Moreover, gold NP have become hydrophobic and can be spread directly over the interface of water/air. Suspension of particles could be sealed and kept in a refrigerator. To correct for solvent evaporation, we marked the top surface of the suspension in the vial prior to storing, and it was checked before using, adding chloroform in case of evaporation.



**Fig 2.2** surface structure of functionalized gold with PEG-SH and 1-DDT

Schematic view of gold NP with functionalized surface is indicated in *Fig. 2.2*. There is a hybrid layer of hydrophobic 1-DDT and hydrophilic PEG-SH that surrounds the gold particles. High density of capping agents makes particles more stable in organic solvents and prevents aggregation. The surface of gold nanoparticles covered with PEG and 1-DDT could be oxidized easily with O<sub>2</sub> plasma in order to prepare it for other part of the experiments and attach other organic molecules to the NP.

Size (nm)	PEG-SH molecules per nm <sup>2</sup>	molecules of DDT per nm <sup>2</sup>	centrifugation for phase transfer
5	0.85	140	3900g; 30 min; 20 °C
10	0.8	148	3900g; 30 min; 20 °C
20	0.7	150	2500g; 15 min; 20 °C
30	0.6	150	2500g; 15 min; 20 °C
40	0.6	155	2000g; 15 min; 20 °C
Nanostar	1.4	155	1500g; 25 min; 10 °C

Table 2.2 Gold nanoparticle phase transfer conditions

### **2.5.3 Gold NP Langmuir monolayer preparation**

Gold NP monolayers were prepared by dropwise addition of chloroform NP suspension at the water/air interface (nominal pH = 5.7, in equilibrium with atmospheric CO<sub>2</sub>). A few drops of the suspension are spread at the water surface using a Hamilton syringe in a Langmuir film balance (KSV mini-trough system). In situ-monitoring of the surface pressure was performed by means of a paper Wilhelmy plate (sec 1.4.7). Morphology of the monolayer at the interface was monitored by a custom-made BAM. There is a potential for monolayer collapse by overlapping NP layers at high lateral pressures, which we want to prevent. To avoid those problems, we need to monitor the surface pressure in real time. After solvent evaporation, gold nanoparticles remain at the water/air interface thanks to the hydrophobic capping effect 1-DDT. By adjusting the barriers of the LB trough, the surface area and the surface pressure are controlled and monolayers with different densities are obtained. Compression of the monolayer was controlled with the KSV NIMA LB control software. We waited around 15 min for solvent evaporation after monolayer preparation. All protocols and experiments were performed at room temperature.

### **2.5.4 Substrate Preparation**

We used APTES for silanizing glass and fused-silica slides. The hydroxyl groups of mineral components like glass and metal oxide surfaces can be easily displaced by the alkoxy group of silane, leading to the formation of a covalent -Si-O-Si bond. Silanization is performed to increase the hydrophilicity of glass surfaces [93]. APTES molecules contain a terminal amine (NH<sub>2</sub>) whose properties are extensively used for surface functionalization. These amine groups have affinity to gold nanoparticles and are widely used to immobilize the nanoparticles through electrostatic interactions [94, 95]. First, all glass instruments were cleaned with sulfuric acid overnight. All glass and fused silica slides were first cleaned with ethanol and acetone, rinsed with Milli-Q water, and dried under stream of N<sub>2</sub>. In the next step, to ensure their surface is free of impurities, we immersed all slides of glass and fused silica into piranha solution (7:3 v/v solution of H<sub>2</sub>SO<sub>4</sub> and H<sub>2</sub>O<sub>2</sub>) for 30 min, and subsequently rinsed with Milli-Q water, and finally dried under a stream of N<sub>2</sub> gas. Glass substrates were immersed in a solution of APTES in 10 % toluene v/v and incubated 120 minutes at a temperature of 60 degrees in a bain-marie containing mineral oil.

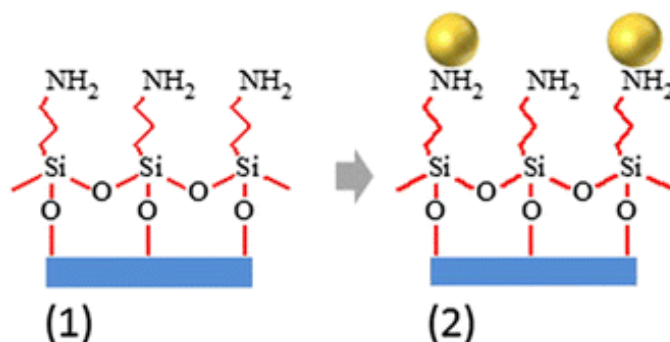


**Fig 2. 3** (1)Surface of glass and silica after functionalization with APTES, (2) Gold particle attaching to functionalized glass and silica surface adapted from [95]

It is crucial to seal the APTES solution during functionalization because contact with water should be avoided, since the reactivity of APTES with water and moisture is very high and leads to sedimentation in solution. After functionalization, we rinsed the glass plates with methanol, toluene, and finally we dried them with nitrogen and we kept them under vacuum. Although the stability of APTES coated glass is high under vacuum, we used them for monolayer transfer during the same day.

### ***2.5.5 Monolayer transfer onto a solid substrate***

Gold NP monolayers were prepared at the interface of water/air at different surface pressures (*sec. 2.5.3*), and subsequently transferred to the glass or silica plates using the Langmuir-Blodgett method (*Fig. 2.4*). Substrates were extracted from water at the constant speed of  $0.1 \text{ mm s}^{-1}$  using the dip-coating mechanism of the KSV minitrough. The control software features a feedback mechanism that allows to keep the pressure constant and compensate particle loss during plate extraction. After the extraction, the resulting gold NP films were cleaned under O<sub>2</sub> plasma to remove traces of organic compounds. These substrates can be stored in a vacuum for a long time after preparation. All silica and glass slides could be reused several times after cleaning their surface with *aqua regia* to remove the deposited gold layer. Aqua regia is a mixture of nitric acid and hydrochloric acid, optimally in a molar ratio of 1:3 (HNO<sub>3</sub>+3 HCl), that can dissolve the noble metals such as gold and platinum

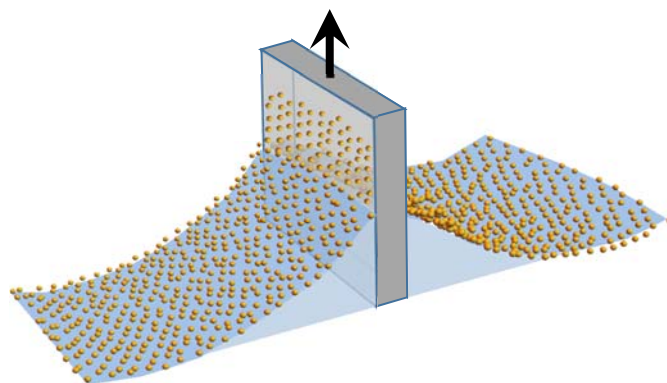


**Fig. 2. 4** Schematic of the LB transfer of a gold NP monolayer from the water/air interface to the solid substrate

### ***2.5.6 Vis–NIR spectroscopy***

We used Shimadzu UV-1700 spectrophotometer (sec. 2.3) to characterize the effect of gold nanoparticles LSPR. Gold films prepared at different lateral pressure were analyzed to study the effect of particle density on Plasmon resonance. Spectra were collected from 400 to 800 nm with a resolution of 0.5 nm.

### ***2.5.7 Scanning electron microscopy***

A Jeol J-7100F Field Emission Scanning Electron Microscope was used in this research. We assessed the quality of the obtained monolayer by SEM imaging. Samples were prepared for SEM by attaching them on a small metal holder using double sided tape and then they were coated with an evaporated carbon layer to increase conductivity.

### ***2.5.8 Electroless deposition of gold***

After cleaning gold coated glass substrates with  $O_2$  plasma we used an electroless plating method to enhance the Raman signal. With this electroplating technique we modified the size and shape of gold nanoparticle seeds. To this purpose, NP-coated plates were soaked in a 10 ml solution of 0.01% (w/v)  $H AuCl_4$  and we added 500  $\mu L$  of  $H_2O_2$  to reduce gold chloride ions to gold atoms. This process is performed under vigorous agitation at room temperature for 2-15 min. After 2 min, the color of the glass surface slowly turned to pink, which indicates the increase of

seed size due to the deposition of gold atoms. All resulting substrates were cleaned with O<sub>2</sub> plasma for the second time to ensure the removal of organic impurities from the surface.

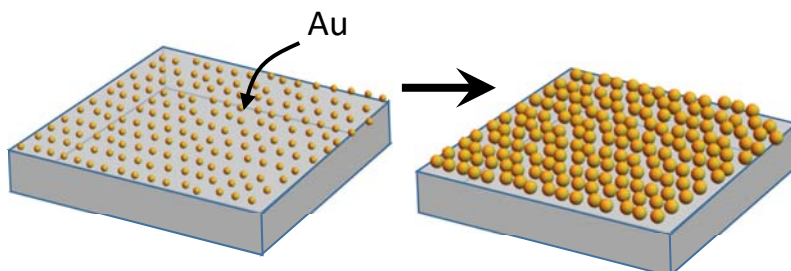


**Fig 2. 5** The size of the nanoparticles is increased by means of electroless gold deposition

### ***2.5.9 Solid substrate functionalization with 1-DDT***

1-DDT was used during the phase transfer of gold nanoparticles from aqueous suspension to chloroform suspension. 1-DDT increased the hydrophobicity of the surface of gold particles and prevented particle aggregation during phase transfer [36, 96]. 1-DDT molecules were used as capping agent in this study where gold nanoparticles can be influenced by the nature of the capping agent. Extraordinary stability of gold nanoparticles is attributed to 1-dodecanthiol that form a strong covalent bond with the particle surface improving their hydrophobicity and, moreover, cover the surface with long hydrocarbon chains with free –CH<sub>3</sub> heads. This spatial form allows particles to be further functionalized and attached to other molecules or particles [97, 98].

Gold surfaces could form strong and stable bonds (Au-S, ~50 Kcal mol<sup>-1</sup>) with thiols (-SH). Their alkyl chains with free CH<sub>3</sub> head groups act like an anchor and adopt an intertwined structure that could capture molecules, such as the water pollutants. For this purpose, we immersed glass substrate cover with gold NP overnight in a 10 μM solution of 1-DDT in chloroform to ensure saturation of the gold surface by 1-DDT.

## **2.5.10 Surface Enhanced Raman Scattering (SERS)**

### **2.5.10.1 4-MBA incubation**

4-MBA was used in our research for the presence of well-known reference and distinctive SERS peaks ( $1076\text{ cm}^{-1}$  and  $1055\text{ cm}^{-1}$ )[36, 99, 100]. Prior to incubation of 4-MBA, substrates have to be cleaned with  $\text{O}_2$  plasma. We cleaned all substrates with plasma except for those which were functionalized with 1-DDT as we need to keep thiol ligands on the substrate as mentioned in sec 2. 5. 9. For depositing

4-MBA molecules on the surface of SERS substrate, we used  $300\ \mu\text{L}$  of a  $10\ \mu\text{M}$  4-MBA aqueous solution (prepared from  $1\ \text{mM}$  stock solution in ethanol), and it was incubated, at room temperature, on top of the gold substrate. Self-assembled monolayers of 4-MBA on gold were formed during the 30 min incubation time. Immediately afterwards, we washed the substrates with Milli-Q water, and dried them under a nitrogen stream. SERS Spectroscopy of the samples were performed within 1 hour of preparation. We also tested the stability of the gold monolayer and found no significant variation in the SERS signals in a week after 4-MBA incubation at room temperature.

### **2.5.10.2 Thiram incubation**

Aqueous solutions of  $1$  and  $5\ \mu\text{M}$  of Thiram in water were prepared and used as stock solutions in this study. Other concentrations were obtained by diluting the stock solution with water.  $100\ \mu\text{L}$  of Thiram solution with concentration from  $10\ \mu\text{M}$  to  $50\ \text{nM}$  was incubated on the surface of SERS substrates, which were prepared under different conditions of lateral pressure and contained different types of gold particles. We further used 1-DDT functionalization to improve the SERS spectrum quality for pollutant detection. After  $\approx 30$  min of incubation at room temperature and solvent evaporation, solid glass substrates were used for SERS measurement.

### **2.5.10.3 Carbaryl incubation**

Carbaryl has a low solubility in water ( $\approx 0.01\%$  at  $20^\circ\text{C}$ ) and vigorous vortex agitation and an ultrasonic bath is needed to achieve the desired level of concentration. We prepared a stock solution of  $10\ \mu\text{M}$  in water by using high vortex agitation and ultra-sonication. Lower concentrations were prepared by diluting the

10  $\mu\text{M}$  stock solution. Higher concentrations of Carbaryl can be obtained in ethanol instead of water. 100  $\mu\text{L}$  of Carbaryl solution was incubated on the SERS substrate until the complete evaporation of water  $\approx 30$  min. SERS measurement were performed within an hour after sample preparation.

***3. SERS substrate preparation by  
LB technique and SERS  
measurement of 4-MBA***

### **3.1 Preface**

In this chapter, we demonstrate a pathway for the fabrication of tailorable quasi-two-dimensional lattices of gold nanoparticles to be used in Surface Enhanced Raman Scattering (SERS) detection of biomolecules. The first part of my work is related to prepare SERS substrates by means of the Langmuir-Blodgett method. We prepared monolayers of gold nanoparticles at the interface of air/water and transferred them to solid surfaces such as glass and silica. The prepared SERS substrates were characterized with UV-NIR spectroscopy and scanning electron microscopy. After characterization and electroplating the substrates with gold, they were exposed to a 4-MBA solution and, upon solvent evaporation, SERS measurement were performed.

### **3.2 introduction**

The development of nanostructured materials based on the self-assembly of simple constituents mediated by wet chemistry methods has been demonstrated to be an efficient and scalable bottom-up strategy [101-104]. We used a versatile approach using spherical nanoparticles as building blocks of 2D or 3D lattices. We prepared mono-disperse hotspots using gold nanospheres as spheres have shown the inherent tendency to self-assemble into ordered 2D or 3D lattices [105].

The Langmuir-Blodgett (LB) deposition method is used to control the self-assembly of nanoparticles. Although this method was originally developed for the transfer of insoluble surfactants previously organized at the water/air interface, it can also be used for the deposition of supramolecular entities [106] and hard nanomaterials [107]. A hydrophilic substrate that can be in a wide size range is initially submerged in the water sub phase. After spreading the nanoparticles and upon evaporation of the solvent we adjusted the monolayer to the desired packing density by moving the barriers of the LB trough. The substrate is smoothly pulled through the interface, thus peeling a thin film of water that carries the monolayer with it. After water evaporation and film drainage, the spread monolayer is deposited while preserving the original lateral order. The thin films prepared in this research with the LB technique could be employed for the preparation of photonic materials or as templates to improve the tribological properties of substrates [108, 109]. Noble metal

nanoparticles are widely used in bio sensing thanks to their plasmon resonance that enhances scattered signals of adsorbed biomolecules [110, 111]. We tried to leverage the plasmonic effects to increase the intensity of SERS spectra.

Preparation of reliable and easy to fabricate SERS substrates are main aspects in our study. Forming self-assembled monolayers (SAM) of gold or silver nanoparticles in contact with a substrate that has been chemically modified to provide suitable binding sites is a simple protocol for SERS substrate preparation [112] [113]. There are some control parameters in this method such as material, size, and shape of the nanoparticles. The main restriction of this method is the surface coverage. Although the surface coverage obtainable by this technique is limited and in very few cases can reach 50% of the substrate area by functionalizing particles with organic molecules and ligands, we can obtain homogeneous hotspot distributions. Proposed methods could involve pre- or post-processing of the nanoparticle monolayer. For instance, nanoparticles can be embedded in a thermosensitive film that allows to tune their spacing [114, 115]. LB deposits can be employed as templates or masks using subsequent lithography techniques in order to manufacture SERS substrates. However, a simple general protocol where the LB films of nanoparticles are directly tuned to optimize their performance as SERS substrates had not been demonstrated before.

Surface chemistry of gold nanoparticles is an important aspect in the demonstrated protocol, which must enable their dispersion in a volatile hydrophobic solvent. Avoiding nanoparticles aggregation that would result in a heterogeneous SERS detection is a key step in our work [116].

### **3.3 methods**

In the first stage, to move from the idea of this research into action, we used the Langmuir trough to create a gold nanoparticles monolayer at the interface of water/air. Upon preparing monolayers at different surface pressures, we transferred them to the desired substrate (glass and fused-silica) using the Langmuir-Blodgett method (sec 2.5.3 to 2.5.5).

After preparing the SERS substrate, in the second step, *Uv-Vis* and *SEM* techniques were utilized to verify the formation of a monolayer on the solid surface. We subsequently used electroless deposition of gold in order to enhance the SERS signal. Gold nanoparticles on the surface were used as seeds for the electroless deposition (sec 2.5.8).

SERS substrates were cleaned under O<sub>2</sub> plasma to remove traces of organic compounds and were incubated in a 4-MBA aqueous solution. 4-MBA was incubated on top of the gold substrate for 30 min, washed with Milli-Q water, and dried under a stream of nitrogen. SERS spectra were obtained within 1 h of 4-MBA monolayer formation. The stability of the films was tested 24 h after 4-MBA incubation at room temperature and no significant variation were detected (sec 2.5.10.1). We used the Raman Dispersive Spectrometer Jobin-Yvon Labram HR 800 (*for detailed information see chapter 2*).

## **3.4 results**

### **3.4.1 Langmuir monolayers of nanoparticles**

The chloroform suspension of functionalized particles, with a nominal concentration of  $5.47 \times 10^{13}$  particles/ $\mu\text{L}$ , was spread dropwise over the water/air interface using a 50  $\mu\text{L}$  Hamilton glass syringe. We used Milli-Q water in equilibrium with atmospheric CO<sub>2</sub> as sub-phase. The nominal pH was about 5.7. We tried to avoid irreversible formation of 3D clusters of nanoparticles by maintaining the initial particle surface concentration low. The particle self-assembling was monitored by real time BAM imaging system. The reflectivity from the thin film under BAM observation is a function of the square of its thickness [117], and the formation of thicker patches upon monolayer collapse, during film compression could be easily detected. Gold particles are affected by capillarity-mediated interparticle interactions. This interaction result in a direct coupling between lateral packing density and surface pressure (surface tension reduction). By monitoring and adjusting the surface pressure we could control the state of the gold monolayer at the interface of water/air (*Fig. 3.1*).

The rise of surface pressure begins at surface densities of particles as low as 50-100 particles/ $\mu\text{m}^2$ , which corresponds to an average center-to-center particle distance of around 100 nm. Collapse of monolayer happens at around 15 mN m<sup>-1</sup>. Once the monolayer is prepared at the desired lateral pressure, LB transfer is performed at a constant pressure by the dipping mechanism in the film balance equipment. The hydrophilic functionalized substrate (glass or fused silica) had been submerged in the sub phase before particle spreading (*Fig 2.4*).

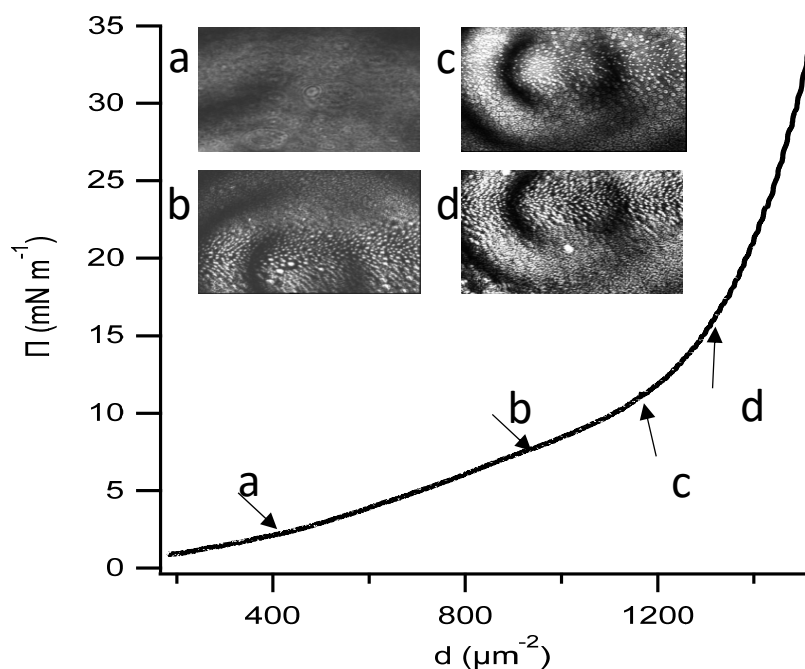


**Fig 3. 1** Surface pressure vs. particle surface number density isotherm. Brewster angle microscopy micrographs (field of view is 0.9 mm wide) have been captured under different compression conditions, as indicated by the corresponding labels

Substrate surfaces were previously functionalized with APTES. Silanized glass or silica surface becomes highly hydrophilic, which improves the stability of gold adhesion onto it. We also employed the Langmuir-Schaeffer (LS) technique as an alternative. In the LS method, the hydrophilic plate is approached from the air side and is introduced on the interface at a parallel orientation. The advantage of the LS technique with respect to the LB protocol is the absence of a surface-pressure with feedback control during monolayer transfer. In the LS technique it is also possible to submerge the hydrophilic plate prior to particle spreading, but it must be kept on a flat support. The deposition of the monolayer on the solid substrate then happens upon slow suction of the sub phase. Although the LS method bears a technical simplicity, the LB protocol results in a substrate with better lateral structure during transfer and larger scale of homogeneity of the transferred film.

### 3.4.2 Langmuir–Blodgett films as templates for nanostructure formation

We wanted to measure the LSPR signal of the surfaces by using a standard *Vis-NIR* spectrophotometer in order to find any significant particle aggregation and assessing the quality of the Langmuir–Blodgett films. In *Fig. 3.2*, the absorption spectra for LB films, restricted to the vis–NIR window where plasmon absorption occurs, are presented.

Higher surface pressure samples have a higher signal strength, consistently with higher particle concentration in the measurement windows, but there is no significant redshift in the absorption maxima below 17 mN m<sup>-1</sup>. There is a redshift in the adsorption peak for surface pressures above 17 mN m<sup>-1</sup>, indicating monolayer collapse and 3D particle cluster formation. As seen in *Fig 3.2 (a)* it is obvious that particle aggregation is minimized by the proposed protocol. There is a SEM micrograph of the extracted LB film at 17 mN m<sup>-1</sup>. The highest nanoparticle density and formation of 3D aggregates are obvious in *Fig 3.2 (b)*. White part of the image are related to the area with higher density of gold nanoparticle which is due to the monolayer decay and overlapping of particles on each other.

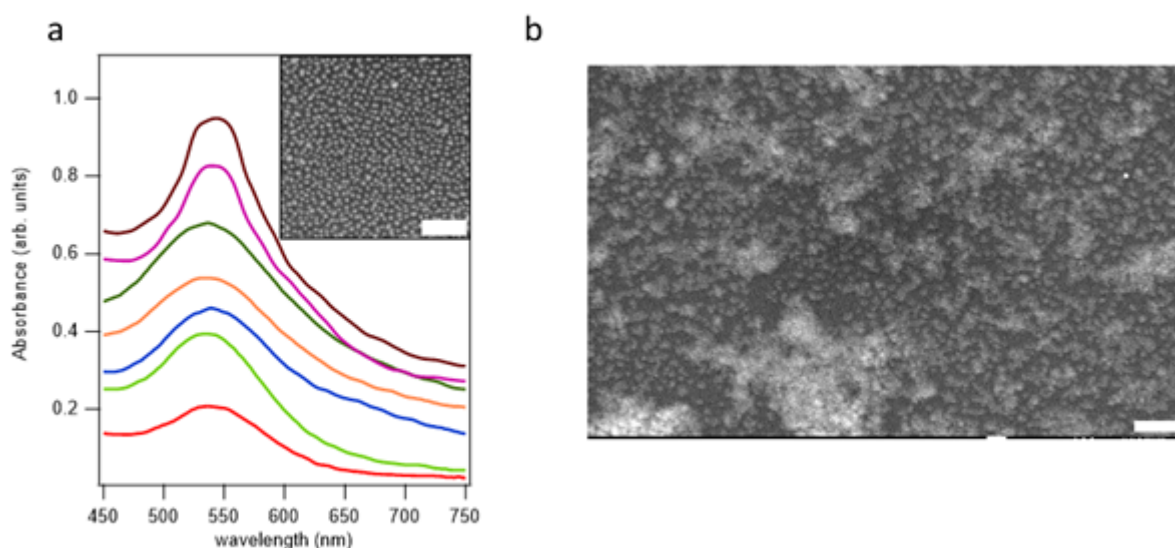


**Fig. 3. 2** a) *Vis-NIR* absorption spectra for LB films of 10 nm gold nanoparticles, prepared under different surface pressures. From bottom to top,  $P = 3, 6, 8, 10, 12, 15,$  and  $17 \text{ mN m}^{-1}$ . In the inset, SEM image for a LB film obtained at  $17 \text{ mN m}^{-1}$ , the scale is 200 nm.

b) Formation of particle aggregation and monolayer decay, the scale is 100 nm

Surface number density of gold particles is around  $1.2 \times 10^2 \mu\text{m}^{-2}$ , as calculated from the SEM image. This value is lower than the nominal value estimated from the isotherm (Fig 3.1). This difference could be related to the incipient 3D particle aggregation.

In order to use gold nanoparticles as a proper SERS substrate, we need to tune the lattice of hotspots. Beside the different control parameters and conditions during Langmuir monolayer formation, electroless gold growth (Fig 2. 5) using the lattice of nanoparticles as a seed layer to grow nanostructures results in the creation of nanostructures of different size and shape [78, 118, 119].

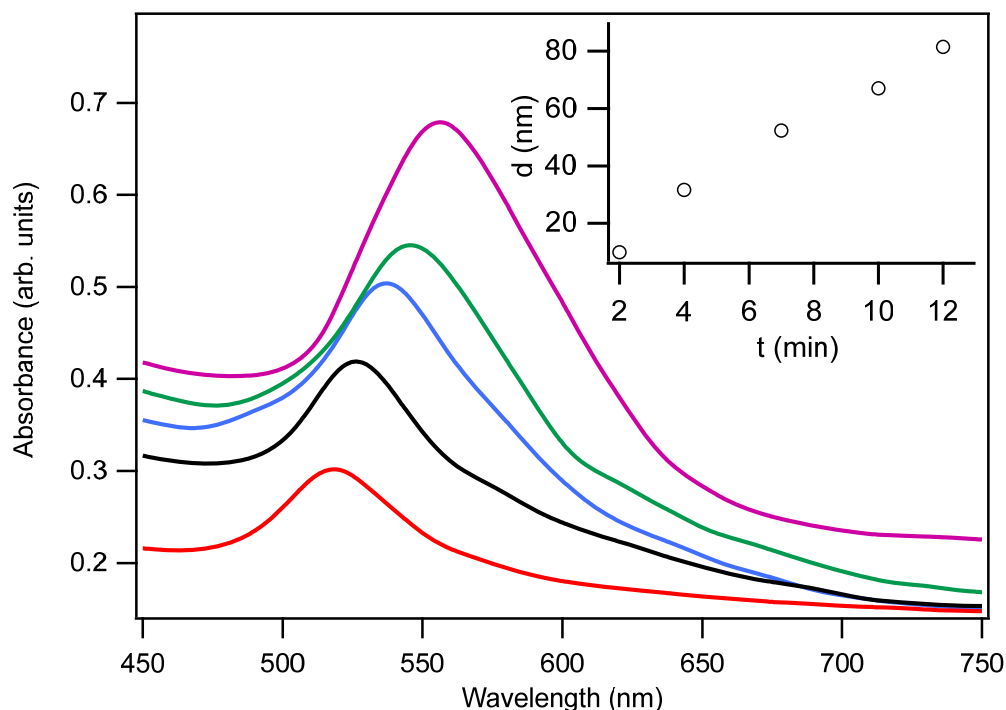


**Fig. 3. 3** Vis-NIR spectra for LB films of 10 nm gold nanoparticles prepared at  $5 \text{ mN m}^{-1}$  of lateral pressure, and different subsequent gold electroplating time. From bottom to top 2, 4, 7, 10, and 12 min. Inset: average hotspot size estimated from the redshift in the spectra

The size, the shape, and the available surface density of the hotspots is adjusted by the electroplating reaction time. There is an increase in the red shift of the absorption maxima in LSPR analysis (Fig. 3.3). This increase is related to the average gold particle size, which increases through seed growth during the electroless procedure. The average hotspot size was estimated by comparing the LSPR redshift with calibration data of gold nanoparticles provided by the manufacturer (see inset in Fig. 3.3). In these experiments, the lateral pressure of

nanoparticle monolayers was tuned at  $5 \text{ mN m}^{-1}$ , corresponding to a nominal density of about  $70 \text{ particles}/\mu\text{m}^2$  at the water/air interface. There is a heterogeneous arrangement of the particles on the surface as seen in SEM images (Fig. 3.4). This arrangement is likely related to the LB extraction and subsequent drying of the aqueous monolayer. Interparticle repulsion at the air/water interface play a main role in their arrangement at the surface. There is an evidence from the LSPR studies (Fig. 3.2) that particle aggregation on the surface is not significant. In (Fig. 3.4) a SEM image obtained by tilting the incidence angle allows us to verify the absence of gold nanoparticle multilayer. The rough surface of gold nanoparticles is visible in the image. Electroless seed growth results in a decrease in hotspot number density and an increase in hotspot size.

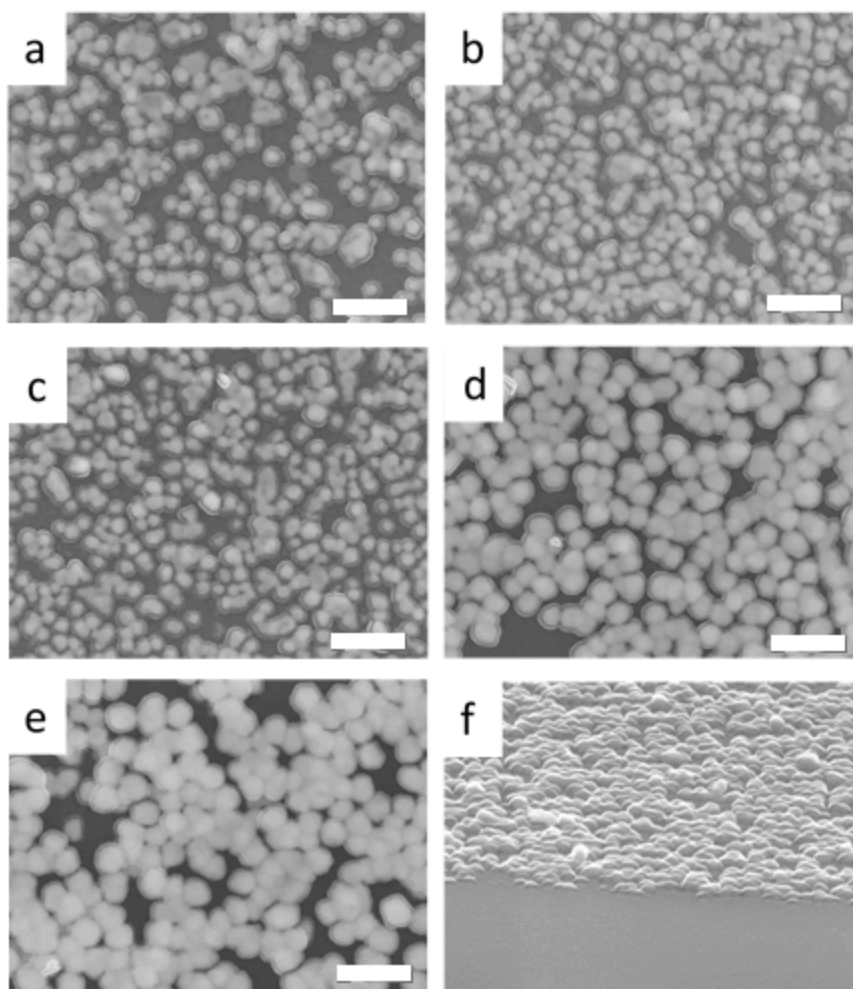


**Fig. 3. 4.** SEM micrographs of nanoparticle LB films after different gold electroplating time, from (a) to (e), 2 min, 4.5 min, 8 min, 10 min, and 12 min, respectively. LB films had been transferred at  $8 \text{ mN m}^{-1}$ . (f) Tilted image of the same substrate in (e). Scale bars are 500 nm long.

### **3.4.3 SERS performance of the gold monolayers**

We used 4-MBA as a reference organic molecule for SERS study of the prepared substrates and we studied the influence of the control parameters on the SERS measurement. 4-MBA chemisorbs to the surface of gold particles with a stable covalent bond. This organic molecule could amplify plasmonic effect and lead to intense peaks in Raman scattering measurements (sec 2.5.10.1).

The family of 4-MBA SERS spectra on the substrates prepared with the LB technique at several surface pressures of gold NP on silica substrate are shown in *Fig. 3.5*.

All samples were electroplated with gold for 8 min using the electroless plating method described in (sec 2.5.8). In all samples we tracked the two well-known peaks of 4-MBA at  $1076\text{ cm}^{-1}$  and  $1588\text{ cm}^{-1}$  and the rest of the spectrum were filtered out by using the Lab-Spec software (sec 2.4). We observed that the intensity of 4-MBA peaks were increased by increasing lateral pressure of the precursor monolayer from 3 up to  $13\text{ mN m}^{-1}$ . Moreover, we saw a decay in the detection performance of SERS when the lateral pressure was above  $13\text{ mN m}^{-1}$ , which could be related to the monolayer collapse and overlapping gold NP layers. Overlapping gold monolayers may lead to aggregation, which could cause a disorder in the homogeneity of gold layers. This disorder can lead to a decrease in the density of hotspots. *Fig. 3.5 b* shows the height of the main 4-MBA peaks. Both peaks feature a maximum at  $13\text{ mN m}^{-1}$ , which we recognize as a limit of monolayer stability in this study. There seems to be a remarkable resonance at a well-defined packing density (corresponding to  $13\text{ mN m}^{-1}$ ). However, these peaks could also be interpreted as a degradation of the substrate performance due to the formation of multilayer patches. In *Fig. 6c* we also calculated the area of the peaks, and a similar trend was observed with even sharper peaks at  $13\text{ mN m}^{-1}$  of lateral pressure.

We also studied the performance of substrates prepared at a common lateral pressure as a function of electroplating time (*Fig. 3.6*). These experiments were performed at  $12\text{ mN m}^{-1}$  (within the limits of monolayer stability) as the lateral surface pressure. These data suggest the presence of a resonance at around 9 min of electroplating time. Analogous results are obtained when either the peak maxima or the integrated peak intensities are considered (*Fig. 3.6 a, b*).

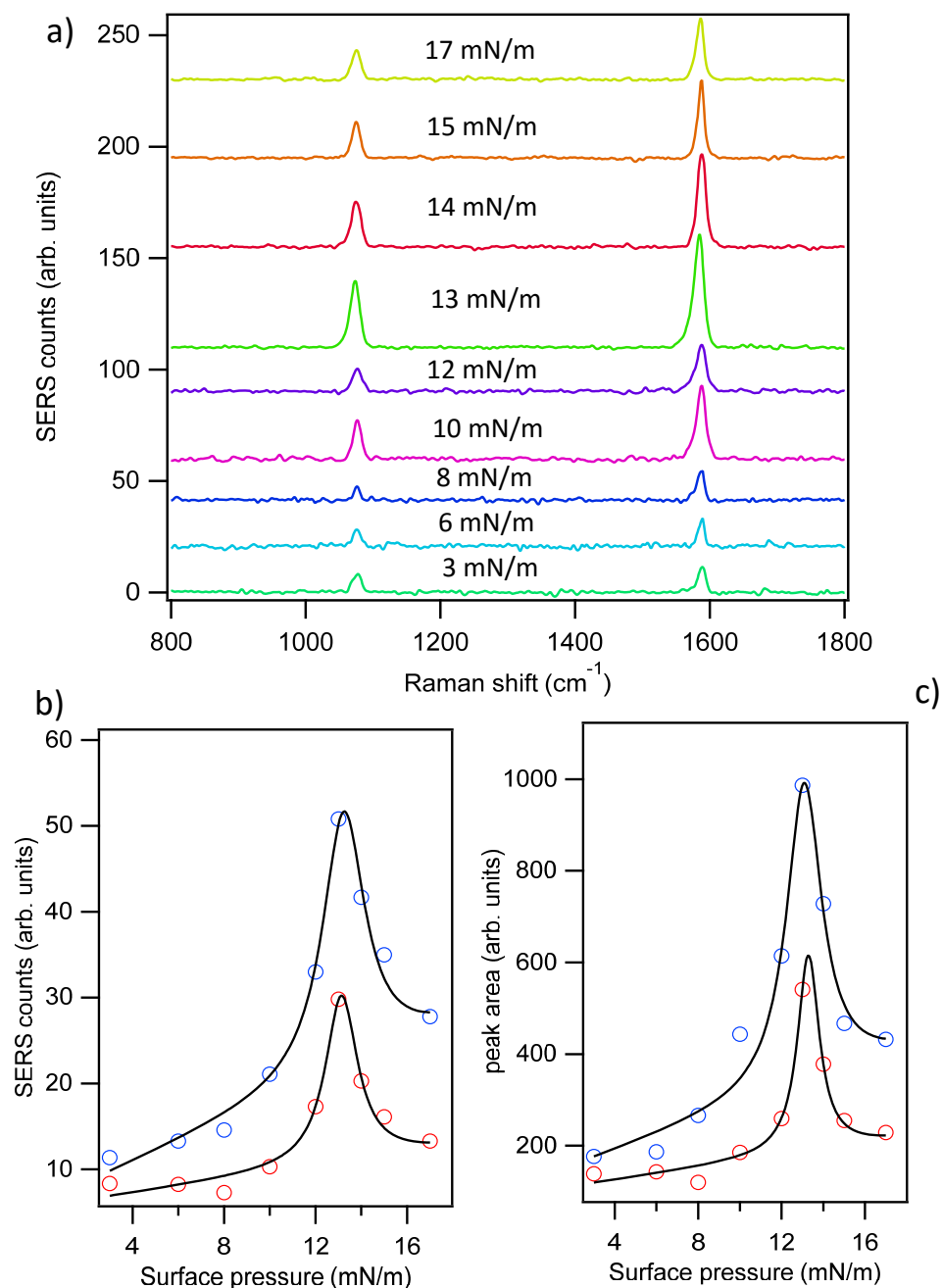


**Fig. 3. 5** (a) SERS spectra of 4-MBA adsorbed on gold nanoparticle monolayers transferred at different lateral pressures, followed by an electroplating time of 8 min. (b) Height of the peaks at 1076  $\text{cm}^{-1}$  and 1588  $\text{cm}^{-1}$ . (c) Area of the peaks at 1076  $\text{cm}^{-1}$  and 1588  $\text{cm}^{-1}$ . The lines through the data are guides for the eye

All peaks are more intense, and spikes are more remarkable when using the integrated intensities. An important point in the spectrum is about the shape of the

peaks, which became bigger in 9 min as electroless plating time, but these data about shape and area under the peaks are somewhat less amenable to further study. Effective hotspot size is around 60 nm for 8 min electroplating time, as obtained from the LSPR data in *Fig. 3.3*.

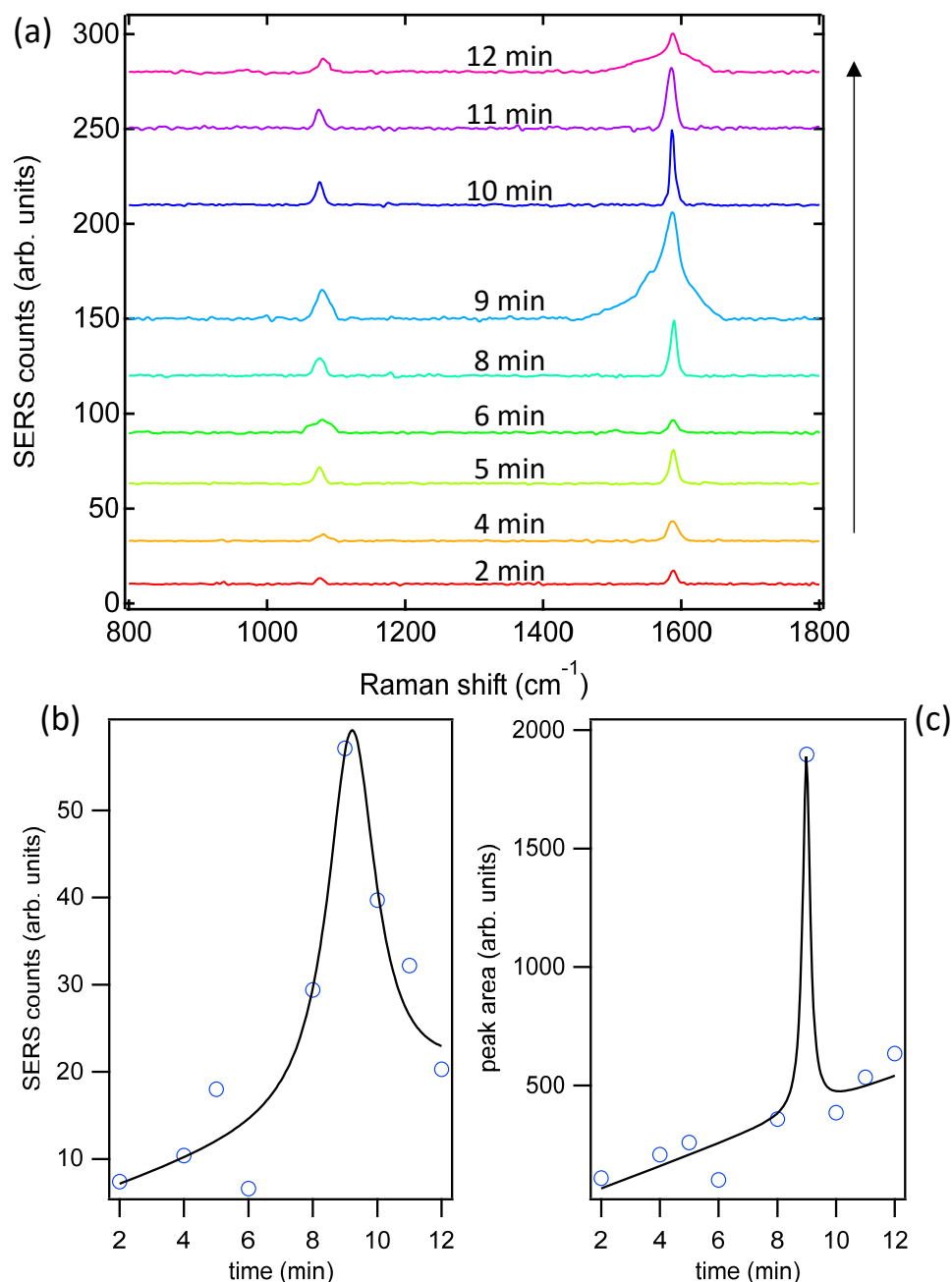


**Fig. 3. 6** (a) SERS spectra of 4-MBA adsorbed on gold nanoparticle monolayers at a lateral pressure of 12 mN m<sup>-1</sup>, followed by different electroplating times. (b) Height of the peaks at 1588 cm<sup>-1</sup>. (c) Area of the peaks at 1588 cm<sup>-1</sup>. The lines through the data are guides for the eye

In the next chapter, we study the possibility of improving the SERS sensitivity by using monolayers prepared with nanoparticles of different diameter than those used in the present study. In this chapter, we tuned and increased the surface roughness of nanoparticles by means of electroplating technique. Increasing in surface roughness led to a resonant-like behavior in the SERS spectrum. All in all, we need to perform more experimental studies and compare them with theoretical models to discover the reason for the mentioned behavior.

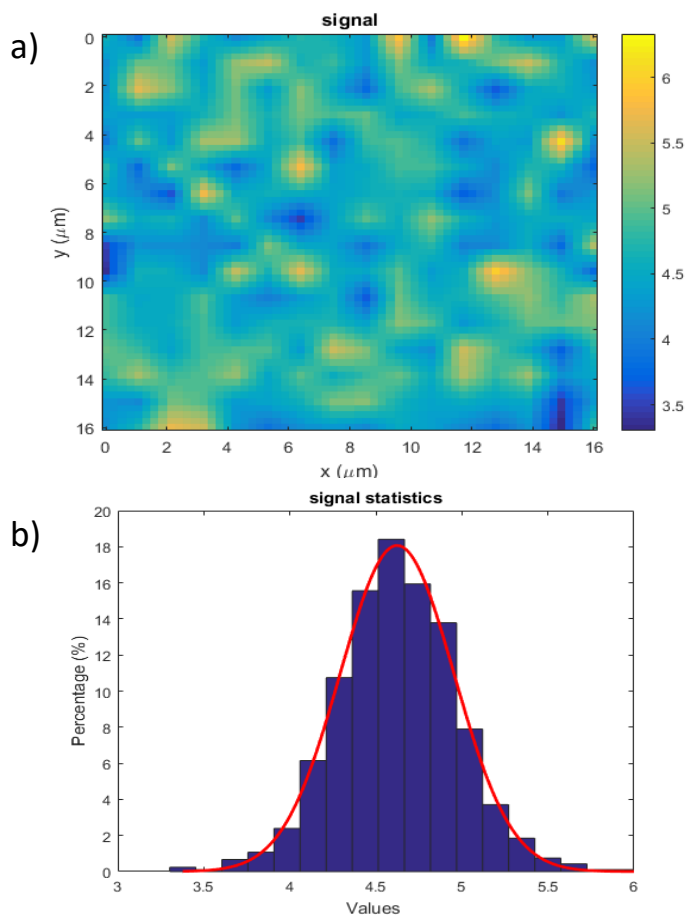


**Fig. 3. 7** (a) SERS scan of the 1077 cm<sup>-1</sup> peak in a sample of 4-MBA adsorbed on a gold nanoparticle monolayer transferred at a lateral pressure of 15 mN m<sup>-1</sup> and an electroplating time of 8 min. Data has been acquired with the 50× microscope objective. (b) SERS intensity distribution in the 15 μm × 15 μm region shown in (a). The solid line is a gaussian fit giving an average intensity 4.4 (arb. units) and a standard deviation 0.7 (arb. units)

Finally, we assessed hotspot homogeneity and their distribution in the nanostructured substrates. We used SERS mapping to monitor the  $1588\text{ cm}^{-1}$  4-MBA peak (integrating from  $1530$  to  $1625\text{ cm}^{-1}$ ) in a region of  $15 \times 15\text{ }\mu\text{m}^2$  and  $1\text{ }\mu\text{m}$  step size (*Fig. 3.7*). A pseudo-random pattern was detected in the distribution of SERS intensity with a dispersion of 8% about the mean value. Disordered particle assembly, aggregation, presence of trace impurities and homogeneities in the electroplating process are examples of phenomena which could lead to a reduction in the homogeneity of the gold NP layer on the solid surfaces.

### **3.5 Conclusion**

A facile and cost-effective protocol for the preparation of tunable SERS substrates of gold nanoparticles by using LB technique was introduced in this part of the study. Gold nanoparticles are commercially-available and water-based, and are further capped with organothiols in this study, allowing to disperse them in chloroform as a volatile solvent. The capping agent avoids unwanted aggregation and enables them to spread at the interface of water/air. For the 10 nm gold particles used in this chapter, the enhancement of 4-MBA SERS signals can be tuned using two control parameters: the packing density of gold NP during the preparation of a monolayer and tuning of the gold layer thickness by means of electroless plating. Both protocols suggest the emergence of a resonance in the SERS intensity at well-defined nanoparticle lateral density or gold electroplating time, whose physical origin is yet unclear and should be further studied.

***4. Effect of gold nanoparticle size and shape on the SERS performance***

## **4.1 Preface**

In this chapter we describe the effect of gold nanoparticle shape and size on SERS spectra of a target molecule (4-MBA). The Langmuir-Blodgett technique, in which a monolayer of nanoparticles is first spread at the interface of water/air, was used in the first stage of this study. In the previous chapter, we demonstrated that fine-tuning of the lateral packing and subsequent seed growth of 10 nm gold nanoparticles led to enhanced SERS signals of 4-MBA. To continue our research, we want to improve our solid substrate in order to reach more intense SERS spectra by using NPs with different sizes (5-40 nm) and shape (urchin-shape). Finally, we have tested our substrates to measure SERS signals of Thiram as a typical water pollutant.

## **4.2 Introduction**

The spatial form of substrate particles and lattices of hotspots play an important role in the improvement of SERS spectra. Efficiency of the SERS method is highly depend to the surface nanostructure of the substrate. Distance between hot spots is one of the aspects in their LSPR performance. It is also difficult to determine the optimal distance between particles. LSPR is a function of several parameters such as packing density of substrate particles, their shape and surface roughness and their size. These factors are directly influenced by the nanoparticle manufacturing technique [120-122]. SERS performance is a result of interaction between incident light and LSPR (*sec 1.3.2*). Major efforts of researchers active in the field of SERS are related to maximize LSPR effect to reach better SERS spectra [123, 124]. Preparing substrates with nanoparticles of different size and shape of has been considered by researchers in recent years. It should also be noted that size, shape and packing density of gold nanoparticles are selected based on the physical properties of the target device [104, 125]. We prepared SERS substrates by using Langmuir-Blodgett (LB) as a self-assembly method in the first phase of our experiment (*sec. 2.5.4 and 5*). We tuned packing density of nano particle by means of surface pressure adjustment in the LB setup. Changing size and shape of gold nanoparticles could result in localized plasmon change which can improve SERS signals [126, 127].

In the previous chapter, we used 10 nm spherical gold nanoparticles that we deposited at solid surface using the LB technique. Then, we used the monolayers

of gold NP as seeds for an electroless process, which resulted in nanoscale hotspots with a larger effective final size. To continue and improve our last results, we want to explore the effect of employing gold NPs of different sizes to prepare monolayers and find an optimal core size to manufacture SERS substrates. Since we believe that the surface of the particles is not smooth and their roughness are increased by means of electroplating technique, we want also to study the possibility of using custom-made non-spherical NPs to control the hotspot roughness in a better way and enhance the quality of SERS detection. Finally, we demonstrate that intermediate size spherical NPs lead to fabricate optimal SERS substrates. The balance of packing density and roughness are the two main aspects for SERS detection of a test analyte. We also found that using urchin-shape gold nanoparticles instead of spherical ones led to a significant improvement in SERS performance. In the last step of this chapter, we study the feasibility of using our optimal substrates to detect water pollutants as a real case study.

### ***4.3 Experimental***

We used spherical gold NPs of several diameters (5, 10, 20, 30 and 40 nm). All gold NPs were purchased from Sigma-Aldrich and were used as received. We also used urchin-shape nanoparticles (gold nanostars) in this part of the study. They were fabricated by the author as described in chapter 2. After preparing SERS substrates by means of the LB technique using fused silica surfaces, we tuned the size of the hotspots by using electroless deposition of gold. The prepared substrates were incubated in a 4-MBA aqueous solution after cleaning under O<sub>2</sub> plasma, rinsed with Milli-Q-Water and dried under a stream of N<sub>2</sub>. (*chapter 2*).

The surface of samples and nanoparticles were monitored with SEM for NP layers and TEM for individual NP. Raman spectra were obtained as described in *chapter 2*. We deposited 300  $\mu$ l of 10  $\mu$ M 4-MBA aqueous solution (*sec 2.5.10.1*). we used a stock solution of 10  $\mu$ M For Thiram detection. The stock solution was diluted with Milli-Q water to reach 1  $\mu$ M. We used Lab spec (*ver. 5*) and Igor-pro (*ver. 8*) to process the SERS spectra.

## 4. 4 Results

### 4. 4. 1 Monolayers of Spherical Gold Nanoparticles

In the previous part of study (*chapter 3*) we came to the conclusion that by using optimal electroless plating time (8–9 min), the effective size of hotspot will be around 50 nm. Since there is a red shift in the adsorption spectrum of rough NP in comparison to smooth NP [36], we expect that the spherical core of the optimal hotspot size should, in reality, be significantly lower than 50 nm (*Fig. 4.1*). We, therefore, expect that the optimal SERS performance should be obtained with gold NP smaller than 50 nm in diameter. We used gold NPs of sizes 5–40 nm, and studied the performance of LB films at different surface pressure.

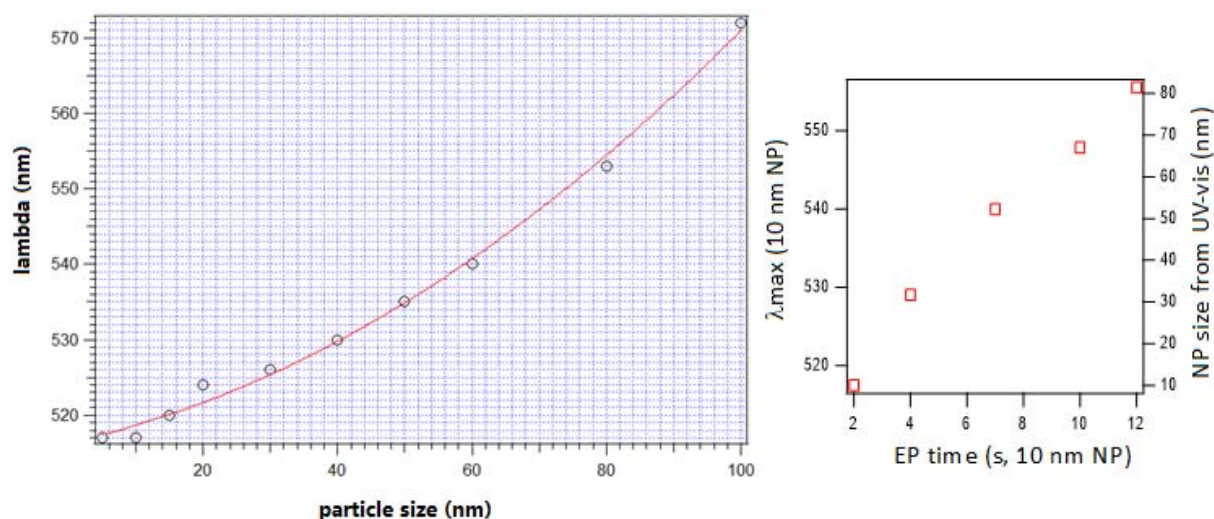


**Fig 4. 1** Maximum wavelength of UV–vis absorption spectra of monolayers of 10nm gold NPs that act as seeds, after different gold electroless plating time. The spectrum is compared with that of gold NP of different sizes to provide with a rough estimation of the hotspot size

All of the NP substrates were electroplated with gold for 8 min, as we found this time to be near optimal in the previous chapter. The size and roughness of gold particles increased by means of electroplating. The state of the spread monolayers was monitored by tracking the surface pressure in real-time by means of a Wilhelmy balance. There is a direct relation between lateral packing and effective surface pressure, related to the capillary-mediated interparticle interactions and repulsion between electrical double layers. NP monolayers are metastable and

have a brittle structure. Films may collapse into third dimension when we reach above a critical surface pressure [19]. Obtained NP monolayers are assessed by SEM imaging to monitor the quality of the films. Packing density has an inverse dependence with particles diameter, since stronger capillary effects result in enhanced inter-particle repulsion.

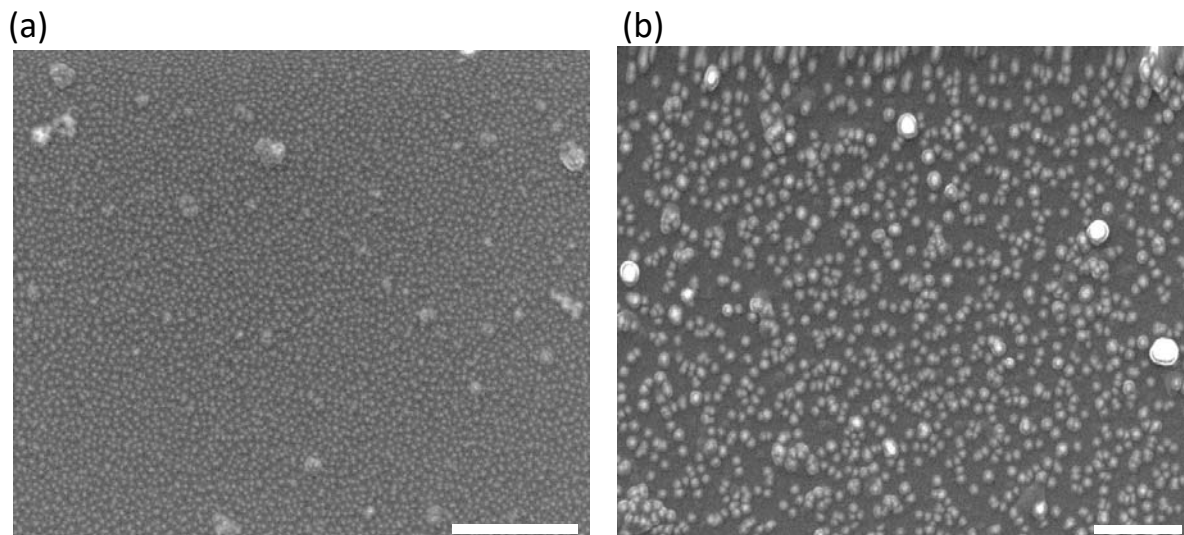


**Figure 4. 2** SEM micrographs of spherical gold NP Langmuir–Blodgett (LB) monolayers prepared at  $12 \text{ mN m}^{-1}$  of lateral pressure and without further gold electroless plating. Images correspond to NPs of 5 nm (a) and 40 nm (b). Scale bars are 500 nm

5 nm NPs show a high number density at the surface in comparison with 40 nm NPs (*Fig. 4.2*). However, it is not obvious that the higher hotspot density should result in an enhanced SERS effect. Not only packing density of particles play a role in SERS enhancement, but also the size of the hotspots has also an influence on the plasmonic effect. SEM images are an evidence of the absence of gold multilayers, in agreement with BAM monitoring of the water/air interface. There are some visible gold clusters on the substrate that can result from aggregation of particles that either existed in the original NP suspension or that formed upon LB film extraction. The effect of particle clusters on SERS spectra are weak and could be neglected.

#### ***4.4.2 SERS Performance of Spherical Gold Nanoparticle Monolayers***

We used 4-MBA as the standard target analyte as we achieved proper SERS result in the previous part of the study. We studied the effect of NP size and lateral

pressure on the SERS detection of this target molecule. We collected the full set of SERS measurement (*Fig. 4.3. a*) to compare the effect of surface pressure and NP size simultaneously. We have chosen 8 min as the common gold electroless plating time and have applied it to all NP monolayers. This time was optimized for 10nm NP in chapter 3. We have focused on the data of main peaks by using a band-pass filter around  $1076\text{ cm}^{-1}$  and  $1588\text{ cm}^{-1}$ . These peaks were recognized as the main SERS peaks of 4-MBA.

Initial observation of SERS spectra indicated that the optimal signal in all experiments corresponded to 10 nm NP at  $13\text{ mN m}^{-1}$  lateral pressure. The only exception is in lower lateral pressures ( $6$  and  $8\text{ mN m}^{-1}$ ), where the height of the peaks for 20 nm nanoparticles are higher. Variation of lateral pressure acts in a different way in monolayers prepared with different size of NP, and this parameter has the strongest influence in monolayers of 5 nm and 10 nm. This effect is much weaker and more subtle for larger NP (*Fig. 4.3 b*), where there is less than a 20% improvement in signal strength across all surface pressure values. The height of the  $1588\text{ cm}^{-1}$  as a function of particle size is shown in *Fig. 4.3 c*), by analyzing the height dependence on NP size, we estimate that nanoparticles which are slightly larger than 10 nm might give the optimal signal intensity. Nevertheless, the predicted further enhancement would be small with respect to 10 nm NP, and fine tuning the electroless plating time for 10 nm NP may be a better option to seek the optimal performance of spherical gold NPs.

We mentioned in (*sec. 3*) that best results of SERS were referred to 10 nm NP  $13\text{ mN m}^{-1}$  as surface pressure, following with 8 min of electroless plating. In the other word we found the optimum SERS substrate fabricated in mentioned condition among several fabricated substrate. We performed SERS measurement with different size NP to verify if bigger or smaller NPs in comparison with 10 nm NP show remarkable change in final spectra. While the density of hotspots can be much higher for smaller NP (*Fig. 4.2*), the final size achievable through electroless plating is limited by the merging of neighboring NP. The other factor that causes a significant effect on the SERS spectra is electroplating, which results in significantly rougher entities in comparison with the original NP [19]. Although the Langmuir–Blodgett technique followed by EP growth is flexible and efficient, we cannot improve our reported results with 10 nm NP when using larger gold particles. In the next step we use urchin-shaped NP. By changing the particles' geometry and tuning their roughness during synthesis, we tried to improve our results with spherical NP.

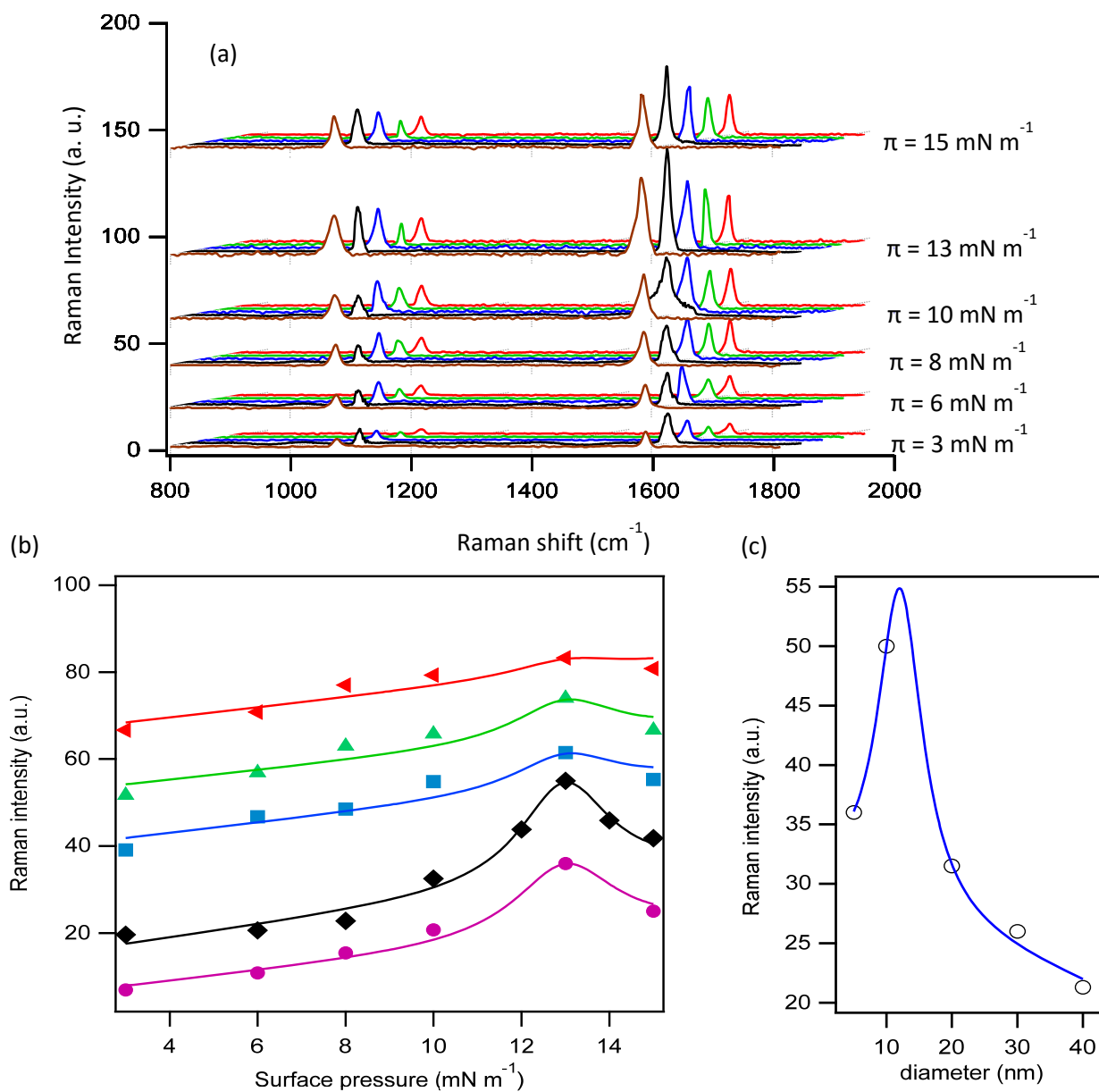


**Fig 4. 3** (a) Surface Enhanced Raman Spectroscopy (SERS) spectra of 4-MBA adsorbed on gold spherical NP monolayers prepared at different lateral pressures (as indicated in each series) and 8 min of gold electroless plating time. For each series, and from front to back, NP sizes are 5 nm, 10 nm, 20 nm, 30 nm, and 40 nm. (b) Height of the SERS peak at  $1588 \text{ cm}^{-1}$  for the data in (a). From bottom to top, NP size is ordered as in (a). (c) Height of the SERS peak at  $1588 \text{ cm}^{-1}$  and a surface pressure of  $13 \text{ mN m}^{-1}$ , as a function of NP size. The lines through data are guides for the eye

### **4.4.3 SERS Performance of Urchin-Shaped Gold Nanoparticle Monolayers**

We used well-established protocols to synthesize urchin-shape NP, henceforth called gold nanostars (*chapter 2*). We grow gold on spherical gold seeds as a core, resulting in the formation of nanoparticles with a rough surface and sparse spikes. The final size of NP synthesized with this protocol is about 50 nm in diameter (*Fig. 4.4 a*). We used our usual protocol for preparing monolayers at the water/air interface by means of the Langmuir–Blodgett technique. One of the advantages of using urchin-shape NP as a SERS substrate is their rough shape. Their shapes would enable spike interdigitation between neighboring particles, allowing to reach high packing densities (*Fig. 4.4 b*). We expect that such high packing density would cause a reduction in the SERS performance of the resulting hotspots [36, 128]. In addition to this phenomenon, we also expect an optimal SERS performance at lower lateral pressures in comparison with substrates which are prepared with monolayers of smooth NP.

Our results and observations of SERS measurement when using urchin-shaped NP are mostly similar to smooth NP, as the height and intensity of 4-MBA peaks increases monotonically with surface pressure until we reached a maximum amount at  $10 \text{ mN m}^{-1}$  (*Fig. 4. 4 c and d*), a value of lateral pressure sensibly lower than for spherical NP.

We mentioned about a possible reason for this, as we expect that high packing densities could result in reduced performance due to nanostar interdigitation. The most significant finding in this part is that the height of the  $1588 \text{ cm}^{-1}$  peak at optimal performance is significantly higher than the result we achieved using spherical NP (*Fig 4.3 c*). Although, by using electroless plating of the spherical NP, we could add roughness to their surface, being able to adjust the roughness of the hotspots is crucial to achieve optimal SERS performance. The mechanism of the gold growth by electroless plating is clearly different from the one achieved during nanostar synthesis, and the former results in smoother surfaces.

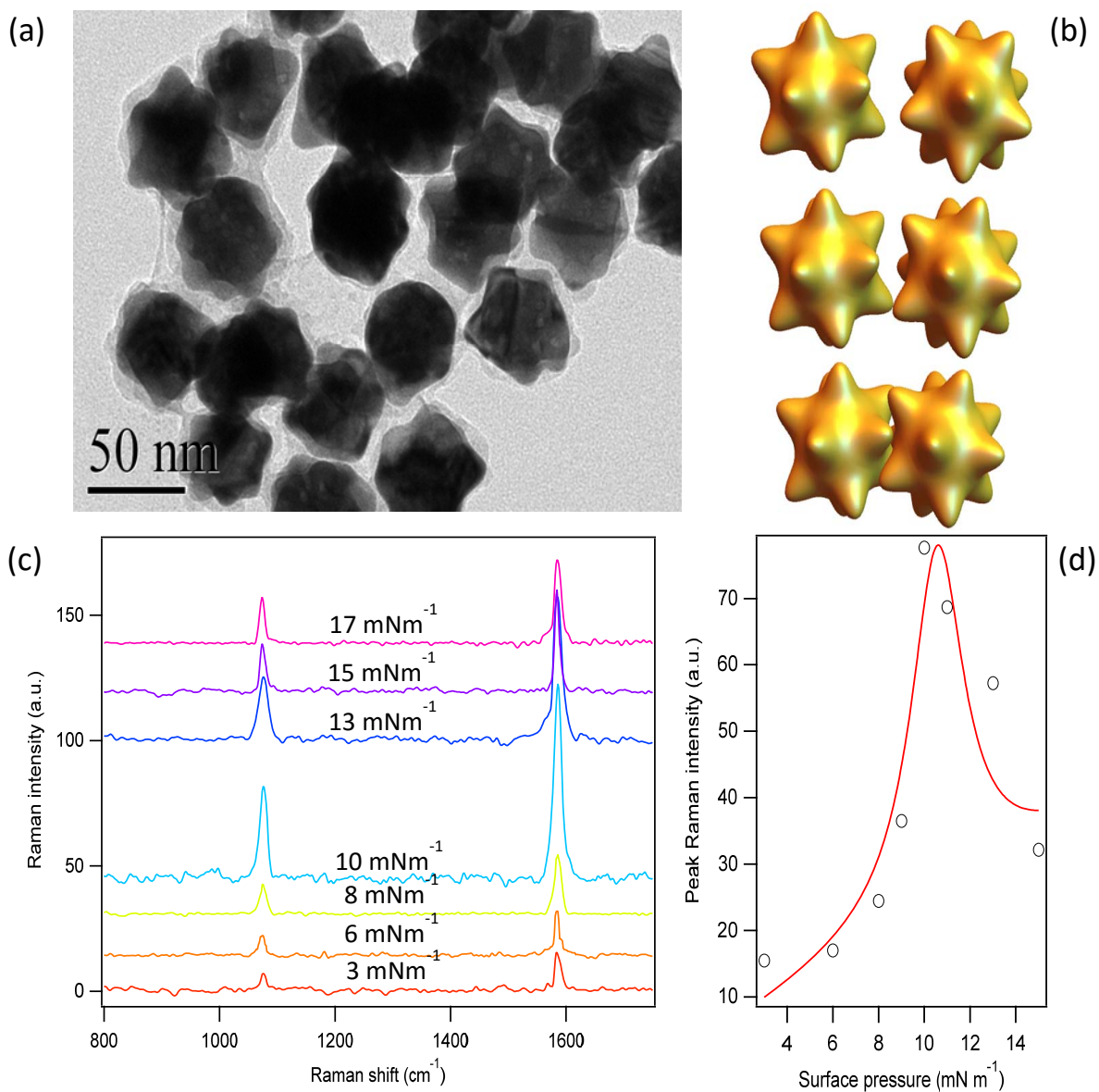


**Fig 4. 4** (a) TEM image of synthesized gold nanostars. (b) Sketch of gold nanostars as the lateral packing density is increased, leading to overlaps that degrade the SERS performance. (c) SERS spectra of 4-MBA adsorbed on gold nanostars prepared at different lateral pressures and 8 min of gold electroless plating time. (d) Height of the SERS peak at  $1588\text{ cm}^{-1}$  at different surface pressures. The line through data is a guide for the eye.

#### ***4.4.4 Homogeneity of the SERS Substrates and Detection of Thiram***

We measured the homogeneity of the gold layer on the prepared substrates to evaluate their quality and their SERS performance. We used the SERS mapping technique in an area of  $15\mu\text{m} \times 15\mu\text{m}$ , at  $1\mu\text{m}$  steps for the  $1588\text{ cm}^{-1}$  peak of 4-MBA. The SERS signal is integrated from  $1530$  to  $1625\text{ cm}^{-1}$  for each  $1\mu\text{m}^2$  area (*Fig. 4.5*). We have done mapping analysis for monolayers of nanostars and for NP of  $5\text{ nm}$ ,  $10\text{ nm}$ , and  $30\text{ nm}$ , prepared at the optimal performance conditions (*see above*). In order to compare the quality of all substrates in terms of their homogeneity, we characterized the noisy pattern of SERS intensity distributions after normalizing and computing their statistical distribution. The signal variance of urchin-shape nanoparticles is the lowest of all tested samples in our study, with an intensity dispersion of around 3% over the explored area (*Fig. 4.5 a*). The lowest variance of spherical NP was observed for  $10\text{nm}$  NP at around 8% (*Fig. 4.5 b*), and variance dispersion increased to 20% for both smaller and larger particles (*Fig. 4.5 c and d*). There are two possible reasons to justify the signal dispersion, namely, inhomogeneities in the electroless plating process and infiltration of organic impurities between substrate particles during the 4-MBA adsorption process. However, here we have performed a systematic study where all protocols are identical except for the size or shape of the employed NP, finding a trend that merits some further explanation.

The presence of chemical impurities on the substrates is probably one of the reasons which causes SERS signal dispersion. In order to study this effect, we focus on the gold electroless plating. When we achieved optimal lateral density for small NP (*Fig. 4.2 a*), we obtained hotspots that included merging of neighboring NP upon electroless plating. This random process contributes to the formation of a wide range hotspot sizes and to increase SERS variance percentage. From another point of view, when we use larger NP and optimal surface pressure, gold particles are deposited on the solid surface with more interparticle distance and this results in a sparse lateral packing (*Fig. 4.2 b*). NP sparse packing on the surface implies a substantial variance in the SERS signal of the mapped area. SERS enhancement is a function of the electromagnetic field around substrate particles, and core to core distances between gold particles have an effect on the localized surface plasmon and the electromagnetic field. Neighbor particles could

improve the LSPR by coupling their evanescent field and employing synergy phenomena.[129-131].

Although electromagnetic fields between particles could be calculated using mathematical models, but for “traditional” SERS substrates, such as metal particles, it is very difficult to actually control the degree of electromagnetic coupling. As discussed above with spherical NP, the spatial variance of the SERS signal is minimized when using 10nm NP and optimum surface pressure conditions. Therefore, we come to the conclusion that when we achieved optimal performance of the SERS signal, the spatial variance is also minimal. This idea is further validated by the observations with nanostars. These substrates indicated both the highest SERS performance and lowest dispersion variance among all tested NP. Despite the obtained results in this study about a relation between SERS performance and signal variance, a clear understanding of this phenomenon is not readily available. Further analysis and study are needed to verify this idea in the future.

In the next step, after having found the optimal condition of SERS for several types of substrate and 4-MBA as a target analyte, we have prepared substrates with nanostars and with 10 nm spherical NP, following the previous protocol (*chapter 2*), to test and detect a 1  $\mu\text{M}$  solution of Thiram, corresponding to 240 ppb. We choose Thiram as a typical water pollutant since it is an extremely widespread fungicide and could be found in the water sources around farmlands, particularly in developing countries. We prepared a primary SERS measurement on Thiram molecules to evaluate the feasibility of detection with the described protocol. The SERS signal of Thiram was measured using 10 nm gold nanoparticle monolayers at 13  $\text{mN m}^{-1}$  and gold nanostar monolayers at 10  $\text{mN m}^{-1}$  (*Fig. 4.6*). Nanostar particles have shown the highest intensity SERS signal and also a good signal to noise ratio. We reached acceptable homogeneity in the SERS performance of the prepared substrates, which could be used to detect very low concentrations of water contaminants. This feasibility opens a very promising strategy towards the development of efficient and optimized SERS chemical sensors.

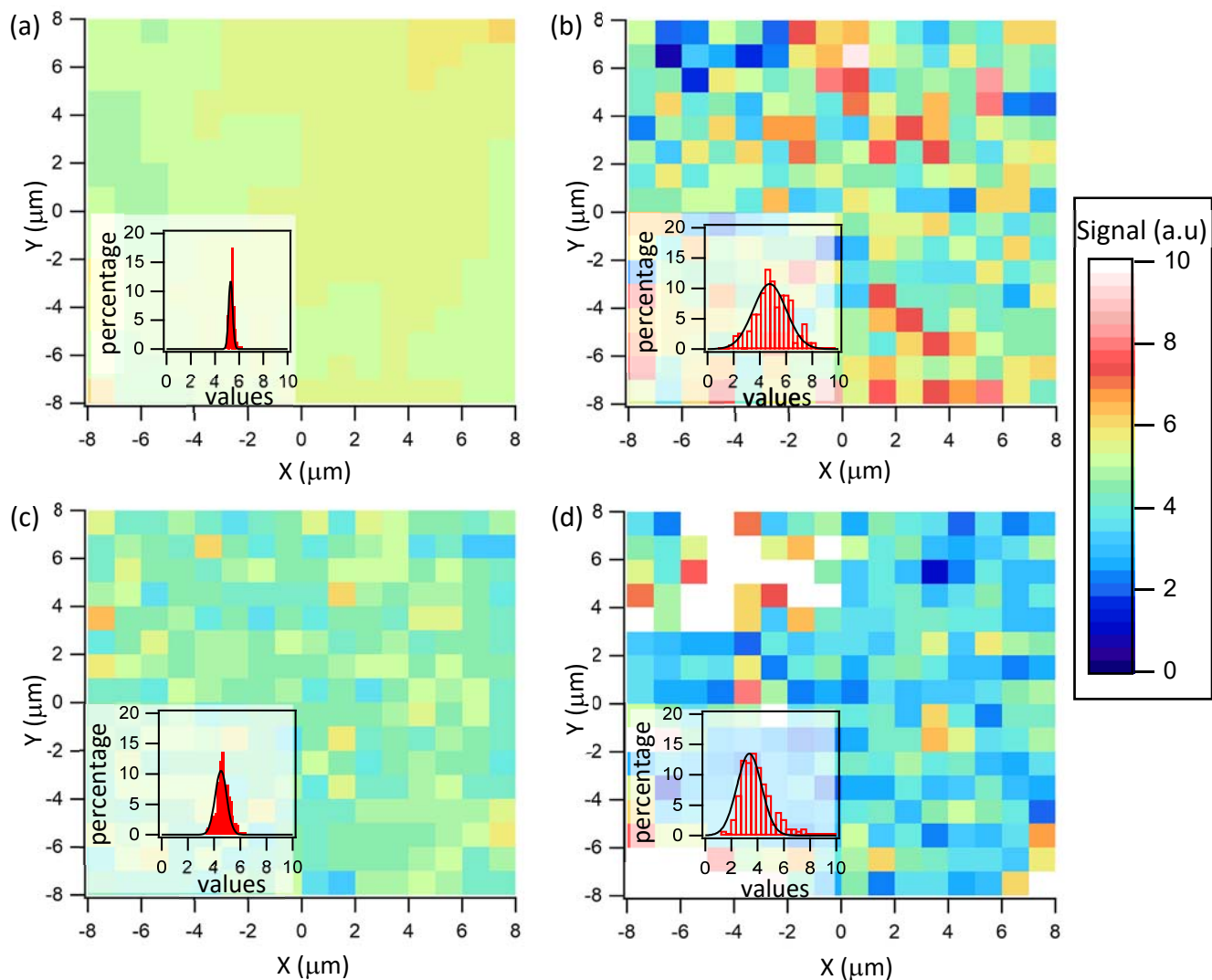


**Fig 4. 5** SERS scan of the  $1588\text{ cm}^{-1}$  peak for 4-MBA adsorbed on different gold NP monolayers prepared at the optimal lateral pressure and an electroless plating time of 8 min. Data correspond to gold nanostars (a), 10 nm gold NP (b), 5 nm gold NP (c), and 30 nm gold NP (d). The distribution of intensities is plotted as an inset in each case, and a Gaussian is fitted to each distribution as a guide for the eye

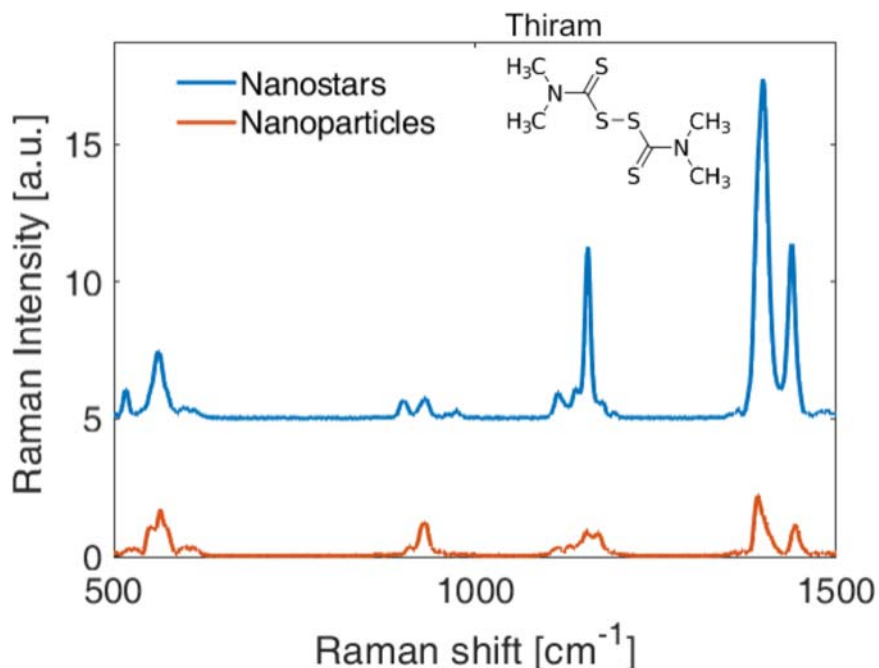


**Fig 4. 6** SERS signal and detection of 1  $\mu\text{M}$  of Thiram in water (240 ppb) for nanostars and nanoparticles-based substrates realized with the optimal pressures of, respectively, 13  $\text{mNm}^{-1}$  and 10  $\text{mNm}^{-1}$

## 4.5 Conclusions

In this chapter, we have studied the effect of the size of NP on SERS performance. SERS substrates were prepared through the tailored self-assembly of gold NP by means of the Langmuir–Blodgett technique. We studied the effect of lateral pressure and further in-situ hotspot growth through gold electroless plating on the substrate. We have extended the study from *chapter 3*, which was related to 10 nm spherical NP, using other sizes of spherical NP and urchin-shaped NPs. Our findings show that optimal performance of SERS could be achieved with spherical NPs with diameter slightly above 10 nm. There are two factors which influence the SERS performance in our study. First, the high hotspot density achievable in the case of using small NP that will easily coalesce with each other during gold electroless plating, and second, the sparse packing density of larger NPs that yield individual hotspots after the electroless plating process. Our results show that using nanostars instead of spherical NP results in better SERS signals. This fact indicates that, although we can increase surface roughness of the spherical

particles by means of electroless plating, preparing a monolayer with custom-synthesized urchin-shape NP with controlled roughness is a better option. Finally, we evaluated the feasibility of detecting a water contaminant (Thiram) by means of the SERS technique using our fabricated substrates. We could satisfactorily detect Thiram from a 240 ppb solution by using both nanostar and 10 nm particles.

Moreover, we performed SERS mapping to study the homogeneity of the signal from the nanostructured surfaces and we found a correlation between surface smoothness and SERS performance. Optimal substrates (nanostars and 10 nm particles) which lead to a better SERS signals have shown also to have the most homogeneous distribution.

## ***5. SERS detection of water pollutant substances***

## **5.1 Preface**

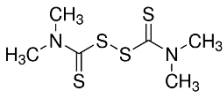
In the previous chapters, SERS technique was introduced as a practical method to identify organic molecules such as 4-MBA. This method is used as a qualitative tool to study and identify a wide range of organic compounds. In this study, after identifying the molecule 4-MBA and optimizing the substrates used with the mentioned techniques, we investigated and performed tests on water polluting molecules (Thiram and Carbaryl). Due to the high potential of the SERS technique in tracking and identifying organic substances, it can be used to identify a large number of water and wastewater contaminants.

## **5.2 Introduction**

### **5.2.1 Thiram**

Thiram ( $C_6H_{12}N_2S_4$ ) is a combination fungicide with systemic-contact effects that belongs to the group of Dithiocarbamates. This fungicide is widely used in the disinfection of field seeds and, after the seeds are placed in the soil, an aura of toxin is created around them, which protects the seeds against the invasion of soil pathogens, and even destroys the pathogen after infiltration inside of the seed. This fungicide is well able to control a variety of seed-borne and soil-borne pathogens. Thiram is the simplest form of thiuram disulfide. Thiram is completely soluble in chloroform, acetone and ether.

Thiram has a high penetration power in clay soils as well as soils that contain organic salts. However, due to its short half-life (15 days) in soil, the probability of its penetration into groundwater is very low. But the presence of Thiram in surface water has been reported near places where it is used. Thiram is moderately toxic by ingestion, but it is highly toxic if inhaled. Exposure to humans seems to show clinical symptoms. Headaches, dizziness, fatigue, nausea, and diarrhea are the most dominant symptoms of exposure. It was reported that long term exposure may cause sensitive skin, and it may have effects on the thyroid or the liver. Chemical properties of Thiram are indicated in *Table 5.1*.

IUPAC Name	Dimethylcarbamothioylsulfanyl N,N-dimethylcarbamodithioate
Structural Formula of Thiram	
Chemical Formula	C <sub>6</sub> H <sub>12</sub> N <sub>2</sub> S <sub>4</sub>
Molar Mass	240.42 g·mol <sup>-1</sup>
Density	1.29 g/cm <sup>3</sup>
Melting Point	155 to 156 °C
Boiling Point	decomposes
Solubility in Water	30 mg/L
LD <sub>50</sub> (median dose)	1350 mg/kg (mouse, oral) 210 mg/kg (rabbit, oral) 560 mg/kg (rat, oral)
LC <sub>50</sub> (median concentration)	500 mg/m <sup>3</sup> (rat, 4 hr.)

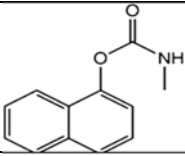
**Table 5. 1** Physicochemical properties of Thiram

There is a report by *Susanne B. Ekroth* in 1998 where she mentioned the detection of Thiram residues in apple, cucumber and strawberry in Sweden. The reported results indicated that 1.6, 0.8 and 3.2 mg of Thiram/kg in apple, cucumber and strawberry, respectively. The maximum residue limit (MRLs) which is accepted by the European Union is 3.0 mg/kg for fruits and vegetables other than mentioned above[132]. Thiram is also used in the rubber industry since 1925. It has been used as an accelerator and vulcanization agent in the industry [133].

### 5.2.2 Carbaryl

Carbaryl (1-naphthyl methylcarbamate) is a chemical from the carbamate family. Carbaryl under the brand name Sevin is a derivative of carbamic acid that has been introduced in recent years to repel plant and animal pests. This insecticide is in the form of wettable powder, consisting of fine solid particles containing dry carriers. Carbaryl has been used commercially since 1958. In the United States it is used as a veterinary drug. Sevin is harmful if absorbed through the skin for humans. It has a potential to cause rapid onset of nausea, vomiting, diarrhea and

abdominal pain if ingested. Inhalation is also harmful and could result in symptoms similar to those from ingestion. Overexposure to Carbaryl is spontaneously and rapidly reversible in the first 30 min of respiratory system contact. Long term exposure is more suspected to cause harmful effects on human health and in case of long term exposure, a serious respiratory problem such as asthma and lung fibrosis will happen. Chemical properties of Carbaryl are indicated in *Table. 5.2*.

IUPAC Name	1-naphthyl methylcarbamate
Structural Formula of Carbaryl	
Chemical Formula	$C_{12}H_{11}NO_2$
Molar Mass	$201.225 \text{ g}\cdot\text{mol}^{-1}$
Density	$1.2 \text{ g/cm}^3$
Melting Point	$142 \text{ }^\circ\text{C}$
Boiling Point	decomposes
Solubility in Water	very low (0.01% at $20^\circ\text{C}$ )
$LD_{50}$ (median dose)	710 mg/kg (rabbit, oral) 250 mg/kg (guinea pig, oral) 850 mg/kg (rat, oral)
$LC_{50}$ (median concentration)	ND

**Table 5. 2.** Physicochemical properties of Carbaryl

### ***5.2.3 Methods for the detection of Thiram and Carbaryl***

There are several reported methods for identification and quantification of pollutants in aqueous media, each having a different sensitivity. Carbaryl could be detected by liquid chromatography with a UV detector (minimum detectable concentration 10 ng/l in 100 ml) [134]. However another research group (Japan Water Works Association, 2001) reported 0.5  $\mu\text{g/l}$  in 500 ml in their study [135]. *UV/VIS* spectroscopy could also be used, but Carbaryl needs to hydrolyze in alkali

media. In their report, the sensitivity of *UV/VIS* spectroscopy method is about 0.2 mg/l [135]. Using *HPLC* with a *UV/VIS* detector has also been reported as a method to measure the presence of Carbaryl in aqueous solution by Portela et al. [135]. *GC* for Carbaryl detection has also been reported by Alvarez-Rodriguez et al with a limit of detection of 20 ng/l.

Similar methods of chemical analysis have been proposed for Thiram. The most important among them are thin layer chromatography, *GC* and *HPLC*. Thin layer chromatography is less sensitive in measuring Thiram than the other mentioned methods. The most sensitive and precise method of measuring Thiram in aqueous solution is the use of *HPLC*, which has a sensitivity of 0.1 µg/l. Spectrophotometric methods have also been used to measure Thiram and are considered as fast but less sensitive methods [133].

Although these methods are reliable, they are time consuming and need to utilize complicated chemicals. The urgent need of analyzing and using easier methods for measuring pollutants has been one of the serious concerns of researchers. The possibility of rapid and daily analysis of various samples to examine them for the presence or absence of contamination has received much attention in recent years. Among these, Raman and SERS spectroscopy can be introduced as relatively accurate and widely used methods to identify organic pollutants in water and wastewater. The advantages of these methods are high measurement speed, ease of manipulation and no need for complex chemical protocols to prepare samples. As mentioned above, due to the relatively high toxicity and the possibility of surface water pollution, the study and monitoring of agricultural products and water resources close to the fields where the pesticides have been used is very important. For this purpose, in the continuation of this study, we investigate and identify the pesticides of Thiram and Carbaryl in aqueous solutions using the SERS method.

### **5.3 methods**

In this part of the research, Thiram and Carbaryl pollutants were selected as two important pollutants that are by-products of pesticides and crops. In this research, aqueous solutions of Thiram and Carbaryl have been used. The SERS technique, which was used in previous sections to measure the presence of 4-MBA in aqueous solutions, was also used in this section. The purpose of using this technique is to study its feasibility to identify contaminants in water qualitatively.

Contaminant concentrations in this study were selected equal to 1  $\mu\text{M}$  and 5  $\mu\text{M}$ . The substrate used was selected similar to the ones reported in previous sections, consisting of gold nanoparticles on a glass surface. The solid substrate was transferred from the water/air interface to the glass surface at different surface pressures using the Langmuir-Blodgett technique. Soluble contaminants were placed at the substrate surface and used for measurement after evaporation of water. After examining and analyzing pollutants, their adsorption isotherms over time were investigated. For this purpose, the prepared substrate was incubated in the aqueous solution of contaminants for different times, allowing for contaminant adsorption. After final washing and drying with a stream of  $\text{N}_2$ , SERS measurements were performed.

By using the adsorption isotherm, the saturation time of the substrate by aqueous contaminant can be detected. The best contact time for better results in SERS can be estimated. In the next step, the fabricated gold substrates were optimized for contaminant adsorption by functionalization with 1-DDT. A chloroform solution with a 1-DDT concentration of 10  $\mu\text{M}$  was placed on the surface of the gold-coated glass substrates and, after evaporation of chloroform, analyte molecules (Thiram and Carbaryl) were deposited on the substrate surface. All samples were analyzed by SERS (sec 2.5.10) using the 785 nm laser under the same conditions reported above.

## **5.4 Results**

### **5.4.1 Thiram detection**

#### **5.4.1.1 Effect of surface pressure**

In the first stage of this part we prepared SERS substrates with different densities of gold nanoparticles using the LB technique (sec. 2.5.3). We used 10 nm gold nanoparticles and  $\approx 40$  nm nano stars in this step. Samples were prepared at 3, 6, 8, 10, 13, 15, 16 and 17  $\text{mNm}^{-1}$  lateral pressures. The surface pressure of the particle monolayer increased upon closing the trough barriers until reaching the maximum of 17  $\text{mNm}^{-1}$  where the monolayer collapsed. Self-assembling and morphology of gold monolayer was monitored with real time BAM imaging. The density of particles on the surface of glass was around 50-120 particles/ $\mu\text{m}^2$ , as measured from the SEM images of glass surface after electroplating. All

substrates were cleaned with plasma after transferring the monolayer to ensure removal of impurities that may interfere during SERS measurement.

Surface pressure	Number of particle per area (particles/ $\mu\text{m}^2$ )
3	55
6	70
10	80
13	95
15	100
17	110

**Table 5. 3** Number of 10 nm gold particles per area on the solid substrate calculated from SEM images.

Thiram has several typical peaks in the SERS spectra which are used to identify this organic pollutant [136]. The main and strongest peak is the one at  $1386\text{ cm}^{-1}$ , which is related to the CN stretching mode. Other peaks are visible at 440, 561, 925, 1150, 1444 and  $1514\text{ cm}^{-1}$ . (*Table 5.4*). By using SERS spectroscopy, it is then possible to perform a qualitative analysis of Thiram.

The sample peaks of Thiram from this study are presented in *Fig. 5.1* There are 6 separated visible peaks in the SERS spectrum of a  $5\text{ }\mu\text{M}$  Thiram solution. The related wavelengths of the peaks from 1-6 are, respectively, 442, 561, 930, 1148, 1386 and  $1515\text{ cm}^{-1}$ . There is a strong signal for Thiram detection with the prepared SERS substrates and showing a good signal-to-noise ratio (*Fig. 5.1*).

Peak wavelength	Chemical structure and specification
440	CH <sub>3</sub> NC deformation and C=S stretching modes
561	S=S stretching mode
928	Stretching CH <sub>3</sub> N and C=S modes
1150	CN stretching mode and CH <sub>3</sub>
1386	CN stretching mode and symmetric CH <sub>3</sub> deformation
1440	CH <sub>3</sub>
1515	CN stretching mode and the deformation and CH <sub>3</sub>

**Table 5. 4** theoretical Band assignments of major peaks in Raman spectra of Thiram

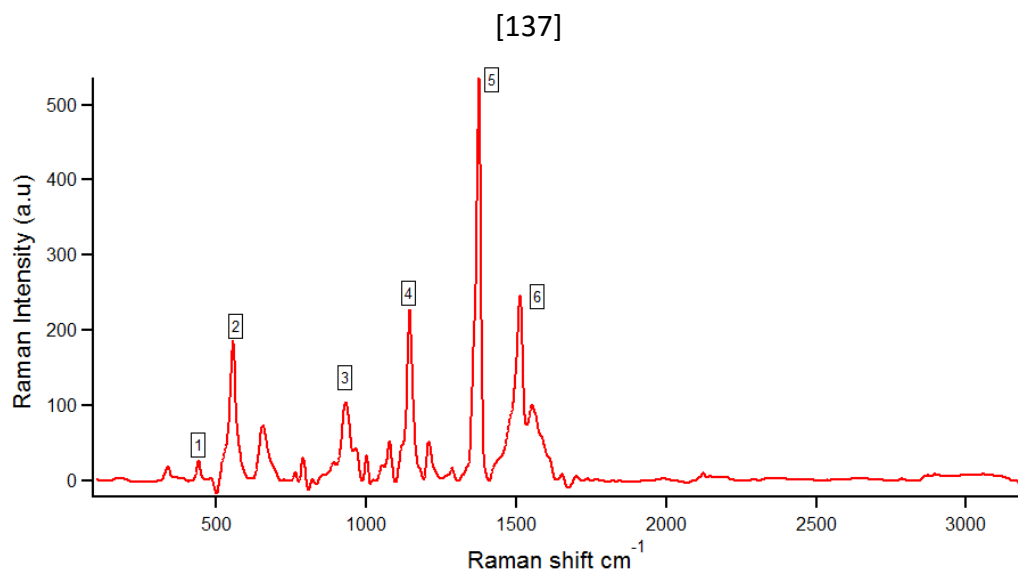


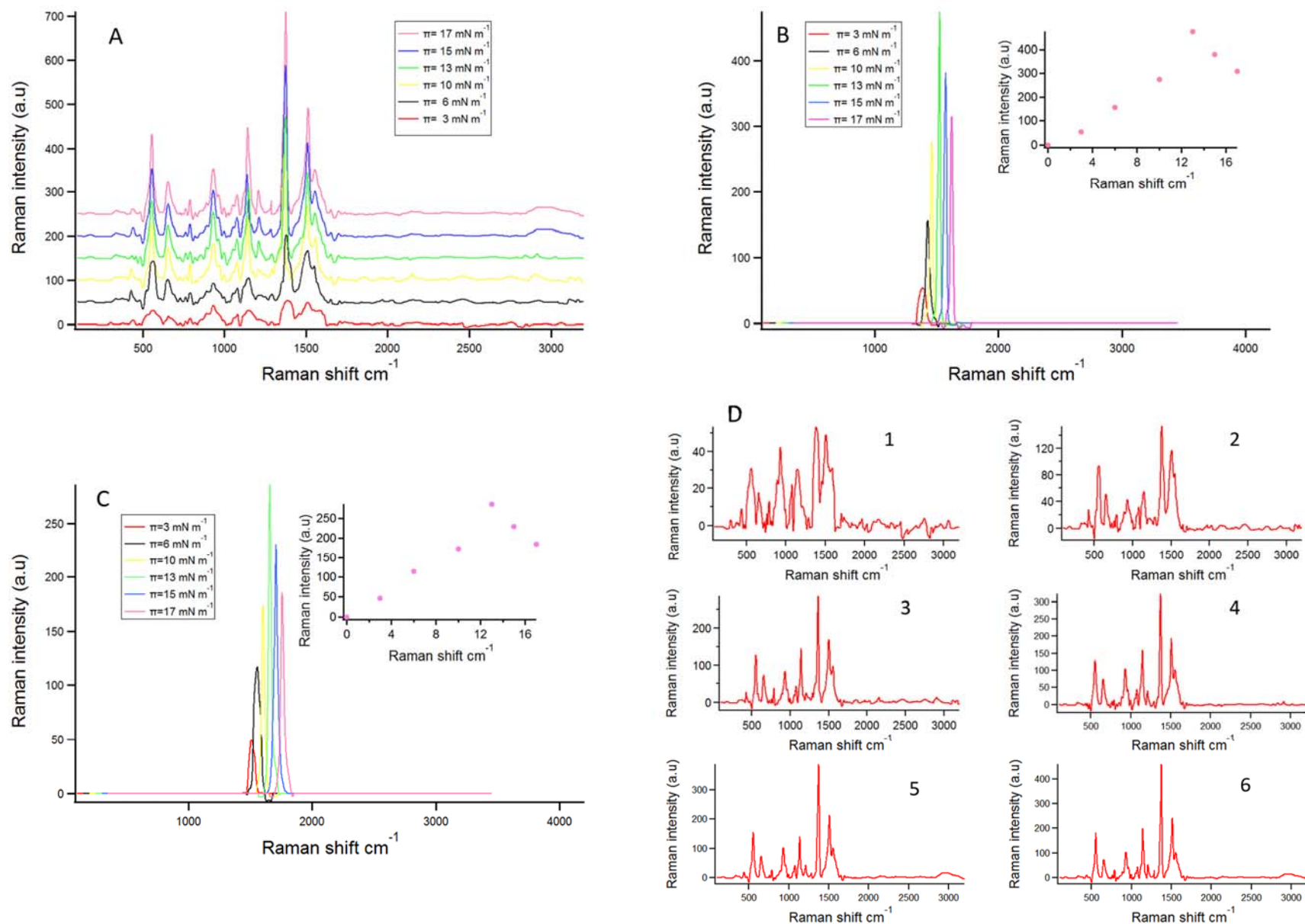
**Fig. 5. 1** SERS spectra of 5  $\mu\text{M}$  Thiram solution on fused silica substrate with a 10 nm gold nanoparticle monolayer prepared at a surface pressure of 13  $\text{mNm}^{-1}$  and 8 min electroplating time numbers 1 to 6 are respectively related to 442, 561, 930, 1148, 1386 and 1515  $\text{cm}^{-1}$

Aiming to investigate the effect of gold particle lattice density on SERS signals, the first phase of contaminant analysis was performed by deposition of Thiram on fused silica substrates prepared with particle monolayers at different lateral

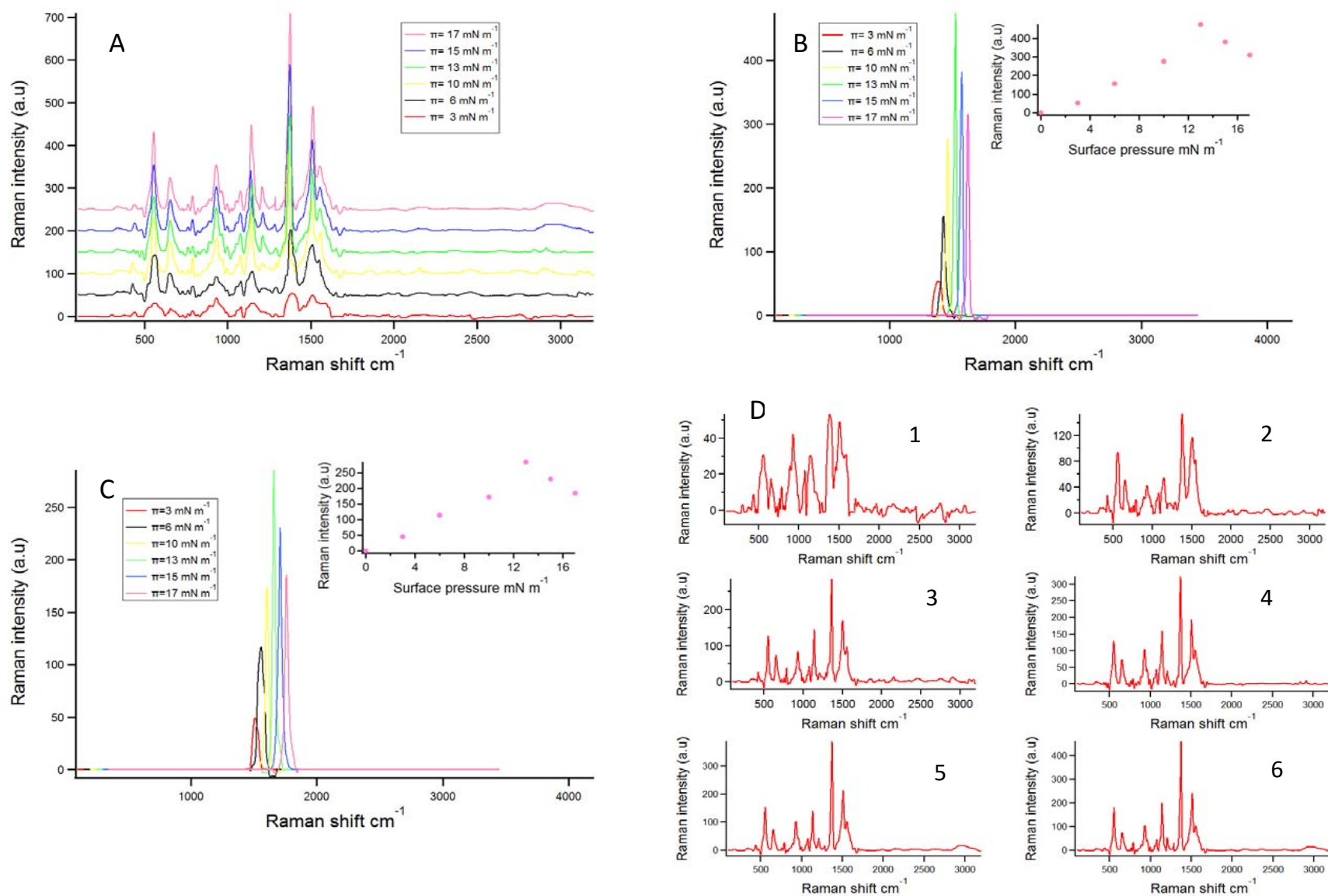
pressures. A common gold electroless plating time of 8 min has been applied to all NP monolayers. Experimental conditions of SERS are 3-accumulation, 30 s exposure time and 1% of laser power.

*Fig. 5.2 to 5.6* show a family of SERS spectra obtained from Thiram adsorbed on gold nanoparticle substrates. In *Fig. 5.2 and 5.3*, we find SERS spectra of Thiram adsorbed on 10 nm gold nanoparticle monolayer respectively from 5 and 1  $\mu\text{M}$  solution. Part a) displayed with an offset in the Y axis to make the peaks visible. In part b) and c) we focused on the two well-known main peaks for Thiram at 1380  $\text{cm}^{-1}$  and 1515  $\text{cm}^{-1}$ , while we filter the rest of the spectrum using bandpass filters. The SERS intensity of Thiram peaks are improved monotonically as the surface pressure increases from 3  $\text{mN m}^{-1}$  up to 13  $\text{mN m}^{-1}$ . The highest peak in these samples was obtained at a lateral pressure of 13  $\text{mN m}^{-1}$ . The density of gold particles per area plays an important role in the amplification of signals. For lateral pressures higher than 13  $\text{mN m}^{-1}$  the intensity of the peaks decreases which could be related to the monolayer collapse and gold particles aggregating on the surface. The LSPR effect becomes weaker when particles are deposited too far or too close from each other. Upon NP aggregation, the surface becomes less homogeneous as we have a part of the surface with a higher amount of aggregated particles and the rest of the surface is covered with a NP monolayer. The LSPR effect in hotspot which are made up of aggregated particles is weaker in comparison with smaller or separated hotspots. The other reason of weak SERS peaks in the aggregated hotspots is a lower surface to volume ratio. Aggregated particles on the surface have higher surface area, which increases the absorption of molecules. SERS peaks of 5  $\mu\text{M}$  Thiram solution are more intense in comparison with the peaks of 1  $\mu\text{M}$  solution, but less than 5 times. See below for an analysis of the kinetics of adsorption and the adsorption isotherm.

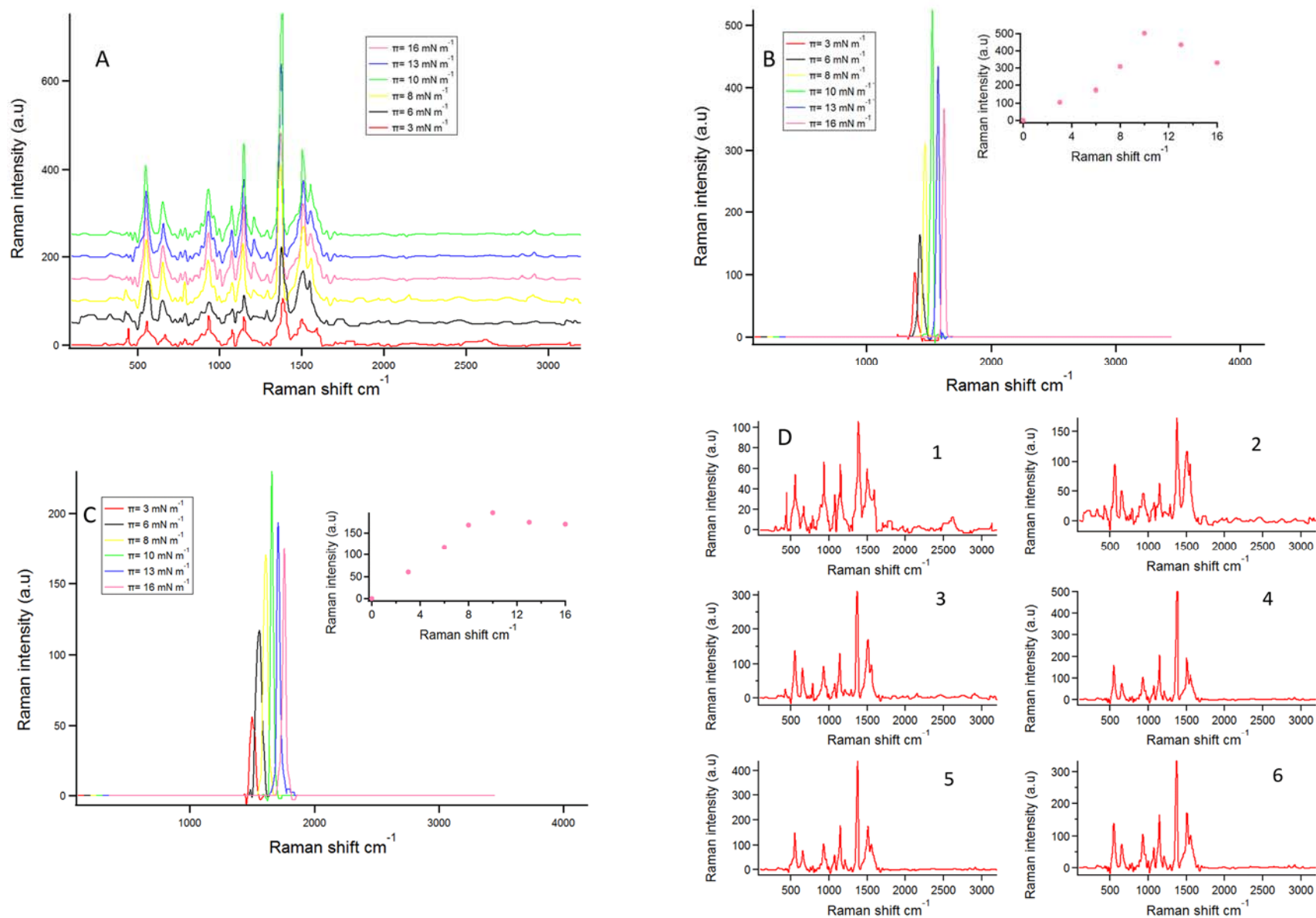
In the next step of this study we used nano-stars (urchin-shaped gold nanoparticles) to perform SERS experiments (*Fig 5 and 6*). After performing test with nano-stars for measuring 4-MBA (sec 4.4.3) we used them for SERS measurement of Thiram and Carbaryl molecules. Substrates were prepared at different lateral pressures, 3, 6, 8, 10, 13, 16 and 17  $\text{mN m}^{-1}$ . SERS data show that there is an increase in both peaks at 1380  $\text{cm}^{-1}$  and 1515  $\text{cm}^{-1}$  from 3 to 10  $\text{mN m}^{-1}$  and the highest peaks are observed at a lateral pressure 10  $\text{mN m}^{-1}$ . The results with Thiram agree with our data for 4-MBA as we also reached the highest peak for 10  $\text{mN m}^{-1}$  lateral pressure.



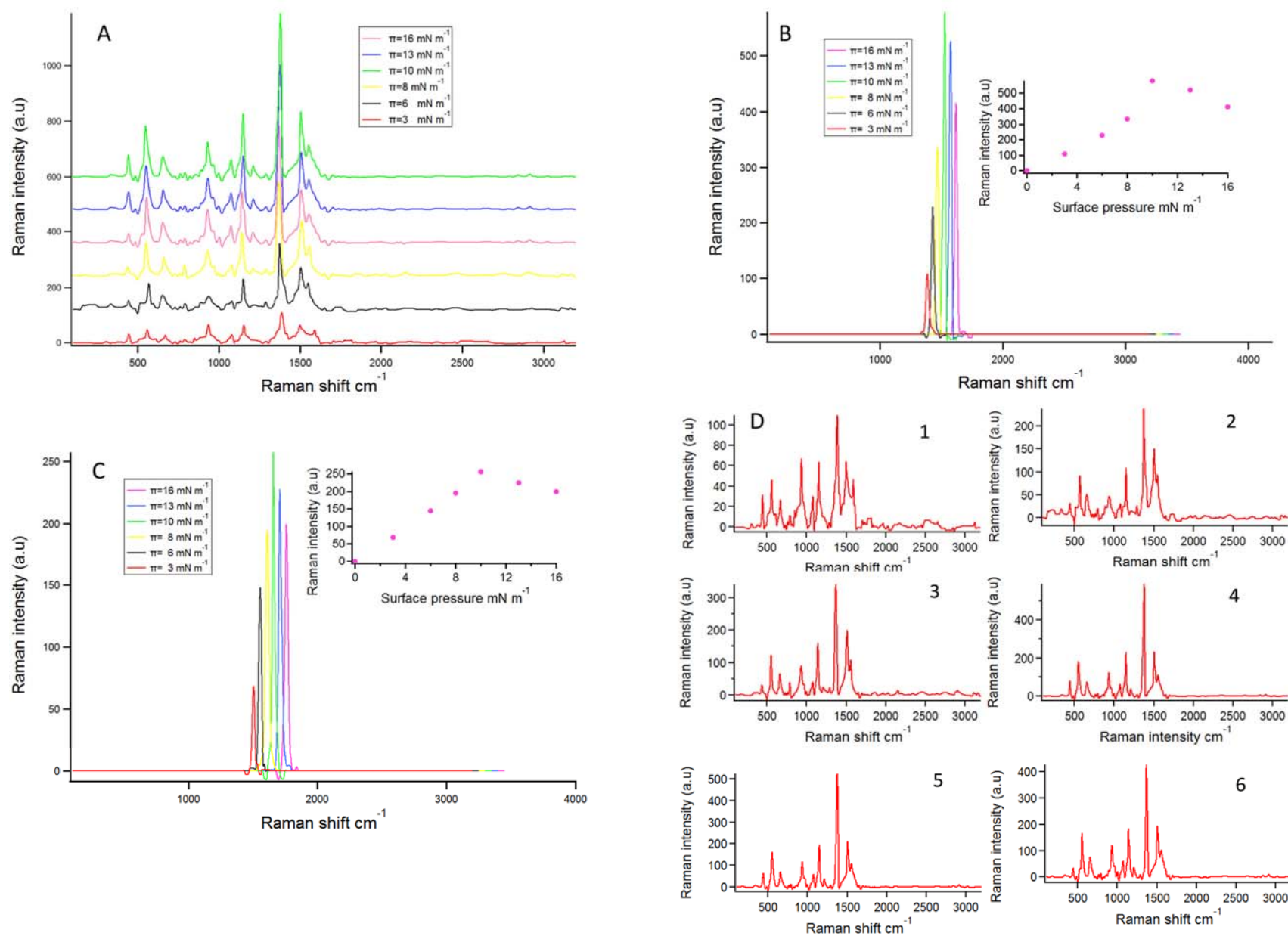
**FIG. 5. 2** A) SERS spectra of Thiram adsorbed on 10 nm gold nanoparticle monolayers from 1  $\mu$ M solution. Monolayers are transferred from the aqueous interface to solid substrates at different lateral pressures (17, 15, 13, 10, 6 and 3 mN m<sup>-1</sup>) followed by an electroplating time of 8 min. Intensities have been manually shifted to avoid spectra overlap. B) Height of the SERS peaks at 1386 cm<sup>-1</sup> C) Height of the SERS peaks at 1515 cm<sup>-1</sup> at different surface pressures. D) Separated SERS spectra of Thiram (1, 2, 3, 4, 5, 6 are respectively related to 3, 6, 10, 13, 15 and 17 mN m<sup>-1</sup> lateral pressure).



**FIG. 5. 3** A) SERS spectra of Thiram adsorbed on 10 nm gold nanoparticle monolayers from  $5 \mu\text{M}$  solution. Monolayers are transferred from the aqueous interface to solid substrates at different lateral pressures ( $17, 15, 13, 10, 6$  and  $3 \text{ mN m}^{-1}$ ) followed by an electroplating time of 8 min. Intensities have been manually shifted to avoid spectra overlap B) Height of the SERS peak at  $1386 \text{ cm}^{-1}$  C) Height of the SERS peak at  $1515 \text{ cm}^{-1}$  at different surface pressures. D) Separated SERS spectra of Thiram (1, 2, 3, 4, 5, 6 are respectively related to 3, 6, 10, 13, 15 and  $17 \text{ mN m}^{-1}$ ).



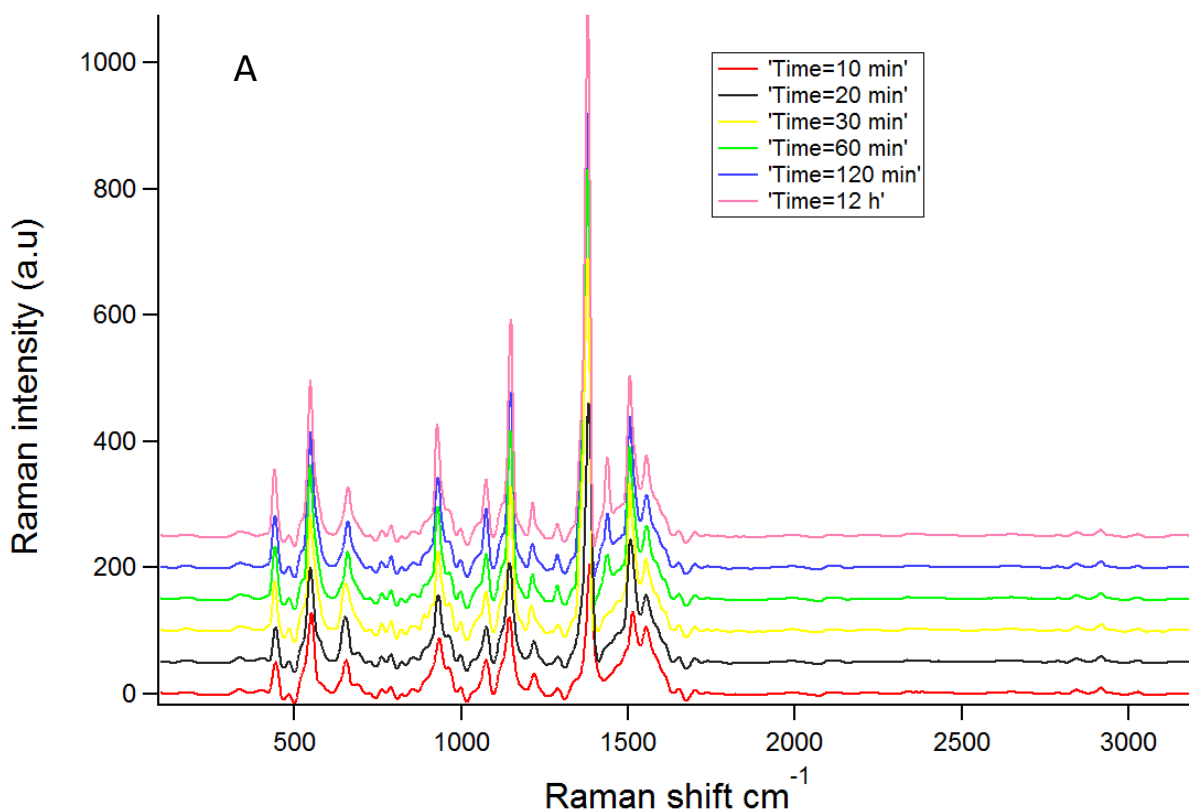
**FIG. 5.** 4 A) SERS spectra of Thiram adsorbed on Nanostar gold nanoparticle monolayers from a  $1 \mu\text{M}$  solution. Monolayers are transferred from the aqueous interface to the solid substrate at different lateral pressures ( $3, 6, 8, 10, 13$  and  $16 \text{ mN m}^{-1}$ ) followed by an electroplating time of  $8 \text{ min}$ . Intensities have been manually shifted to avoid spectra overlap B) Height of the SERS peak at  $1386 \text{ cm}^{-1}$  C) Height of the SERS peak at  $1515 \text{ cm}^{-1}$  at different surface pressures. D) Separated SERS spectra of Thiram (1, 2, 3, 4, 5, 6 are respectively related to  $3, 6, 8, 10, 13$  and  $16 \text{ mN m}^{-1}$ ).

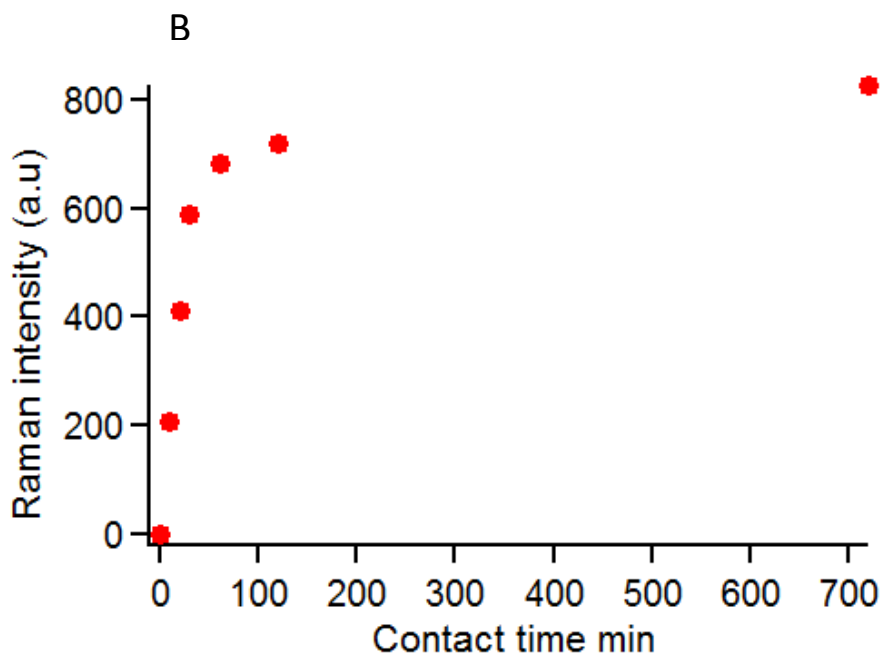


**FIG. 5.** A) SERS spectra of Thiram adsorbed on Nanostar gold nanoparticle monolayers from 5  $\mu\text{M}$  solution. Monolayers are transferred from the aqueous interface to the solid substrates at different lateral pressures (3, 6, 8, 10, 13 and 16  $\text{mN m}^{-1}$ ) followed by an electroplating time of 8 min. Intensities have been manually shifted to avoid spectra overlap. B) Height of the SERS peak at 1386  $\text{cm}^{-1}$  C) Height of the SERS peak at 1515  $\text{cm}^{-1}$  at different surface pressures. D) Separated SERS spectra of Thiram (1, 2, 3, 4, 5, 6 are respectively related to 3, 6, 8, 10, 13 and 16  $\text{mN m}^{-1}$ ).

### 5.4.1.2 Effect of contact time on Thiram adsorption on substrate

We tested the effect on the SERS spectra of the contact time with Thiram solutions with the substrates. In this part we used gold nanostars and 5  $\mu\text{M}$  aqueous Thiram solution. Samples were prepared at 10  $\text{mN m}^{-1}$ , which is the optimal lateral pressure as reported above. Solid samples were immersed in the Thiram solution for 10, 20, 30, 60, 120 min and 12h and let the samples to dry. Our goal in this section was to measure the kinetics of adsorption of Thiram on the gold particle surface. The highest peaks in the spectra correspond to 12h contact time. There is an uptrend in SERS spectra from 10 min to 12h contact time. If we assume that the peak intensity is proportional to the surface coverage by Thiram molecules, around 80% of surface saturation occurs within 30 minutes of contact time *Fig 5. 6*.

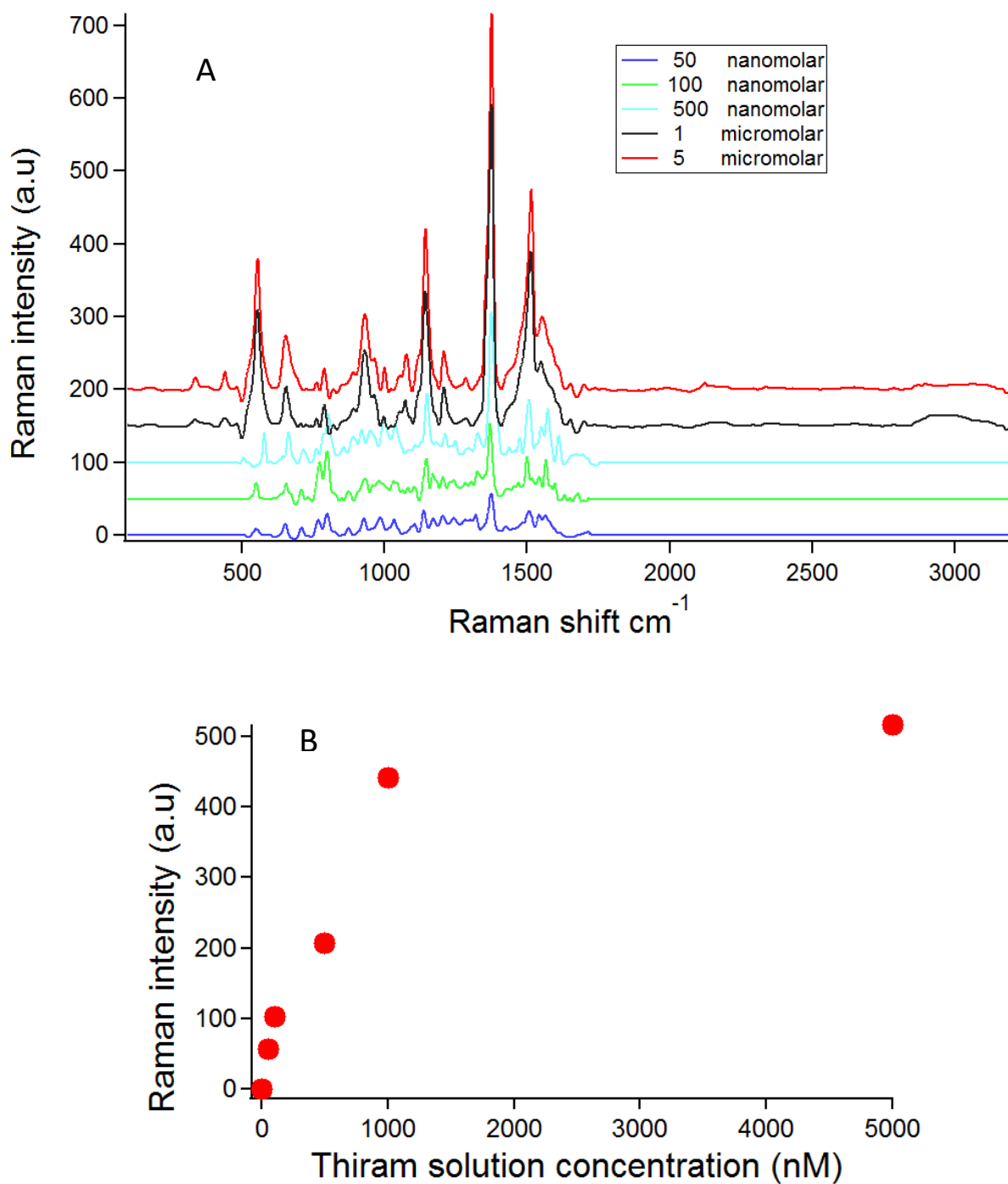




**Fig. 5. 6** A) SERS spectra of Thiram adsorbed on gold Nanostar monolayers from 5  $\mu\text{M}$  solution. Prepared substrates were submerged in Thiram solutions for different contact times (10, 20, 30, 60, 120 min and 12 h). B) Height of the SERS peak at 1386  $\text{cm}^{-1}$  as a function of adsorption time

#### ***5.4.1.3 Effect of Thiram solution concentration on SERS measurements***

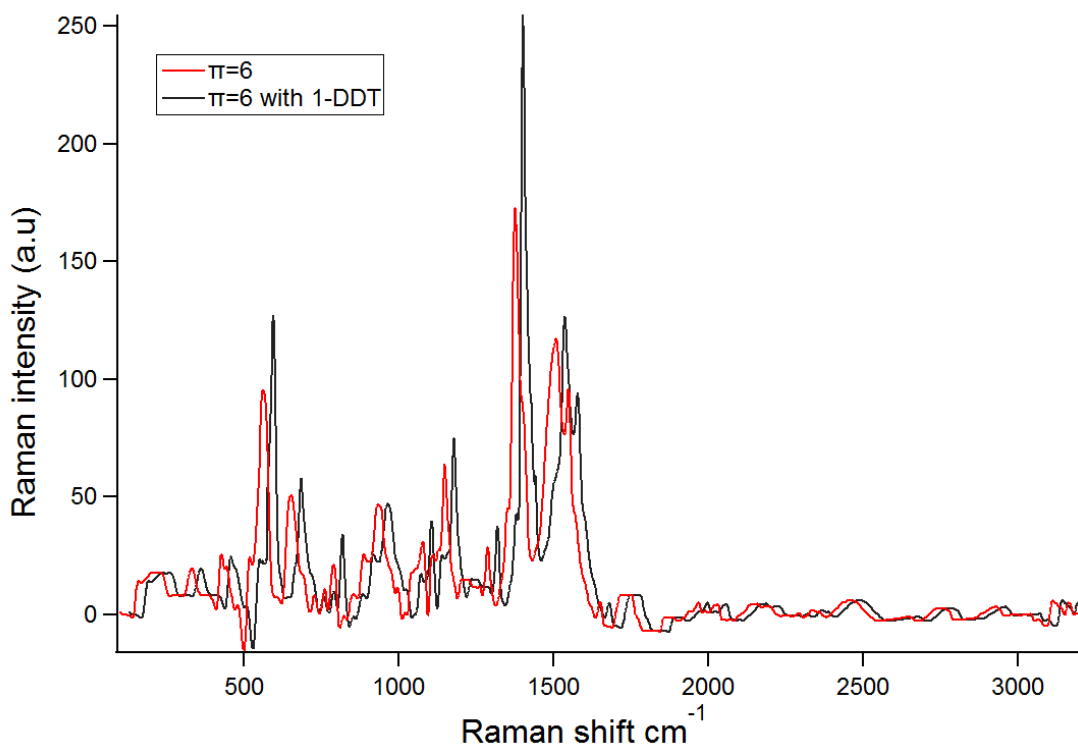
In order to study the effect of Thiram concentration on SERS measurements and study the limit of detection, we prepared several aqueous solutions of Thiram (50, 100, 500, 1000 and 5000 nanomolar). For preparing substrates in this stage we used 10 nm spherical gold nanoparticles and 13  $\text{mN m}^{-1}$  surface pressure and Thiram adsorption was allowed to equilibrate for 30 min. At 50 and 100 nanomolar, Thiram peaks were weakly detected, but at higher concentrations, such as 500 nM and 1 and 5 micromolar, we have clear peaks. The intensity of peaks at 1386  $\text{cm}^{-1}$  are shown in *Fig. 5.7*, part B. It increases monotonically up to the 5  $\mu\text{M}$  solution, where it seems to be close to saturation. With our proposed method of SERS substrate fabrication, we could confidently detect Thiram in solutions with concentrations higher than 50 nanomolar.



**Fig. 5.** 7 A) SERS spectra of Thiram adsorbed on 10 nm gold nanoparticle monolayers prepared at  $13 \text{ mN m}^{-1}$  surface pressure. Adsorption was studied for 50, 100, 500 nanomolar and 1, 5 micromolar aqueous solutions. B) Height of the SERS peak at  $1386 \text{ cm}^{-1}$

#### 5.4.1.4 Effect of 1-DDT functionalization on the performance of SERS substrates

Thiol-ligand exchange on Au NPs surfaces plays a crucial role for particle reactivity [138]. Thiol-ligand on gold nanoparticles act as a Raman receptor and enhances SERS measurements [139]. In this section, the prepared solid substrates were treated with a solution of 1-DDT in chloroform to functionalize gold particle surfaces (*chapter 2*). We wanted to study the effect of 1-DDT molecules as receptors of pollutants, at the surface of gold particles. The main goal was to reach the highest adsorption levels of pollutant molecules at the gold surface and obtain robust and intense peak in SERS graphs. Substrates were prepared by using nano-star gold particles at 6 and 10 mN m<sup>-1</sup> lateral pressures. We used 1  $\mu$ M Thiram solution for substrate incubation for 30 min. We see in *Fig. 5.8* that the peaks of Thiram SERS spectra were enhanced upon substrate functionalized with 1-DDT. Different molecules could bind to the free -CH<sub>3</sub> terminal group of dodecanethiol and perform a stable structure. There is a remarkable increase in the peak intensity at 1386 cm<sup>-1</sup>, from 173 to 255 a.u. and from 503 to 760 a.u. respectively for 6 and 10 mN m<sup>-1</sup> surface pressure. In both cases, the increase is around 50%.



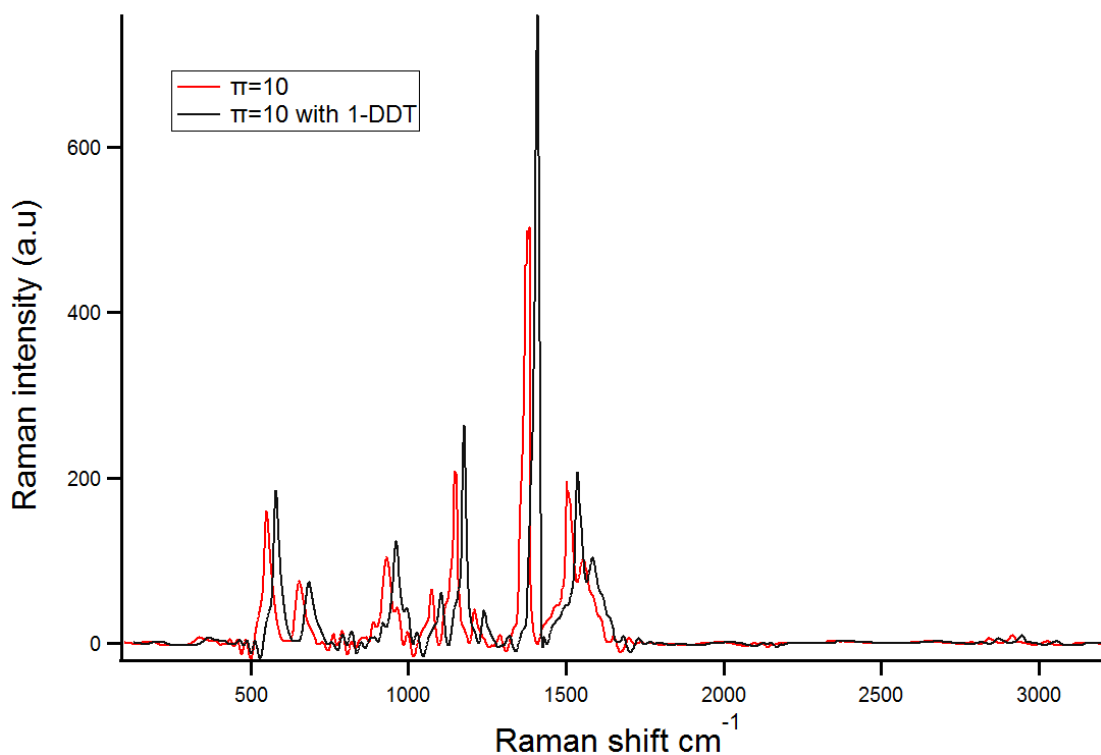


**Fig. 5. 8** SERS spectra of Thiram adsorbed on nanostar gold nanoparticle monolayers from 1  $\mu\text{M}$  solution. Solid substrates were prepared under 6 and 10  $\text{mN m}^{-1}$  as surface pressure. Substrates were functionalized with 1-DDT prior to Thiram adsorption, and compared with simple substrates without 1-DDT. We perform a shift in graph of 1-DDT for eye comfort

### 5.4.2 Carbaryl detection

In the second step of analyzing the SERS spectra of pollutants, we used Carbaryl molecules. 1 and 5  $\mu\text{M}$  solutions were used in this study. SERS substrates were fabricated from 10 nm gold nanoparticles and gold nanostars at 3, 6, 8, 10, 13, 15, 16 and 17  $\text{mNm}^{-1}$  surface pressure. Samples were electroplated with gold for 8 min. 100 microliter of 1 or 5  $\mu\text{M}$  Carbaryl solution was deposited on the substrates and we waited for 30 min until solvent evaporation. Carbaryl has several SERS peaks that can be used to identify this organic pollutant. SERS peaks of Carbaryl molecules are observed at 453, 723, 930, 1374, 1432, 1576 and 1704  $\text{cm}^{-1}$  [140].

We found 6 main peaks in our SERS measurement of Carbaryl, and these peaks are numbered from 1 to 6 in Fig. 5. 9 that are respectively observed at 453, 723,

930, 1374, 1432 and 1576  $\text{cm}^{-1}$ . In our samples we did not recognize a remarkable peak at the 1704  $\text{cm}^{-1}$ .

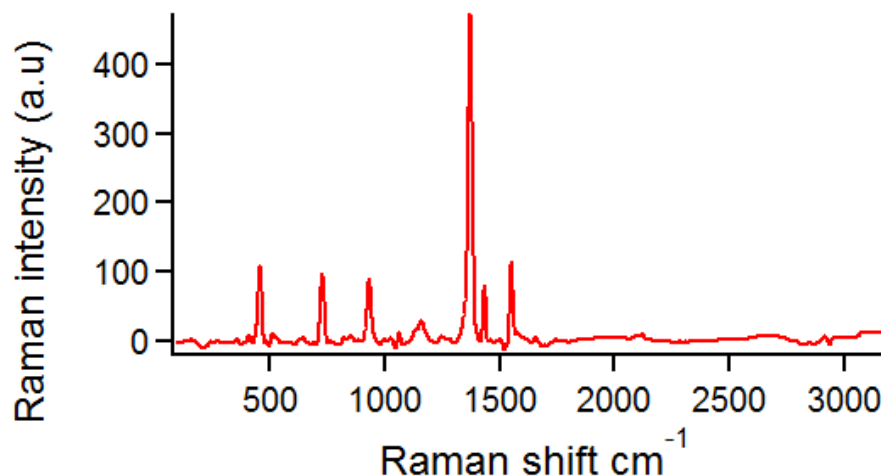


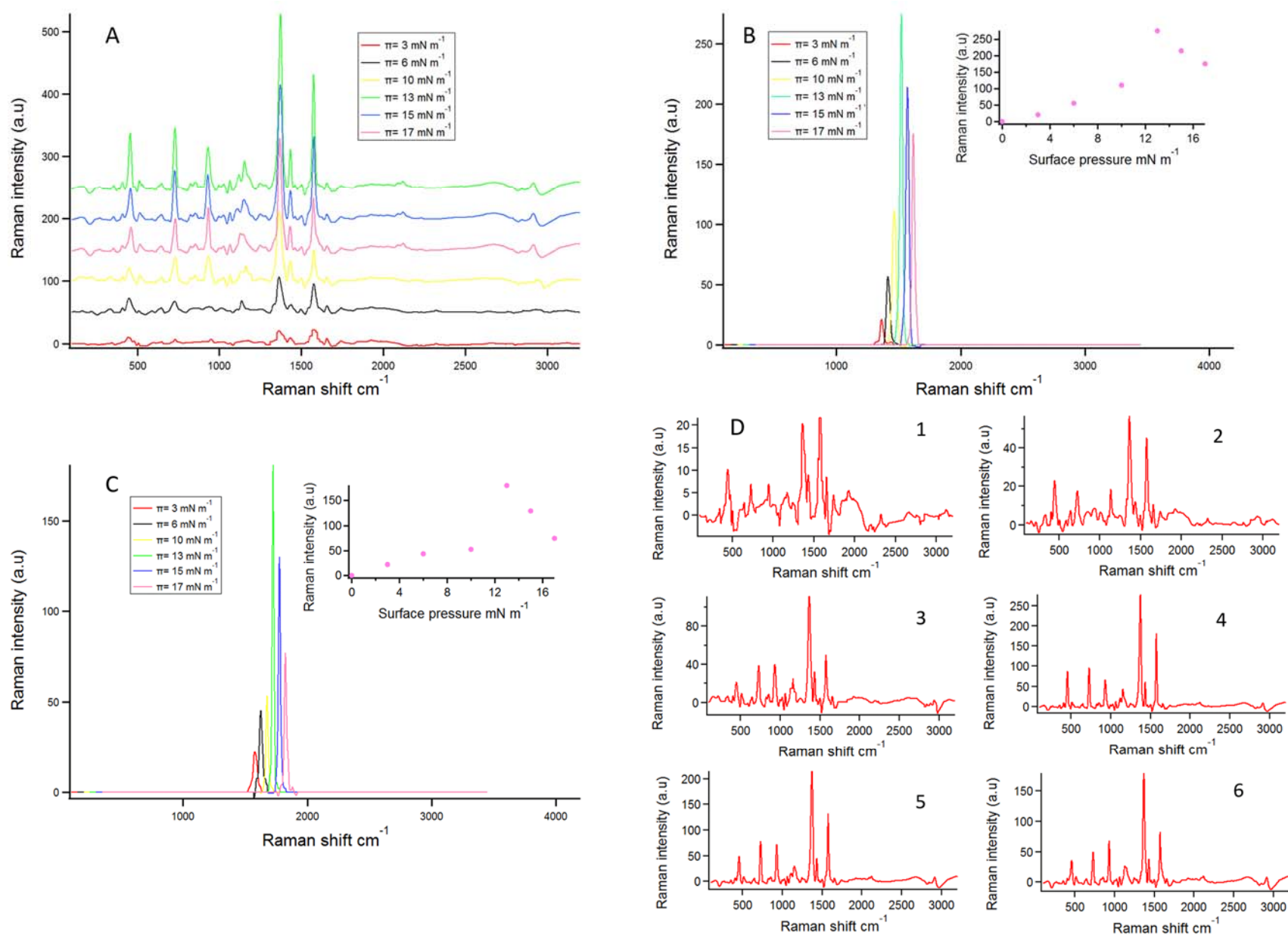
**Fig. 5. 9** SERS spectra of 5  $\mu\text{M}$  Carbaryl solution on fused silica substrates with 10 nm gold NP prepared at 13  $\text{mNm}^{-1}$  surface pressure and 8 min electroplating time

In *Fig. 5.9*, peak number 4 is the most intense at 1374  $\text{cm}^{-1}$ . In the following reported data, we masked and analyzed peaks at 1374 and 1576  $\text{cm}^{-1}$  using the program Labspec. Peaks at 1374 and 1576  $\text{cm}^{-1}$  are related to C-C, C-N and CN stretching mode and the deformation of  $\text{CH}_3$  bond.

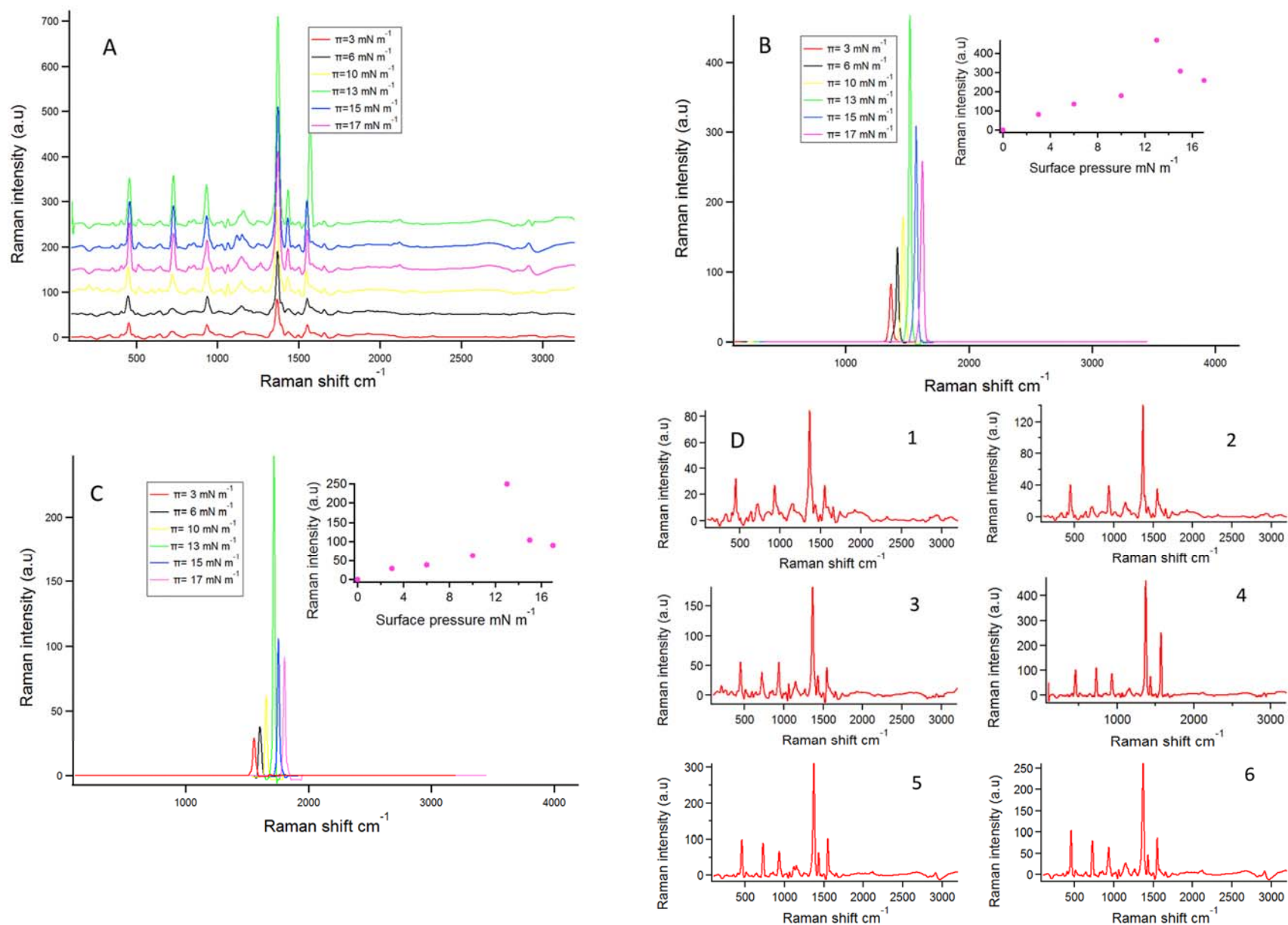
#### **5.4.2.1 Effect of surface pressure**

Monolayers of both 10 nm and urchin shape gold nanoparticles were prepared at the water/air interface in several lateral pressures (3, 6, 8, 10, 13, 15, 16 and 17  $\text{mN m}^{-1}$ ) and transferred to the silica surface. All substrates were subsequently electroplated with gold for 8 min. SERS spectra and peaks of Carbaryl become more intense and more robust by increasing lateral pressures from 3 to 13  $\text{mN m}^{-1}$  and 3 to 10  $\text{mN m}^{-1}$  respectively for 10 nm gold particles and gold nano-star particles. For higher surface pressures there is a remarkable decrease in spectra intensity (*Fig. 5. 10* to *5. 14*). We mask the peak at 1374 and 1576  $\text{cm}^{-1}$  in part B and C of the figures. The highest intensity of peaks for 10 nm gold nanoparticles were equal to 472 (a.u) and were observed at 1374  $\text{cm}^{-1}$  (5  $\mu\text{M}$ ) whereas the highest intensity of peaks at 1374  $\text{cm}^{-1}$  for nanostars was equal to 530 (a.u). Also in 1  $\mu\text{M}$  solution the high intensity of peaks for 10 nm was observed in 13  $\text{mN m}^{-1}$  and 10  $\text{mN m}^{-1}$  respectively for 10 nm gold particles and gold nano-

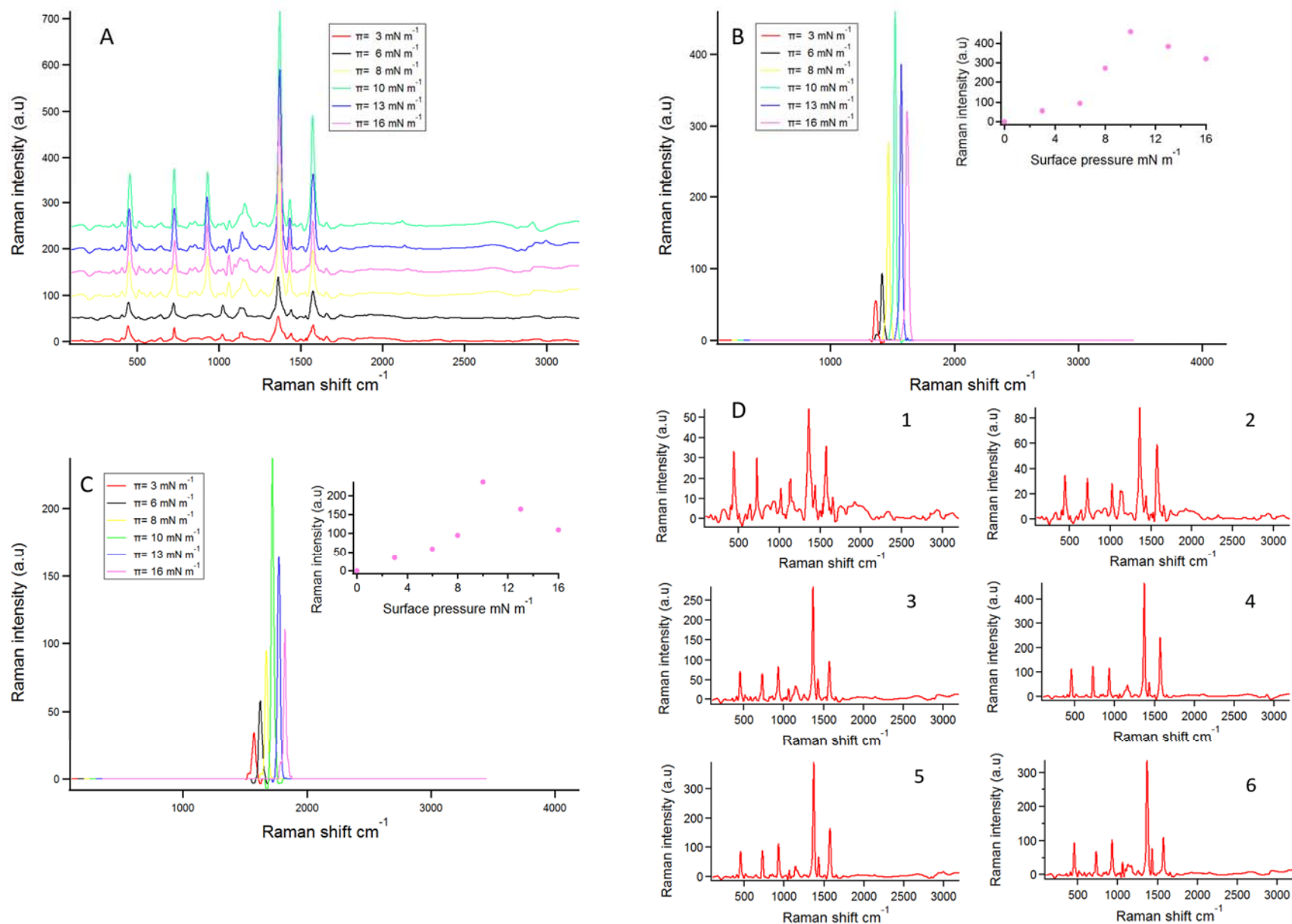
star particles. Due to the result of SERS, we observed substantial change at the peak of  $1374\text{ cm}^{-1}$  and  $1576\text{ cm}^{-1}$  by increasing the Carbaryl concentration from 1 to  $5\text{ }\mu\text{M}$ .



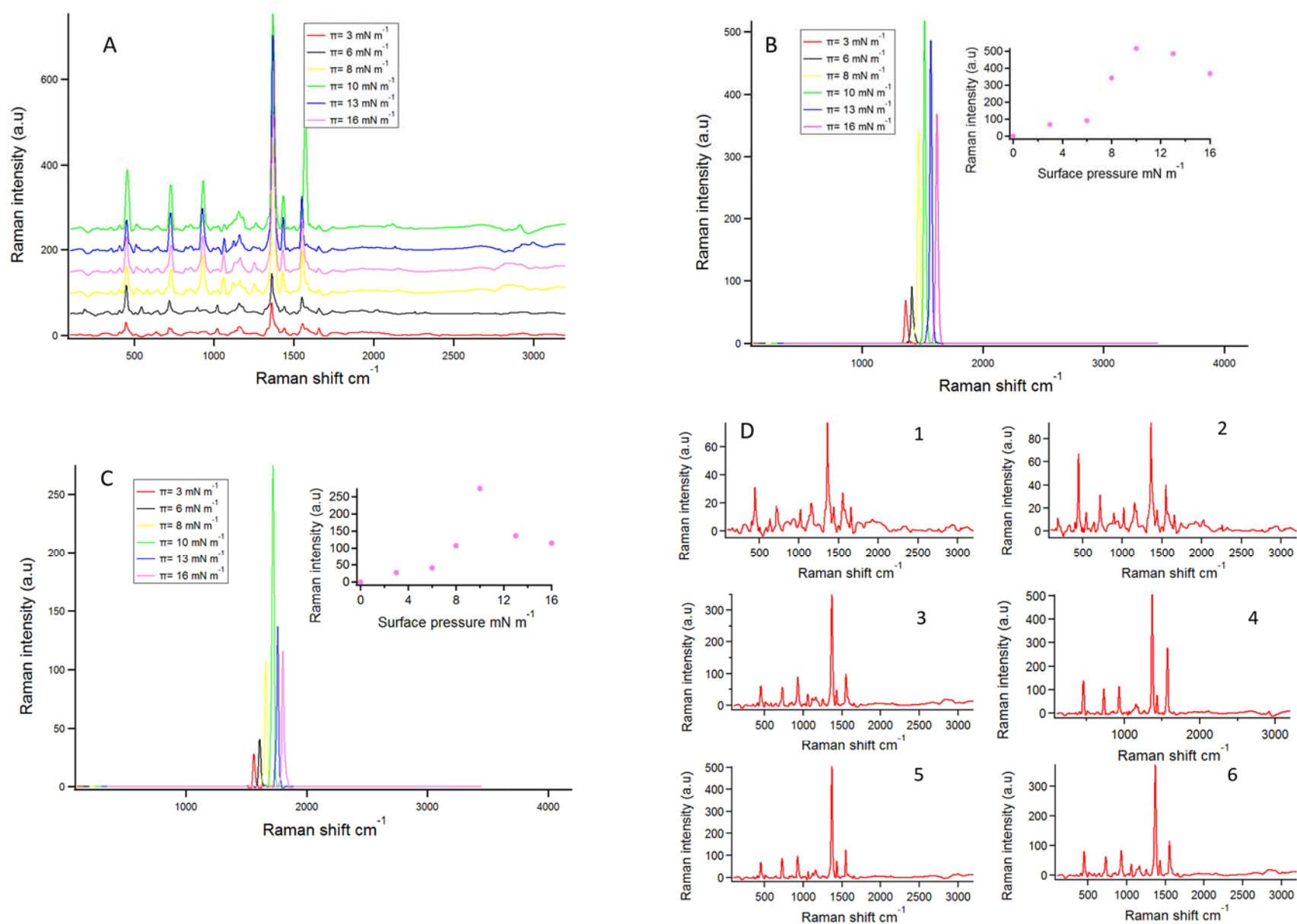
**FIG. 5.10** A) SERS spectra of Carbaryl adsorbed on 10 nm gold nanoparticle monolayers from 1  $\mu\text{M}$  solution. Monolayers are transferred from the aqueous interface to solid substrates at different lateral pressures (3, 6, 10, 13, 15 and 17  $\text{mN m}^{-1}$ ) followed by an electroplating time of 8 min. Intensities have been manually shifted to avoid spectra overlap. B) Height of the SERS peak at 1374  $\text{cm}^{-1}$  C) Height of the SERS peak at 1576  $\text{cm}^{-1}$  at different surface pressures. D) Separated SERS spectra of Carbaryl (1, 2, 3, 4, 5, 6 are respectively related to 3, 6, 10, 13, 15 and 17  $\text{mN m}^{-1}$ ).



**FIG. 5.11** A) SERS spectra of Carbaryl adsorbed on 10 nm gold nanoparticle monolayers from a 5  $\mu\text{M}$  solution. Monolayers are transferred from the aqueous interface to solid substrates at different lateral pressures (3, 6, 10, 13, 15 and 17  $\text{mN m}^{-1}$ ) followed by an electroplating time of 8 min. Intensities have been manually shifted to avoid spectra overlap. B) Height of the SERS peak at 1374  $\text{cm}^{-1}$ . C) Height of the SERS peak at 1576  $\text{cm}^{-1}$  at different surface pressures. D) Separated SERS spectra of Carbaryl (1, 2, 3, 4, 5, 6 are respectively related to 3, 6, 10, 13, 15 and 17  $\text{mN m}^{-1}$ ).



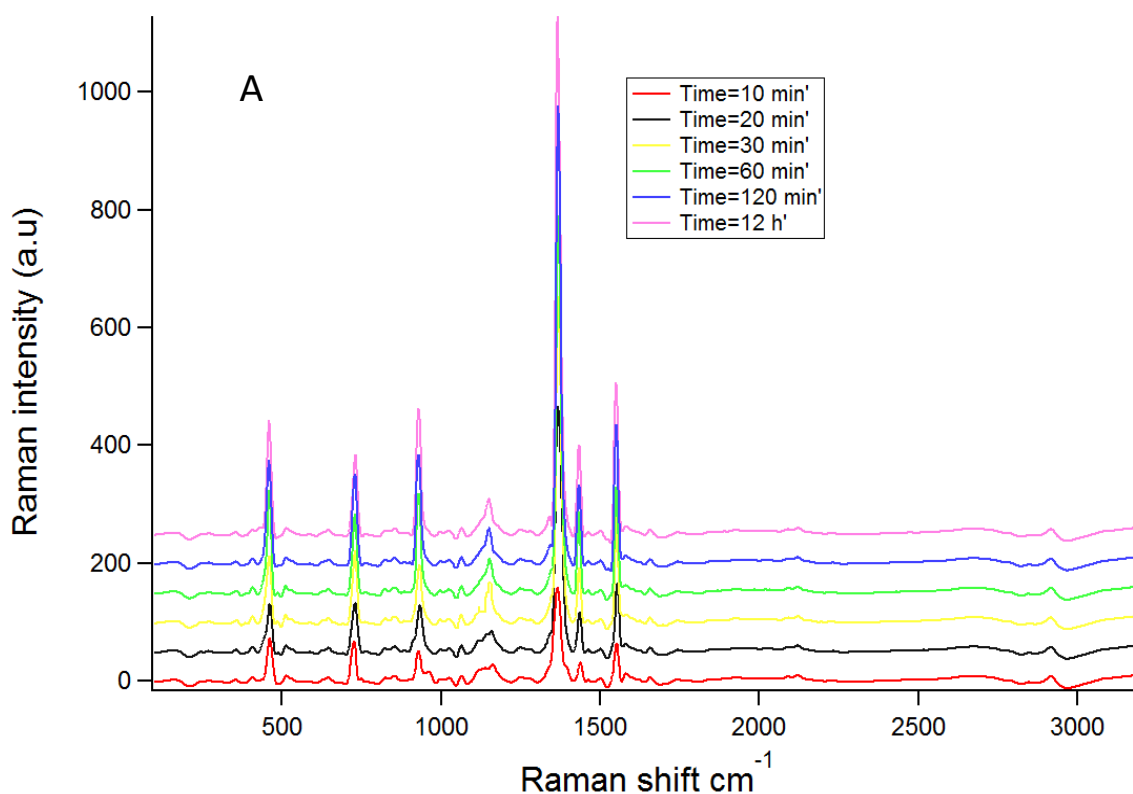
**FIG. 5.12** A) SERS spectra of Carbaryl adsorbed on Nanostar gold nanoparticle monolayers from a  $1 \mu\text{M}$  solution. Monolayers are transferred from the aqueous interface to the solid substrate at different lateral pressures ( $3, 6, 8, 10, 13$  and  $16 \text{ mN m}^{-1}$ ) followed by an electroplating time of  $8 \text{ min}$ . Intensities have been manually shifted to avoid spectra overlap. B) Height of the SERS peak at  $1374 \text{ cm}^{-1}$ . C) Height of the SERS peak at  $1576 \text{ cm}^{-1}$  at different surface pressures. D) Separated SERS spectra of Carbaryl (1, 2, 3, 4, 5, 6 are respectively related to  $3, 6, 8, 10, 13$  and  $16 \text{ mN m}^{-1}$ ).



**FIG. 5.13** A) SERS spectra of Carbaryl adsorbed on Nanostar gold nanoparticle monolayers from a  $5 \mu\text{M}$  solution. Monolayers are transferred from the aqueous interface to the solid substrates at different lateral pressures ( $3, 6, 8, 10, 13$  and  $16 \text{ mN m}^{-1}$ ) followed by an electroplating time of  $8 \text{ min}$ . Intensities have been manually shifted to avoid spectra overlap. B) Height of the SERS peak at  $1374 \text{ cm}^{-1}$  C) Height of the SERS peak at  $1576 \text{ cm}^{-1}$  at different surface pressures. D) Separated SERS spectra of Carbaryl (1, 2, 3, 4, 5, 6 are respectively related to  $3, 6, 8, 10, 13$  and  $16 \text{ mN m}^{-1}$ ).

### 5.4.2.2 Effect of contact time on Carbaryl adsorption on substrates

In order to study effect Carbaryl adsorption on SERS spectra, we prepared several samples with different contact time. 5  $\mu\text{M}$  Carbaryl solution is kept in contact with gold nanostar substrates prepared at 10  $\text{mN m}^{-1}$  surface pressure and following with 8 min of electroless plating. We used 10, 20, 30, 60, 120 min and 12 h as contact time. The main goal of this study was to study adsorption kinetic and find the optimal time, in order to achieve a certain SERS signal level. The trend of SERS peaks is similar to the graph of Thiram (sec 5.4.1.2). By increasing the contact time the adsorption of molecules increased dramatically and SERS peaks are increased monotonically. (Fig. 5.14). The most intense peaks are related to the samples of 12 h contact time, where equilibrium adsorption is nearly reached. Around 80% of Carbaryl saturation adsorption on the gold surface is reached after 30 min of incubation.



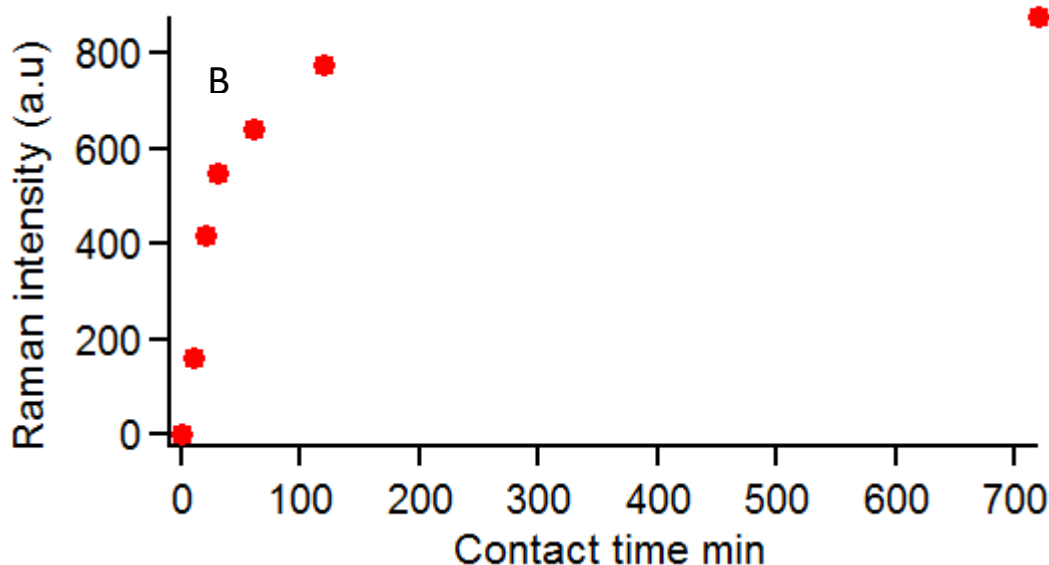


**Fig. 5. 14** A) SERS spectra of Carbaryl adsorbed on nanostar gold monolayers from 5  $\mu\text{M}$  solution. Prepared substrates were put into contact with Carbaryl solution for different times (10, 20, 30, 60, 120 min and 12 h). B) Height of the SERS peak at  $1374\text{ cm}^{-1}$

### ***5.4.2.3 Effect of Carbaryl solution concentration on SERS measurement***

We chose a range of Carbaryl aqueous solutions with different concentrations (50, 100, 500, 1000 and 5000 nanomolar) to study the effect of pollutant concentrations on SERS signals. 10 nm spherical gold nanoparticles were used for preparing substrate on fused silica. Gold monolayer was prepared at  $13\text{ mN m}^{-1}$  surface pressure following with 8 min of electroless plating. SERS substrates were immersed in Carbaryl solutions and were allowed to equilibrate for 30 min. in *sec 5.4.2.2* we mentioned above that around 80% of Carbaryl saturation adsorption on the gold surface is reached after 30 min of incubation. Carbaryl peaks of 50 and 100 nanomolar samples are very weak and, as mentioned in *sec 5.4.1.3*, we do not have clear peak as their intensity is within the noise level. At higher concentrations (500, 1000 and 5000 nanomolar) there are clear and peaks. Carbaryl SERS signals are shown in Fig. 5. 15 A. we plotted the height of the Carbaryl peak at  $1386\text{ cm}^{-1}$  in Fig. 5.15 B. In regards to the result of this part we could detect Carbaryl molecules from solutions with concentration higher than

100 nanomolar. In the other words, our limit of detection with the proposed method of substrate fabrication could be 100 nanomolar.

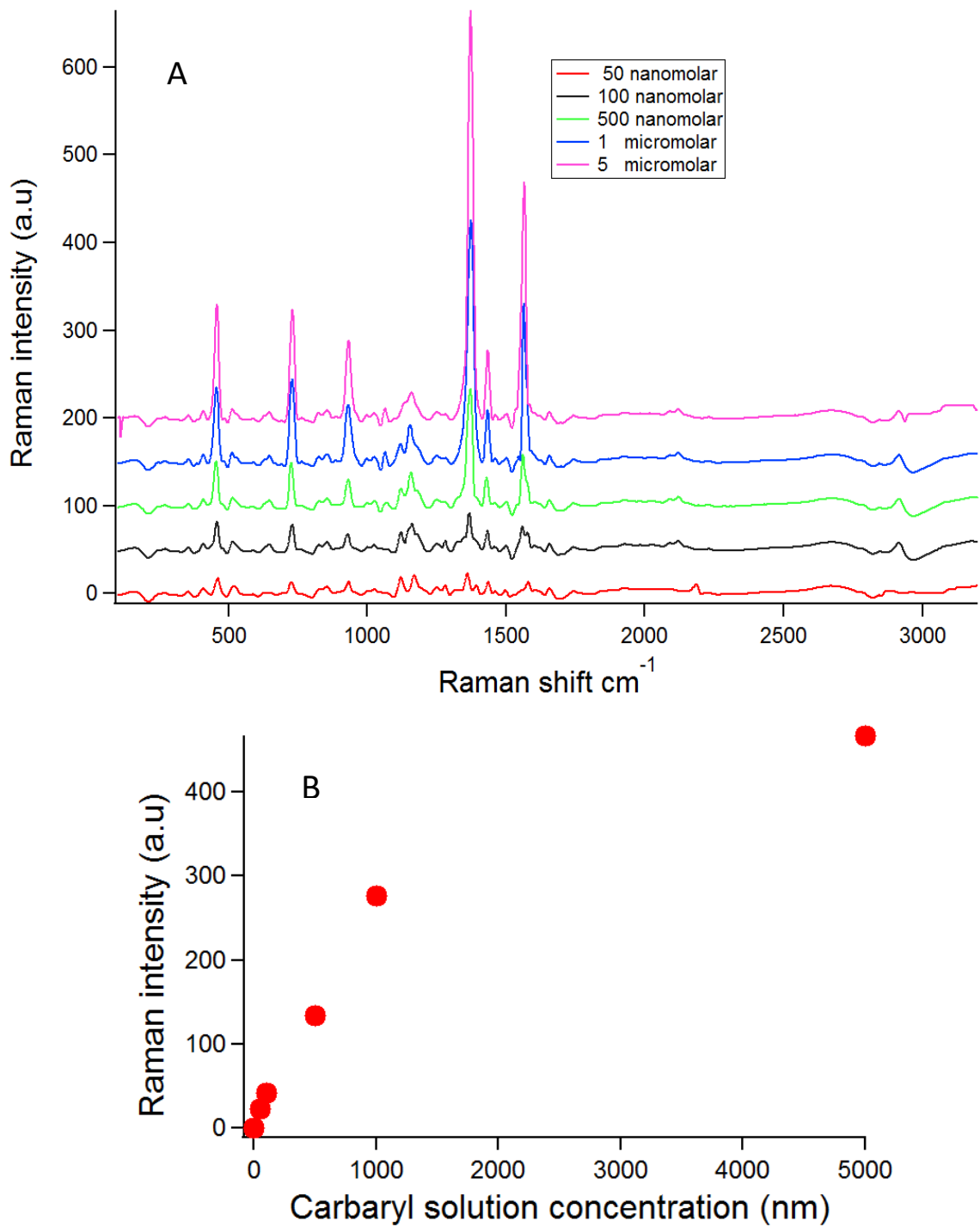
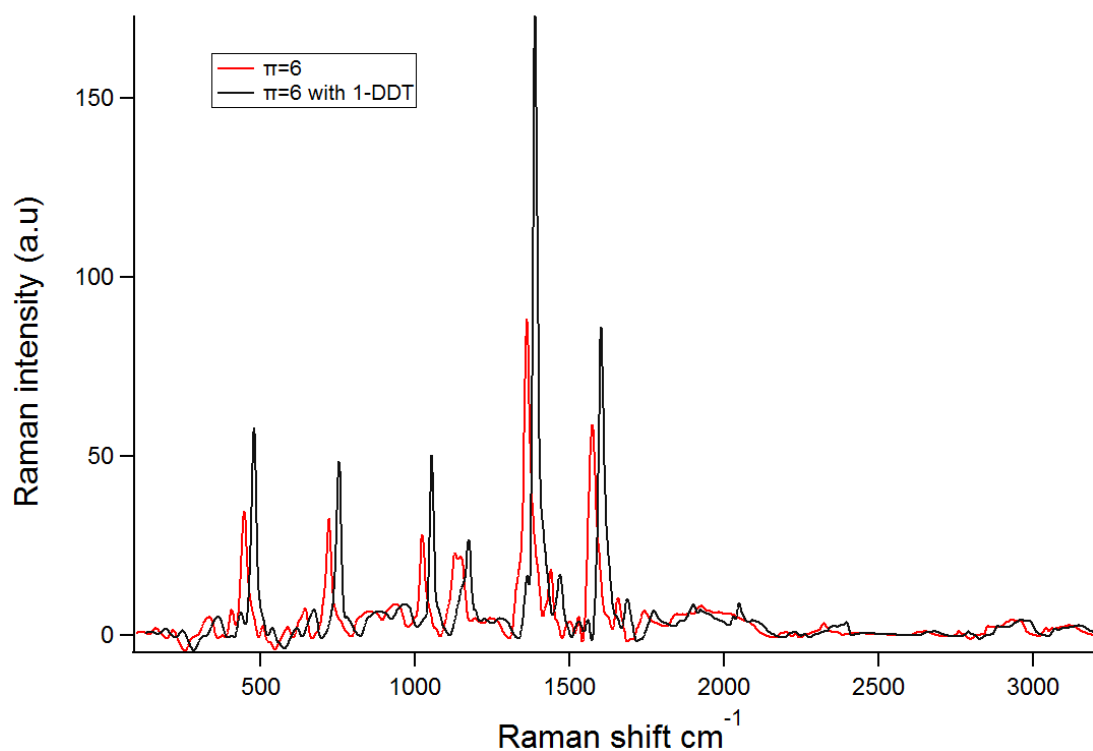


**Fig. 5. 15** A) SERS spectra of Carbaryl adsorbed on 10 nm gold nanoparticles monolayers prepared from 50, 100, 500 Nanomolar and 1, 5 Micromolar aqueous solutions and

10nm gold NP substrates prepared at  $13 \text{ mN m}^{-1}$  surface pressure, and electroplating time 8 min. B) Height of the SERS peak at  $1374 \text{ cm}^{-1}$ .

#### 5.4.2.4 Effect of 1-DDT functionalization on the performance of SERS substrate

In order to increase the adsorption rate of Carbaryl molecules on gold nanoparticles, we deposited 1-DDT molecules on SERS substrates. Thiol-ligands play an important role in SERS signal enhancement. The spatial form of  $-\text{CH}_3$  group in dodecanthiol molecules provide a proper place for attachment to the organic molecules such as Thiram and Carbaryl [139]. Prepared SERS substrates were functionalized with 1-DDT solution (sec 2), and immediately put into contact with Carbaryl solution with  $1 \mu\text{molar}$  concentration for 30 min, and subsequently SERS measurement were performed. SERS substrates were prepared at 6 and  $10 \text{ mN m}^{-1}$  surface pressures. SERS peaks are clear, enhanced and became more intense after substrate functionalization with 1-DDT (Fig. 5.16). In functionalized samples, intensity of the peak at  $1374 \text{ cm}^{-1}$  is increased from 88 to 170 (a.u) and from 467 to 596 (a.u), respectively for samples prepared under 6 and  $10 \text{ mN m}^{-1}$  surface pressure.



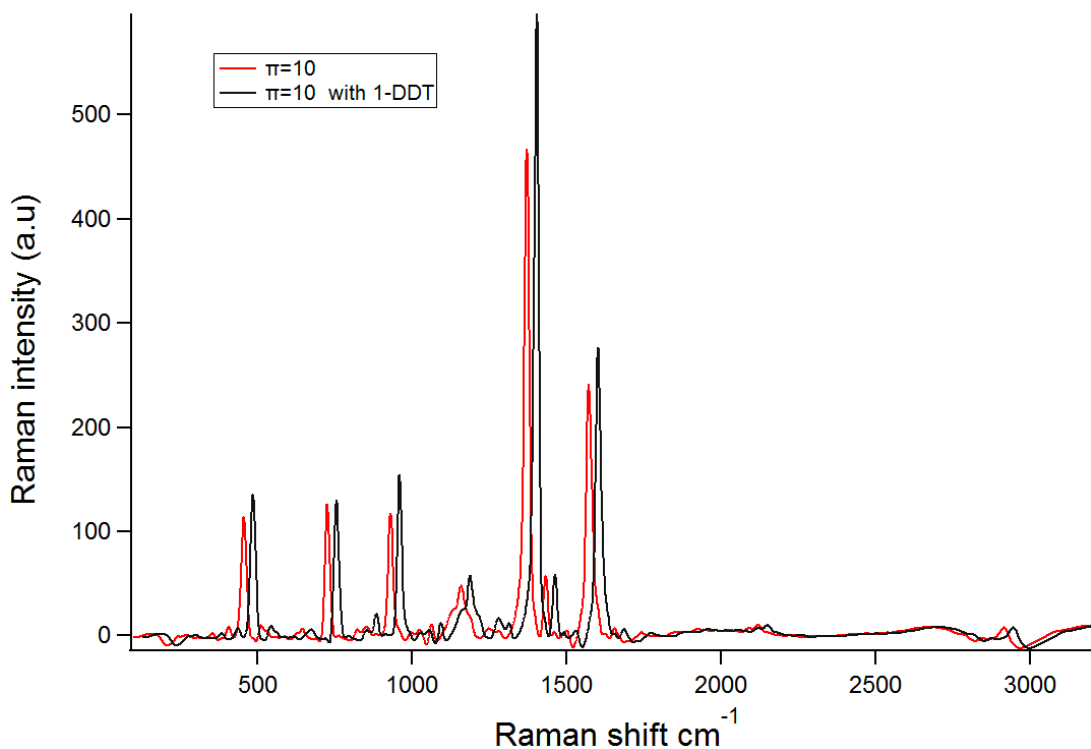


**Fig. 5. 16** SERS spectra of Carbaryl adsorbed on Nanostar gold monolayers from a 1  $\mu\text{M}$  solution. Solid substrates were prepared at 6 and 10  $\text{mN m}^{-1}$  as surface pressure. For each surface pressure, substrates were functionalized with 1-DDT and compares with substrates without 1-DDT

## 5. 5 Conclusions

In this chapter, the SERS signals of two water pollutants (Carbaryl and Thiram) were investigated. All measurements were performed using the substrates synthesized with the LB method at different surface pressures. Since the latter correlates with the degree of compaction and lateral density of gold particles on the surface, with increasing the surface pressure, the monolayer compaction also increased. If the surface pressure is too high, monolayer collapse and overlapping of gold nanoparticle layers occurs. This overlap and high density of nanoparticles reduces the distance between the hotspots but also could reduce the local surface Plasmon property. Also, high distance between surface particles could result in the same phenomena and reduced LSPR. Optimal LSPR is depended on several factors such as particle and hotspot distances from each other, functionalization

groups on particles and particle shape and roughness [141, 142]. In this research, at surface pressures above 13 and 10  $\text{mN m}^{-1}$ , there is a decrease in the intensity of SERS signals for 10 nm gold spherical nanoparticles and nanostars, respectively. The optimum results were observed at 13 and 10  $\text{mN m}^{-1}$  surface pressures. The next finding in this section is the optimum contact time of pollutant solutions with SERS substrate. The most intense signals of SERS correspond to the samples which are in contact with a substrate for 12h, but around 80% of saturation occurs after 30 min in both Thiram and Carbaryl.

Follow our goals in this study we tried to find the limit of detection for pollutants with the SERS technique. Aqueous solution of Thiram and Carbaryl were prepared in the range of 50 nM to 5 micromolar. Although we observe some small signals at 50 nanomolar, robust detection of Thiram and Carbaryl require concentrations higher than 100 nM. In concentration below 100 nM the heights of the pollutant peaks are in the range of the noise level.

At the end of the section, we functionalized our samples with 1-DDT to provide a better adsorption site for pollutant molecules. Our results proved that thiol-ligand on gold nanoparticles act as a Raman receptor that enhances SERS measurements.

## ***6. Final conclusions and future ideas***

In this thesis, we developed a facile protocol by means of the Langmuir-Blodgett technique for the preparation of fine-tuned SERS substrates. This method worked well as we measure SERS signals of several molecules such as the test analyte 4-MBA, or the pesticides Carbaryl and Thiram using the prepared substrates.

The most important advantage of the LB technique is the possibility of adjusting gold nanoparticle distribution by first tuning it at the water/air interface. This is difficult to control by other methods, such as self-assembly. Surface packing density of gold nanoparticles can be easily tuned by using the LB film balance and we can easily reach a desired lateral density of nanoparticles. The lateral density of the final nanostructures on the surface upon transfer to a substrate by the LB technique is correlated with the packing density of the nanoparticle film at the water/air interface.

We observed a remarkable correlation between nanoparticle size and surface morphology with their SERS performance. The size of nanoparticles and their surface roughness was also modified with electroless gold plating. By controlling the surface density of nanoparticles and also their size and roughness we modified the SERS signals. We revealed the emergence of a resonance in the SERS intensity when packing density and electroplating time was finely tuned. The prepared nanoscale structures of gold nanoparticles allow to concentrate light in tiny areas of the surface of the well-ordered surfaces, thus locally increasing the incident light intensity in what are known as hot-spots. Optimum SERS results of 4-MBA were observed when using 10 nm gold nanoparticles at a lateral pressure of  $13 \text{ mNm}^{-1}$  followed with 8 min of electroless gold plating time.

We also used different size NPs to fabricate SERS substrate. Using bigger core size NPs in the same time of electroless plating did not result in better result in comparison with 10 nm gold NPs. In the following we tested urchin shape Nps where we reached a better result and observing stronger peaks in comparison with spherical nanoparticles. Substrates were not only used to measure SERS signals of the reference molecule 4-MBA, but also in the second phase of our research we tested the substrates with Carbaryl and Thiram, as examples of water pollutants. We tried to propose a method to detect water organic contamination with high accuracy to use for on-field measurement of contaminants in water. We reach the

better results of SERS for detection of Carbaryl and Thiram when using 10 nm spherical NPs from different size at a lateral pressure of  $13 \text{ mNm}^{-1}$  following with 8 min of electroless gold plating time. Urchin shape NPs have shown the most intense peaks of SERS preparing at  $10 \text{ mNm}^{-1}$  and following with 8 min of electroless gold plating time. Finally we functionalized our substrates with 1-DDT to improve their surface adsorption capacity and to achieve better SERS results of pollutants.

SERS technique has a high potential to measure Polycyclic Aromatic Hydrocarbons (PAHs), Ammonia, Nitrates, Herbicides and Pesticides such as Carbaryl and Thiram. The intensity of Raman signals from water is negligible thus making such technique a perfect candidate for identification of molecules in water solution.

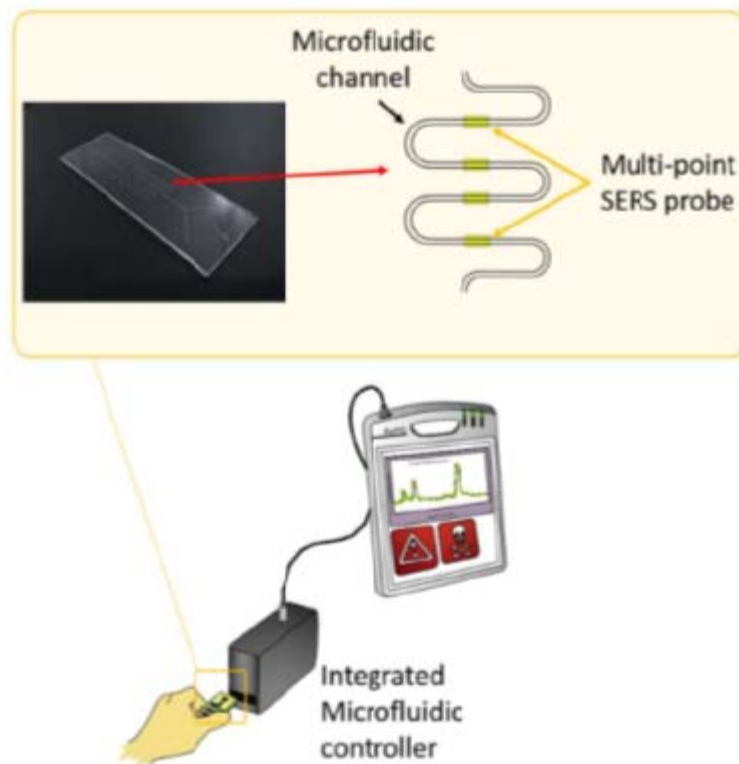
**Future goals of this research are divided in two parts:**

Control of water quality is essential and the identification of contaminants level is a key aspect to guarantee the safety of entire regions. Currently, the most reliable and commonly used detection methods for organic molecules and contaminants are based on chromatographic techniques. However, these methods are expensive, time-consuming (hours/days) and require laboratory equipment as well as highly trained operators. Nevertheless, none of the currently proposed methods meets the required performance to fulfil the specification for quick portable and cost-effective on field application.

Firstly, we need to modify our substrates to increase their sensitivity in order to reach strong signals of SERS. The presence of thiol ligands and graphene will enhance the sticking of aromatic rings and increase the efficiency of the SERS substrates for PAHs detection. The deposition of graphene on gold nanoparticles could be the next goal in order to modify the SERS substrates.

Secondly, the fabrication techniques developed here could be used to make a sensor to achieve efficient and reliable Raman measurements with portable devices. In fact, this work was part of a recent project that had that goal in mind. We propose probes/cartridges that comprise a microfluidics delivery system on the prepared nano-structured substrates, which can handle the appropriate quantity of water samples and move towards a lab-on chip integrated SERS probe. Our proposed technology is based on a label-free Surface Enhanced Raman Scattering (SERS) sensor probe realized with scalable and cost effective

nanostructures of either on the tip of an optical fiber or on a flat substrate that subsequently is integrated to obtain lab-on-chip detection.



Proposed SERS probes with patterned substrate including microfluidics and relative control integrated in a portable detection system (adapted from the RAPID project proposal that funded this research)

## List of references:

1. Bayda, S., et al., *The History of Nanoscience and Nanotechnology: From Chemical–Physical Applications to Nanomedicine*. Molecules, 2020. **25**(1).
2. Johnson, S., *Nanotechnology*, in *Encyclopedia of Applied Ethics (Second Edition)*, R. Chadwick, Editor. 2012, Academic Press: San Diego. p. 182-185.
3. Lyddy, R., *Chapter 36 - Nanotechnology*, in *Information Resources in Toxicology (Fourth Edition)*, P. Wexler, et al., Editors. 2009, Academic Press: San Diego. p. 321-328.
4. Mansoori, G.A. and T.A. Fauzi Soelaiman, *Nanotechnology &dash; An Introduction for the Standards Community*. Journal of ASTM International, 2005. **2**(6): p. 1-22.
5. Feynman, R.P.J.C.I.o.T., Engineering and S. magazine, *There's plenty of room at the bottom*. 1960.
6. Hulla, J.E., S.C. Sahu, and A.W. Hayes, *Nanotechnology: History and future*. Human & Experimental Toxicology, 2015. **34**(12): p. 1318-1321.
7. Drexler, K.E., *Nanotechnology: From Feynman to Funding*. Bulletin of Science, Technology & Society, 2004. **24**(1): p. 21-27.
8. *Nanotechnology Research Directions: IWGN Workshop Report - Vision for Nanotechnology R&D in the Next Decade*, "WTEC, Loyola College in Maryland, M. C. Roco, S. Williams, and P. Alivisatos, Eds., September 1999; "National Nanotechnology Initiative: Leading to the Next Industrial Revolution," A Report by the Interagency Working Group on Nanoscience, Engineering and Technology Committee on Technology, National Science and Technology Council, Washington, DC, February 2000, (see also [www.nano.gov](http://www.nano.gov)).
9. Baird, D. and A.J.D.t.n. Shew, *Probing the history of scanning tunneling microscopy*. 2004. **2**: p. 145-156.
10. Kattan, P., *Ratio of Surface Area to Volume in Nanotechnology and Nanoscience*. 2011.
11. Schasfoort, R.B.M., *Chapter 2 History and Physics of Surface Plasmon Resonance*, in *Handbook of Surface Plasmon Resonance (2)*. 2017, The Royal Society of Chemistry. p. 27-59.
12. Liz-Marzán, L.M., *In My Element: Gold*. 2019. **25**(3): p. 661-661.
13. Boyle, R.W., *INDICATOR ELEMENTS Indicator elements*, in *General Geology*. 1988, Springer US: Boston, MA. p. 339-372.
14. Chellan, P. and P.J. Sadler, *The elements of life and medicines*. Philosophical transactions. Series A, Mathematical, physical, and engineering sciences, 2015. **373**(2037): p. 20140182.
15. Louis, C., O.J.G.n.f.p. Pluchery, chemistry, and biology, *Gold nanoparticles in the past: before the nanotechnology era*. 2012. **1**.
16. Wagner, F.E., et al., *Before striking gold in gold-ruby glass*. Nature, 2000. **407**(6805): p. 691-692.
17. Spaer, M.J.B.J.o.t.S.o.B.R., *Gold-glass beads: a review of the evidence*. 1993. **5**(1): p. 9-25.
18. Heinzerling, P. and M. Oetken, *Nanochemistry - A Split between 18th Century and Modern Times*. World Journal of Chemical Education, 2018. **6**(1): p. 1-7.

19. Faraday, M., X. *The Bakerian Lecture. &#x2014;Experimental relations of gold (and other metals) to light.* 1857. **147**: p. 145-181.
20. Yu, S., Y. Chen, and J. Liaw. *Faraday-Tyndall effect of gold colloids.* in *2015 International Symposium on Next-Generation Electronics (ISNE)*. 2015.
21. Edwards, P.P. and J.M. Thomas, *Gold in a Metallic Divided State—From Faraday to Present-Day Nanoscience.* 2007. **46**(29): p. 5480-5486.
22. Duque, J.S., J.S. Blandón, and H. Riascos, *Localized Plasmon resonance in metal nanoparticles using Mie theory.* *Journal of Physics: Conference Series*, 2017. **850**: p. 012017.
23. Tang, Y., X. Zeng, and J. Liang, *Surface Plasmon Resonance: An Introduction to a Surface Spectroscopy Technique.* *Journal of chemical education*, 2010. **87**(7): p. 742-746.
24. Haes, A.J., et al., *Plasmonic Materials for Surface-Enhanced Sensing and Spectroscopy.* *MRS Bulletin*, 2005. **30**(5): p. 368-375.
25. Singh, S., et al., *2D Nanomaterial-Based Surface Plasmon Resonance Sensors for Biosensing Applications.* *Micromachines*, 2020. **11**(8).
26. Kheirandish, A., N. Sepehri Javan, and H. Mohammadzadeh, *Modified Drude model for small gold nanoparticles surface plasmon resonance based on the role of classical confinement.* *Scientific Reports*, 2020. **10**(1): p. 6517.
27. *Extinction*, in *Absorption and Scattering of Light by Small Particles.* 1998. p. 286-324.
28. Wriedt, T., *Mie Theory: A Review*, in *The Mie Theory: Basics and Applications*, W. Hergert and T. Wriedt, Editors. 2012, Springer Berlin Heidelberg: Berlin, Heidelberg. p. 53-71.
29. Agrawal, A., et al., *Resonant Coupling between Molecular Vibrations and Localized Surface Plasmon Resonance of Faceted Metal Oxide Nanocrystals.* *Nano Letters*, 2017. **17**(4): p. 2611-2620.
30. Sehmi, H., W. Langbein, and E.J.P.R.B. Muljarov, *Optimizing the Drude-Lorentz model for material permittivity: Method, program, and examples for gold, silver, and copper.* 2017. **95**(11): p. 115444.
31. *The Lorentz Oscillator Model and Beyond .... In: Extreme Nonlinear Optics. Advanced Texts in Physics*, in Springer, Berlin. 2005.
32. Mulvaney, P., *Surface Plasmon Spectroscopy of Nanosized Metal Particles.* *Langmuir*, 1996. **12**(3): p. 788-800.
33. Geim, A.K. and K.S. Novoselov, *The rise of graphene.* *Nat Mater*, 2007. **6**(3): p. 183-91.
34. Nicol, J.R., D. Dixon, and J.A. Coulter, *Gold nanoparticle surface functionalization: a necessary requirement in the development of novel nanotherapeutics.* 2015. **10**(8): p. 1315-1326.
35. Liu, A., et al., *Gold nanostructures with near-infrared plasmonic resonance: Synthesis and surface functionalization.* *Coordination Chemistry Reviews*, 2017. **336**: p. 28-42.
36. Serrano-Montes, A.B., et al., *A General Method for Solvent Exchange of Plasmonic Nanoparticles and Self-Assembly into SERS-Active Monolayers.* *Langmuir*, 2015. **31**(33): p. 9205-9213.
37. Ariga, K., et al., *Thin Film Nanoarchitectonics.* *Journal of Inorganic and Organometallic Polymers and Materials*, 2015. **25**(3): p. 466-479.

38. Cheng, Q., et al., *Free-Standing 2D Janus Gold Nanoparticles Monolayer Film with Tunable Bifacial Morphologies via the Asymmetric Growth at Air–Liquid Interface*. *Langmuir*, 2020. **36**(1): p. 250-256.
39. Hishimone, P., H. Nagai, and M. Sato, *Methods of Fabricating Thin Films for Energy Materials and Devices*. 2020.
40. Sondhi, P., D. Lingden, and K.J. Stine, *Structure, Formation, and Biological Interactions of Supported Lipid Bilayers (SLB) Incorporating Lipopolysaccharide*. 2020. **10**(10): p. 981.
41. Singhal, R., et al., *Poly-3-hexyl thiophene Langmuir-Blodgett films for application to glucose biosensor*. 2004. **85**(3): p. 277-282.
42. Dey, T. and D. Naughton, *Cleaning and anti-reflective (AR) hydrophobic coating of glass surface: a review from materials science perspective*. *Journal of Sol-Gel Science and Technology*, 2016. **77**(1): p. 1-27.
43. Ariga, K., *Don't Forget Langmuir–Blodgett Films 2020: Interfacial Nanoarchitectonics with Molecules, Materials, and Living Objects*. *Langmuir*, 2020. **36**(26): p. 7158-7180.
44. Tahghighi, M., et al., *Tailoring plasmonic response by Langmuir–Blodgett gold nanoparticle templating for the fabrication of SERS substrates*. *Applied Surface Science*, 2018. **447**: p. 416-422.
45. Raghuwanshi, V.S. and G. Garnier, *Cellulose Nano-Films as Bio-Interfaces*. *Frontiers in chemistry*, 2019. **7**: p. 535-535.
46. Jasper, J.J.J.o.p. and c.r. data, *The surface tension of pure liquid compounds*. 1972. **1**(4): p. 841-1010.
47. Nugent, S. and H.J.P.R.E. Posch, *Liquid drops and surface tension with smoothed particle applied mechanics*. 2000. **62**(4): p. 4968.
48. Bernardini, C., et al., *ChemInform Abstract: Colloids in Flatland: A Perspective on 2D Phase-Separated Systems, Characterization Methods, and Lineactant Design*. *Chemical Society reviews*, 2012. **42**.
49. Lheveder, C., et al., *A new Brewster angle microscope*. *Review of Scientific Instruments - REV SCI INSTR*, 1998. **69**: p. 1446-1450.
50. Sun, Z., D. Zheng, and S. Baldelli, *Distortion Correction for a Brewster Angle Microscope Using an Optical Grating*. *Analytical Chemistry*, 2017. **89**(4): p. 2186-2190.
51. Cunningham, A., P. Wood, and D. McKee, *Brewster-angle measurements of sea-surface reflectance using a high resolution spectroradiometer*. *Journal of Optics A: Pure and Applied Optics*, 2002. **4**: p. S29.
52. Vollhardt, D., *Brewster angle microscopy: A preferential method for mesoscopic characterization of monolayers at the air/water interface*. *Current Opinion in Colloid & Interface Science*, 2014. **19**(3): p. 183-197.
53. Nandi, N. and D.J.T.J.o.P.C.B. Vollhardt, *Chiral discrimination effects in Langmuir monolayers: Monolayers of palmitoyl aspartic acid, n-stearoyl serine methyl ester, and n-tetradecyl- $\gamma$ ,  $\delta$ -dihydroxypentanoic acid amide*. 2003. **107**(15): p. 3464-3475.
54. Prochazka, M., *Basics of Raman Scattering (RS) Spectroscopy*, in *Surface-Enhanced Raman Spectroscopy: Bioanalytical, Biomolecular and Medical Applications*, M. Prochazka, Editor. 2016, Springer International Publishing: Cham. p. 7-19.

55. Efremov, E.V., F. Ariese, and C. Gooijer, *Achievements in resonance Raman spectroscopy: Review of a technique with a distinct analytical chemistry potential*. *Analytica Chimica Acta*, 2008. **606**(2): p. 119-134.
56. Rostron, P., S. Gaber, and D.J.I. Gaber, *Raman spectroscopy, review*. 2016. **21**: p. 24.
57. *Vibrational Spectroscopy Techniques: Basics and Instrumentation*, in *Infrared and Raman Spectroscopy in Forensic Science*. p. 9-44.
58. Siesler, H.W., *Basic principles of near-infrared spectroscopy*, in *Handbook of near-infrared analysis*. 2007, CRC press. p. 25-38.
59. Ozaki, Y. and S.J.G.S.C. Kawata, Tokyo, Japan, *Near-infrared spectroscopy*. 1996.
60. Alessi, A., et al., *Raman and IR investigation of silica nanoparticles structure*. 2013. **362**: p. 20-24.
61. Asher, S.A.J.A.c., *UV resonance Raman spectroscopy for analytical, physical, and biophysical chemistry. Part 2*. 1993. **65**(4): p. 201A-210A.
62. Skoog, D.A., F.J. Holler, and S.R. Crouch, *Principles of Instrumental Analysis*. 2007: Thomson Brooks/Cole.
63. Rossi, E., et al., *Differential diagnosis between experimental endophthalmitis and uveitis in vitreous with Raman spectroscopy and principal components analysis*. *Journal of photochemistry and photobiology. B, Biology*, 2011. **107**: p. 73-8.
64. Jehlička, J. and H.G.M. Edwards, *Raman spectroscopy as a tool for the non-destructive identification of organic minerals in the geological record*. *Organic Geochemistry*, 2008. **39**(4): p. 371-386.
65. Carron, K.T. and L.G.J.T.J.o.P.C. Hurley, *Axial and azimuthal angle determination with surface-enhanced Raman spectroscopy: thiophenol on copper, silver, and gold metal surfaces*. 1991. **95**(24): p. 9979-9984.
66. Song, J., et al., *Gold nanoparticle coated carbon nanotube ring with enhanced raman scattering and photothermal conversion property for theranostic applications*. 2016. **138**(22): p. 7005-7015.
67. Gillibert, R., et al., *Raman tweezers for small microplastics and nanoplastics identification in seawater*. 2019. **53**(15): p. 9003-9013.
68. Jeanmaire, D.L. and R.P. Van Duyne, *Surface raman spectroelectrochemistry: Part I. Heterocyclic, aromatic, and aliphatic amines adsorbed on the anodized silver electrode*. *Journal of Electroanalytical Chemistry and Interfacial Electrochemistry*, 1977. **84**(1): p. 1-20.
69. Le Ru, E. and P. Etchegoin, *Principles of Surface-Enhanced Raman Spectroscopy: and related plasmonic effects*. 2008: Elsevier.
70. Pilot, R., et al., *A Review on Surface-Enhanced Raman Scattering*. *Biosensors*, 2019. **9**(2): p. 57.
71. Sharma, B., et al., *SERS: Materials, applications, and the future*. *Materials Today*, 2012. **15**(1): p. 16-25.
72. Maher, R., et al., *Vibrational pumping in surface enhanced Raman scattering (SERS)*. *Chemical Society reviews*, 2008. **37**: p. 965-79.
73. ADAR, F., *Introduction to Interpretation of Raman Spectra Using Database Searching and Functional Group Detection and Identification*. *Spectroscopy*, 2016. **31**(7): p. 16-23.

74. Tammer, M., *G. Sokrates: Infrared and Raman characteristic group frequencies: tables and charts*. Colloid and Polymer Science, 2004. **283**(2): p. 235-235.
75. Mohammadi, A., D.L. Nicholls, and A.J.S. Docoslis, *Improving the surface-enhanced Raman scattering performance of silver nanodendritic substrates with sprayed-on graphene-based coatings*. 2018. **18**(10): p. 3404.
76. Hu, L., et al., *Graphene oxide-decorated silver dendrites for high-performance surface-enhanced Raman scattering applications*. 2017. **5**(16): p. 3908-3915.
77. Shao, J., et al., *Nanoimprint lithography for the manufacturing of flexible electronics*. 2019. **62**(2): p. 175-198.
78. La Porta, A., M. Grzelczak, and L.M. Liz-Marzán, *Gold Nanowire Forests for SERS Detection*. ChemistryOpen, 2014. **3**(4): p. 146-151.
79. Liu, L., et al., *A high-performance and low cost SERS substrate of plasmonic nanopillars on plastic film fabricated by nanoimprint lithography with AAO template*. 2017. **7**(6): p. 065205.
80. Dill, F.H.J.I.t.o.e.d., *Optical lithography*. 1975. **22**(7): p. 440-444.
81. Mack, C., *Fundamental principles of optical lithography: the science of microfabrication*. 2008: John Wiley & Sons.
82. Srituravanich, W., et al., *Plasmonic Nanolithography*. Nano Letters, 2004. **4**(6): p. 1085-1088.
83. Garcia, R., A.W. Knoll, and E.J.N.n. Riedo, *Advanced scanning probe lithography*. 2014. **9**(8): p. 577.
84. Howell, S.T., et al., *Thermal scanning probe lithography—A review*. 2020. **6**(1): p. 1-24.
85. Mohamed, K., *Nanoimprint Lithography for Nanomanufacturing*. 2018.
86. Mohamed, K., *2.16 - Nanoimprint Lithography for Nanomanufacturing*, in *Comprehensive Nanoscience and Nanotechnology (Second Edition)*, D.L. Andrews, R.H. Lipson, and T. Nann, Editors. 2019, Academic Press: Oxford. p. 357-386.
87. Barcelo, S.J., et al., *Nanoimprint lithography of plasmonic platforms for SERS applications*. Applied Physics A, 2015. **121**(2): p. 443-449.
88. Marinescu, M., et al., *Considerations regarding the use of SU-8 photoresist in MEMS technique*. 2018.
89. Dahman, Y., *Chapter 10 - Self-Assembling Nanostructures\*\*By Yaser Dahman, Gregory Caruso, Astrid Eleosida, and Syed Tabish Hasnain*, in *Nanotechnology and Functional Materials for Engineers*, Y. Dahman, Editor. 2017, Elsevier. p. 207-228.
90. Fang, C., et al., *Preparation of a SERS substrate and its sample-loading method for point-of-use application*. Nanotechnology, 2009. **20**: p. 405604.
91. Hu, J., et al., *Novel plating solution for electroless deposition of gold film onto glass surface*. 2008. **202**(13): p. 2922-2926.
92. Wang, X., et al., *A rapid phase transfer method for nanoparticles using alkylamine stabilizers*. 2010. **348**(1): p. 24-28.
93. Mokter Hossain, M., et al., *Improvement of mechanical strength of hydrophobic coating on glass surfaces by an atmospheric pressure plasma jet*. Surface and Coatings Technology, 2019. **357**: p. 12-22.
94. Haddada, M., et al., *Optimizing the immobilization of gold nanoparticles on functionalized silicon surfaces: Amine- vs thiol-terminated silane*. Gold Bulletin, 2013. **46**: p. 335-341.

95. Stetsenko, M.O., et al., *Optical Properties of Gold Nanoparticle Assemblies on a Glass Surface*. *Nanoscale Research Letters*, 2017. **12**(1): p. 348.
96. Soliman, M.G., et al., *Phase Transfer and Polymer Coating Methods toward Improving the Stability of Metallic Nanoparticles for Biological Applications*. *Chemistry of Materials*, 2015. **27**(3): p. 990-997.
97. Fratoddi, I.J.N., *Hydrophobic and hydrophilic Au and Ag nanoparticles. Breakthroughs and perspectives*. 2018. **8**(1): p. 11.
98. Negishi, Y., et al., *Kinetic stabilization of growing gold clusters by passivation with thiolates*. 2006. **110**(25): p. 12218-12221.
99. Zhu, S., et al., *Realization of high sensitive SERS substrates with one-pot fabrication of Ag-Fe*. *Journal of Colloid and Interface Science*, 2015. **438**.
100. Liu, Y., et al., *Au@Ag Core-Shell Nanocubes: Epitaxial Growth Synthesis and Surface-Enhanced Raman Scattering Performance*. *Phys. Chem. Chem. Phys.*, 2015. **17**.
101. Whitesides, G.M. and B. Grzybowski, *Self-Assembly at All Scales*. 2002. **295**(5564): p. 2418-2421.
102. Mann, S., *Self-assembly and transformation of hybrid nano-objects and nanostructures under equilibrium and non-equilibrium conditions*. *Nature Materials*, 2009. **8**(10): p. 781-792.
103. Zhang, J., et al., *Colloidal Self-Assembly Meets Nanofabrication: From Two-Dimensional Colloidal Crystals to Nanostructure Arrays*. *Advanced Materials*, 2010. **22**(38): p. 4249-4269.
104. Vogel, N., et al., *Advances in Colloidal Assembly: The Design of Structure and Hierarchy in Two and Three Dimensions*. *Chemical Reviews*, 2015. **115**(13): p. 6265-6311.
105. Zhou, W., et al., *Lasing action in strongly coupled plasmonic nanocavity arrays*. *Nature Nanotechnology*, 2013. **8**(7): p. 506-511.
106. Ariga, K., et al., *25th Anniversary Article: What Can Be Done with the Langmuir-Blodgett Method? Recent Developments and its Critical Role in Materials Science*. *Advanced Materials*, 2013. **25**(45): p. 6477-6512.
107. Acharya, S., J.P. Hill, and K. Ariga, *Soft Langmuir-Blodgett Technique for Hard Nanomaterials*. *Advanced Materials*, 2009. **21**(29): p. 2959-2981.
108. Reculosa, S. and S. Ravaine, *Synthesis of Colloidal Crystals of Controllable Thickness through the Langmuir-Blodgett Technique*. *Chemistry of Materials*, 2003. **15**(2): p. 598-605.
109. Portal-Marco, S., et al., *Structure and physical properties of colloidal crystals made of silica particles*. *Colloids and Surfaces A: Physicochemical and Engineering Aspects*, 2012. **401**: p. 38-47.
110. Eustis, S. and M.A. El-Sayed, *Why gold nanoparticles are more precious than pretty gold: Noble metal surface plasmon resonance and its enhancement of the radiative and nonradiative properties of nanocrystals of different shapes*. *Chemical Society Reviews*, 2006. **35**(3): p. 209-217.
111. Jain, P.K., et al., *Calculated Absorption and Scattering Properties of Gold Nanoparticles of Different Size, Shape, and Composition: Applications in Biological Imaging and Biomedicine*. *The Journal of Physical Chemistry B*, 2006. **110**(14): p. 7238-7248.

112. Velev, O.D. and S. Gupta, *Materials Fabricated by Micro- and Nanoparticle Assembly – The Challenging Path from Science to Engineering*. Advanced Materials, 2009. **21**(19): p. 1897-1905.
113. Liu, J., et al., *Surface enhanced Raman scattering (SERS) fabrics for trace analysis*. Applied Surface Science, 2016. **386**: p. 296-302.
114. Tao, A., et al., *Langmuir–Blodgett Silver Nanowire Monolayers for Molecular Sensing Using Surface-Enhanced Raman Spectroscopy*. Nano Letters, 2003. **3**(9): p. 1229-1233.
115. Lu, Y., G.L. Liu, and L.P. Lee, *High-Density Silver Nanoparticle Film with Temperature-Controllable Interparticle Spacing for a Tunable Surface Enhanced Raman Scattering Substrate*. Nano Letters, 2005. **5**(1): p. 5-9.
116. Marquestaut, N., et al., *Raman Enhancement of Azobenzene Monolayers on Substrates Prepared by Langmuir–Blodgett Deposition and Electron-Beam Lithography Techniques*. Langmuir, 2008. **24**(19): p. 11313-11321.
117. Ignés-Mullol, J., J. Claret, and F. Sagués, *Star Defects, Boojums, and Cardioid Droplet Shapes in Condensed Dimyristoylphosphatidylethanolamine Monolayers*. The Journal of Physical Chemistry B, 2004. **108**(2): p. 612-619.
118. He, J., et al., *Forest of Gold Nanowires: A New Type of Nanocrystal Growth*. ACS Nano, 2013. **7**(3): p. 2733-2740.
119. Hu, J., et al., *Novel plating solution for electroless deposition of gold film onto glass surface*. Surface and Coatings Technology, 2008. **202**(13): p. 2922-2926.
120. Bantz, K.C., et al., *Recent progress in SERS biosensing*. Physical Chemistry Chemical Physics, 2011. **13**(24): p. 11551-11567.
121. Mosier-Boss, P.A., *Review of SERS Substrates for Chemical Sensing*. Nanomaterials, 2017. **7**(6).
122. McNay, G., et al., *Surface-Enhanced Raman Scattering (SERS) and Surface-Enhanced Resonance Raman Scattering (SERRS): A Review of Applications*. Applied Spectroscopy, 2011. **65**(8): p. 825-837.
123. Chang, Y.-C., B.-H. Huang, and T.-H.J.N. Lin, *Surface-enhanced Raman scattering and fluorescence on gold Nanogratings*. 2020. **10**(4): p. 776.
124. Halas, N.J., et al., *Plasmons in strongly coupled metallic nanostructures*. 2011. **111**(6): p. 3913-3961.
125. Gu, B., C. Ruan, and W. Wang, *Perchlorate Detection at Nanomolar Concentrations by Surface-Enhanced Raman Scattering*. Applied Spectroscopy, 2009. **63**(1): p. 98-102.
126. *Monolayer materials*, in *Langmuir-Blodgett Films: An Introduction*, M.C. Petty, Editor. 1996, Cambridge University Press: Cambridge. p. 65-93.
127. Zhuang, Y., et al., *Size and Shape Effect of Gold Nanoparticles in “Far-Field” Surface Plasmon Resonance*. 2019. **36**(1): p. 1800077.
128. Solís, D.M., et al., *Optimization of Nanoparticle-Based SERS Substrates through Large-Scale Realistic Simulations*. ACS Photonics, 2017. **4**(2): p. 329-337.
129. Gunnarsson, L., et al., *Interparticle Coupling Effects in Nanofabricated Substrates for Surface-Enhanced Raman Scattering*. Applied Physics Letters, 2001. **78**: p. 802-804.
130. He, L., et al., *The Distance-Dependence of Colloidal Au-Amplified Surface Plasmon Resonance*. The Journal of Physical Chemistry B, 2004. **108**(30): p. 10973-10980.

131. Ghosh, S.K. and T. Pal, *Interparticle Coupling Effect on the Surface Plasmon Resonance of Gold Nanoparticles: From Theory to Applications*. Chemical Reviews, 2007. **107**(11): p. 4797-4862.
132. Ekroth, S.B., et al., *Rapid and simple method for determination of thiram in fruits and vegetables with high-performance liquid chromatography with ultraviolet detection*. 1998. **46**(12): p. 5302-5304.
133. Sharma, V., J.S. Aulakh, and A. Malik, *Thiram: Degradation, applications and analytical methods*. Journal of environmental monitoring : JEM, 2003. **5**: p. 717-23.
134. Marvin, C. and R.J.A.C. Singh, *1. D. Brindle, CD Halt, M. Chiba*. 1990. **62**: p. 1495.
135. WATER, E.I.D., *From Carbaryl in Drinking Water, Background document for development of WHO Guidelines for Drinking-Water Quality*. 2008.
136. Shizhuang, W., et al., *Quantitative analysis of thiram based on SERS and PLSR combined with wavenumber selection*. Analytical Methods, 2014. **6**(1): p. 242-247.
137. Dao, C., et al., *High-sensitive SERS detection of thiram with silver nanodendrites substrate*. Advances in Natural Sciences: Nanoscience and Nanotechnology, 2019. **10**: p. 025012.
138. Kluncker, M., et al., *Monitoring Thiol-Ligand Exchange on Au Nanoparticle Surfaces*. Langmuir, 2018. **34**.
139. Israelsen, N., et al., *Rational design of Raman-labeled nanoparticles for a dual-modality, light scattering immunoassay on a polystyrene substrate*. Journal of Biological Engineering, 2016. **10**.
140. Sitjar, J., et al., *SERS-Active Substrate with Collective Amplification Design for Trace Analysis of Pesticides*. 2019. **9**(5): p. 664.
141. Messersmith, R.E., G.J. Nusz, and S.M.J.T.J.o.P.C.C. Reed, *Using the localized surface plasmon resonance of gold nanoparticles to monitor lipid membrane assembly and protein binding*. 2013. **117**(50): p. 26725-26733.
142. Hossain, M.K., et al., *Surface-enhanced Raman scattering: realization of localized surface plasmon resonance using unique substrates and methods*. 2009. **394**(7): p. 1747-1760.

## ***List of Publications:***

1. Tahghighi M., Mannelli I., Janner D., Ignés-Mullol J., *Tailoring plasmonic response by Langmuir–Blodgett gold nanoparticle templating for the fabrication of SERS substrates.* Applied Surface Science, 2018. **447**: p. 416-422.
2. Tahghighi M., Janner D., Ignés-Mullol J. *Optimizing Gold Nanoparticle Size and Shape for the Fabrication of SERS Substrates by Means of the Langmuir-Blodgett Technique.* Nanomaterials (Basel). 2020; **10**(11):2264.